BASAL SHEAR STRENGTH INVERSIONS FOR ICE SHEETS WITH AN APPLICATION TO JAKOBSHAVN ISBRÆ, GREENLAND

By

Marijke Habermann

RECOMMENDED:

Dr. David Maxwell

Dr. Jeff Freymueller

Dr. Erin Pettit

Dr. Carl Tape

Dr. Martin Truffer
Advisory Committee Chair

Dr. Paul McCarthy
Chair, Department of Geology and Geophysics

APPROVED:

Dr. Paul Layer
Dean, College of Natural Science and Mathematics

Dr. John Eichelberger
Dean of the Graduate School

10/28/2013
Date

BASAL SHEAR STRENGTH INVERSIONS FOR ICE SHEETS WITH AN APPLICATION TO JAKOBSHAVN ISBRÆ, GREENLAND

A

DISSERTATION

Presented to the Faculty

of the University of Alaska Fairbanks

in Partial Fulfillment of the Requirements

for the Degree of

DOCTOR OF PHILOSOPHY

By

Marijke Habermann, M.S.

Fairbanks, Alaska

December 2013

Abstract

Satellite and *in situ* observations of ice sheet outlet glaciers around the turn of the 21st century showed that rapid changes in ice dynamics are possible and important for the evolution of ice sheets. When attempting to model these dynamic changes the conditions at the ice-bed interface are crucial. Inverse methods can be used to infer basal properties, such as the basal yield stress, from abundant surface velocity observations by using a physical model of ice flow. Inverse methods are very powerful, but they need to be applied with care, otherwise errors can dominate the solution. In this study we investigate the potentials and caveats of inverse methods.

Synthetic experiments can be designed where basal conditions are assumed and an ice flow model is used to produce a set of 'synthetic' surface velocities. These can then be used to examine and evaluate inverse methods. We find that in iterative inverse methods it is essential to use a stopping criterion that will prevent overfitting the data. We introduce a new and rapidly-converging iterative inverse method called Incomplete Gauss Newton method, where the linearized problem is partly minimized in each step.

In a practical application of inverse methods to the terminus region of Jakobshavn Isbræ, Greenland we investigate changes in basal conditions over time by performing inversions for different years of available surface velocity data. We find a decrease in basal yield stress in the lower areas of the glacier that agrees with effective pressure changes due to the changes in ice geometry. This supports an ocean and terminus driven system.

The difference between the modeled and observed velocity fields, called residual, contains information about the ability to reproduce the velocities when only adjustment of the basal condition is allowed. With a properly regularized inversion the residual patterns can be used to investigate sources of error in the system. We find that the ice geometry and the model simplifications influence the ability to reproduce observed velocity fields more than the error in observed velocity does. This indicates that further progress must come from model improvements and improved capabilities to measure bedrock geometry.

Table of Contents

Page

Page

List of Figures

Page

Page

List of Tables

Page

Acknowledgements

First, I want to thank my advisor Martin Truffer. From the start he shared his knowledge, curiosity and excitement about the field. He gave me the freedom to work at my own pace, make my own mistakes and to work remotely if I needed/wanted to be somewhere else for a while. His door was always open and I am very thankful for all his feedback, comments and suggestions on my work and writing. He made sure that I could get a bit of field work with the Harding Ice Field radar survey and a few days at Ultima Thule that I will never forget. This thesis would not have been possible without David Maxwell, who developed the inverse code. His knowledge and speed always amazed me and it was a great experience to be part of the code development through different versions, different programing languages all the way to a polished and well documented open-source code. Carl Tape joined my committee in the middle of my Ph.D. and was a valuable source of information about anything related to inverse methods. Erin Pettit and Jeff Freymueller gave thought provoking feedback and support throughout my years at UAF.

Ed Bueler always finds the right words to explain the math and often helped me to develop ideas and to get started on a new topic. Andy Aschwanden and Constantine Khroulev were endlessly patient with all my questions and helped out with many problems. Ronni Grapenthin reminded me to get my own help online, but he was always willing to help out when the internet failed me. Mark Fahnestock always had explanations and ideas at hand. David Podrasky patiently answered and discussed even the silliest questions and helped with the entertainment through cubical walls. It was great to go through courses, comps and paper writing together with David P., Bob McNabb and Barbara Trüssel. Thank you, Barbara for taking me to Yakutat glacier. What a wonderful place to do field work.

With the guidance of Erin Pettit, the founder of Girls on Ice, Barbara, Joanna Young and I started an Alaska version of the program in 2011. This entire experience has taken more time away from my studies than I could have imagined, but at the same time it is one of the most rewarding things I have ever done. All of it, the fundraising, the website (oh, how much I regretted suggesting a website sometimes...), and the logistics were a tremendous learning experience. I had the pleasure of working with and learning from Cecelia Mortenson, our mountaineering guide and everybody else involved in the many hours of planning and during the program itself. I also have to thank the applicants and participants of the program for opening up and sharing so much of themselves, for being

characters and letting us feel like we are impacting their lives. Girls on Ice has clearly impacted my life! Thank you!

Will Harrison picked me up from the airport when I first arrived in Fairbanks and he is one of the reasons why the glaciers group is such an amazing community. His door was always open for silly questions about physics or glaciers or just simply a chat, and you could always count on a good story from him. I've learned many life lessons from our professors emeritus and their families, especially Keith Echelmeyer and Susan Campbell.

It has been an amazing time for me in Fairbanks. I am happy to be done and the last few months have been too busy to truly realize that I'm leaving. The time of saying goodbyes is here and I am thankful that this makes me really sad. I stayed happy during my winters in Fairbanks thanks to Moose Mountain and everyone who hiked up and skied down with me (including Scout). Thanks to my friends for all the good talks, good food and good times. And for getting me through the not so good ones. You don't even know how dull life would be without you.

Thanks to my family for all the support from far away and for understanding that I didn't make it back for Christmas most years. My housemates have become a second family to me and I am going to miss them! At this point I want to congratulate and thank Brad for making it through my Ph.D. with me. I am excited for our next adventure together!

Chapter 1
Introduction

Glaciers are fascinating features, shaping landscapes like immense conveyor belts, providing routes of easy travel, providing water resources in times of little precipitation and storing about 75% of available freshwater on Earth [*IPCC*, 2007]. This storage of freshwater largely affects current, future and past sea-levels in an ever changing climate.

Historically, glaciology textbooks have taught us that glaciers respond to climate change on time-scales that vary from decades for mountain glaciers to millennia for polar ice sheets. In other words, it is typically thought that small glaciers undergo rapid changes, while ice sheets adjust at a leisurely pace [*Truffer and Fahnestock*, 2007]. Yet, satellite observations from the beginning of the 21st century show that ice sheets and especially their outlet glaciers can change much more rapidly than commonly believed. The sudden and rapid retreat of the floating ice tongue of Jakobshavn Isbræ, Greenland, and the doubling in speed of many outlet glaciers in the southern part of Greenland are some of the most striking examples [*Howat et al.*, 2007]. These rapid changes have potentially worrying implications for the stability of ice sheets in a future climate.

The most dynamic parts of the ice sheet are the outlet glaciers where most of the ice is not frozen to the bed. Processes at the ice/bed boundary such as sliding or till deformation largely determine how much ice will be transported into the ocean. Dynamic mass losses resulting from these processes have been estimated to contribute to sea level at a rate of $0.25\,\mathrm{mm\,a^{-1}}$ between 2003 and 2008 which is comparable to the mass loss through surface melt [*Van den Broeke et al.*, 2011].

Continued improvements in many aspects of ice sheet modeling are necessary to predict future sea level in a changing climate accurately. The physics of the ice flow in an ice sheet is well understood compared to the necessary boundary and initial conditions. At the surface of the ice sheets satellite and direct observations are feasible and widely available, whereas the base and the interior of the ice can only be observed with great difficulty. The focus of this study is the basal condition of the ice, a critical boundary condition for ice sheet models, which is not well known on a large spatial scale. Ice sheet models show a great sensitivity to this parameter.

Obtaining large-scale direct observations at the base of an ice sheet is inherently difficult. Conversely, surface velocity observations are widely available from satellite and *in situ* observations. This situation where direct observations of one physical property are

abundant while another physical property is inaccessible for direct observations occurs in many geophysical settings and is commonly solved through inverse methods. With the help of inverse methods useful inferences about the world from physical observations can be obtained. The application of inverse methods requires observations (data) and a physical model (forward model), which relates the desired parameter to the observations. In a forward sense, parameters and a physical model give a prediction of what we expect to measure directly. The inverse problem is to go backwards: given a set of observations and a physical model we want to find the parameters that give the best match to the observations. Even fitting a straight line to data is a simple application of inverse methods, where the slope and the intercept of the line are the parameters that we are solving for and the linear relationship is the physical model. Fitting a straight line is a well-posed inverse problem, where a single well-defined solution is possible. In most cases where inverse methods are applied, the problem is not as simple.

Inverse methods are very powerful when applied carefully, but there are also caveats and difficulties. The problems generally relate to existence, uniqueness and stability of solutions. There may be no parameter field that fits the observations exactly, which can occur, for example, because the forward model is only an approximation. Even if such exact solutions exist, they may not be unique: There may be other solutions that fit the data exactly, these solutions might be considerably smoothed or otherwise biased. Finally, inverse problems can be extremely unstable, in the sense that small changes in measurements can lead to large changes in the estimated parameters. Such inverse problems are called ill-posed, but a key point is that they can often be stabilized by imposing additional constraints that bias the solution. This is referred to as regularization [*Aster et al.*, 2005].

With the difficulties mentioned above it is generally not possible to give an exact numerical value for the estimated parameter. Instead it might be possible to give a range of solutions or to find a weighted average of parameters. It is important to keep these limitations of inverse methods in mind and to avoid thinking of the estimated parameter as the true solution. Even if the exact parameter cannot be found, valuable information about the parameter is gained. For example, inverse methods can provide a means to assess the correctness of a forward model or to discriminate between several possible models [*Menke*, 2012].

Geophysical inverse methods were introduced to the field of glaciology by *MacAyeal* [1992] who used control methods to invert for basal stresses on ice streams from obser-

vations of surface velocities. Many early applications did not pay particular attention to the ill-posed nature of the problem and regularization methods were usually not explicitly mentioned. Examples include the application of the force balance method to finding basal velocities by *Van der Veen and Whillans* [1989], which requires large amounts of smoothing to keep solutions from showing unphysical oscillations, as pointed out by *Bahr et al.* [1994] and *Lliboutry* [1995]. Since then, the details of inverse methods have received more attention and more rigorous methods that include regularization and prevent fitting to errors in observations or in the model have been applied [e.g. *Thorsteinsson et al.*, 2003; *Truffer*, 2004; *Raymond and Gudmundsson*, 2009]. This thesis investigates the difficulties of inverse methods, develops new methods and applies them to Jakobshavn Isbræ. We discuss uncertainties in the inverse solutions explicitly and use additional information from the inversion to asses sources of errors.

Chapter 2, which is published in the *Journal of Glaciology*, demonstrates with multiple synthetic experiments the importance of stopping iterative inverse methods before the model describes noise and errors in the data instead of actual underlying relationships. We show that the slow convergence of the steepest descent method, which is currently the most commonly used iterative inverse method in glaciology, can lead to a solution that does not reach the full potential resolution. A new and rapidly converging iterative inverse method called Incomplete Gauss Newton method is introduced. As the lead author on this paper, I designed and executed the synthetic experiments, analyzed and visualized and wrote-up the results. D. Maxwell developed the Incomplete Gauss-Newton method, M. Truffer provided guidance and edited the manuscript.

Chapter 3 is accepted for publication in *The Cryosphere* and investigates changing basal conditions during the speed-up of Jakobshavn Isbræ, Greenland. In this practical application of the theoretical findings of Chapter 2 the basal conditions for different years are inferred. The sensitivity of the inversion results to parameter choices are explored and a lowering of basal yield stress close to the terminus that is significant compared to the uncertainties in the inversion is found. The results are compared to commonly used parameterizations. As the lead author, I obtained and reformatted the necessary data sets, designed the numerical experiments, analyzed, visualized and wrote-up the results. D. Maxwell wrote and documented the inverse code. M. Truffer provided guidance and edited the manuscript.

Chapter 4 will be submitted to *Journal of Glaciology* and explores the potential of resid-

ual patterns in inversions of Jakobshavn Isbræ to distinguish between different sources of error. Synthetic experiments are performed and we find that velocity observation errors are not sufficient to explain the residual patterns seen in real-data inversions. Ice geometry errors and especially errors in model simplifications are capable of reproducing similar patterns and magnitudes. Synthetic experiments with checkerboard patterns of basal yield stress show that in the upstream parts of the drainage basin the resolution strength of inferred basal yield stress is very limited. Especially in these areas of low resolution the prior estimate in an inversion determines, for the most part, the final value of basal yield stress. As the lead author, I designed and executed the experiments, analyzed, visualized and wrote-up the results. D. Maxwell assisted in the use of his inverse code, and M. Truffer provided guidance and edited the manuscript.

These three chapters are all written as manuscripts for publication and the use of variables is consistent within each manuscript but not necessarily throughout the entire thesis. In Chapter 2 the basal shear stress, τ_b, is assumed to be a linear function of velocity components (u,v);

$$\tau_{b,x} = \gamma u \quad \text{and} \quad \tau_{b,y} = \gamma v, \tag{1.1}$$

where $\gamma \geq 0$ is a scalar function of position, called the basal stickiness, which is the parameter that we are inverting for. In Chapters 3 and 4 the basal shear stress is parametrized through a power law:

$$\tau_b = \tau_c \frac{||\mathbf{u}||^{\mathrm{q}-1}}{u_{\mathrm{threshold}}^{\mathrm{q}}} \mathbf{u}, \tag{1.2}$$

where $\mathbf{u}$ is the basal velocity, and the threshold velocity $u_{\mathrm{threshold}}$ is set to 100 $\mathrm{m\,a^{-1}}$. In these two chapters, we solve for τ_c, which has units of stress and is the basal yield stress if $q = 0$. Despite setting $q = 0.25$, we call τ_c the basal yield stress. The treatment of basal till as a linearly viscous material, as done in Chapter 2, could be achieved by setting $q = 1$. In this case the basal stickiness, used in Chapter 2, and the basal yield stress, used in Chapters 3 and 4, are related through

$$\gamma = \frac{\tau_c}{u_{\mathrm{threshold}}}. \tag{1.3}$$

The linear viscous sliding law in Chapter 3 is used because this sliding law is commonly

used in glaciology and the focus of the work is the iterative inverse method and its regularization. For Jakobshavn Isbræ a sliding law approximating a plastically deforming till is more justified [*Clarke,* 2005].

References

Aster, R. C., B. Borchers, and C. H. Thurber (2005), *Parameter Estimation and Inverse Problems*, Elsevier Academic Press, New York.

Bahr, D. B., W. T. Pfeffer, and M. F. Meier (1994), Theoretical limitations to englacial velocity calculations, *J. Glaciol.*, *40*(136), 509–518.

Clarke, G. K. C. (2005), Subglacial Processes, *Annual Review of Earth and Planetary Sciences*, *33*(1), 247–276.

Howat, I. M., I. Joughin, and T. Scambos (2007), Rapid changes in ice discharge from Greenland outlet glaciers, *Science*, *315*, 1559–1561.

IPCC (2007), *Climate Change 2007: The Physical Science Basis. Contribution of Working Group I to the Fourth Assessment Report of the Intergovernmental Panel on Climate Change*, Cambridge University Press.

Lliboutry, L. A. (1995), Why calculated basal drags of ice streams can be fallacious, *J. Glaciol.*, *41*, 204–206.

MacAyeal, D. (1992), The basal stress distribution of ice stream E, Antarctica, inferred by control methods, *J. Geophys. Res.*, *97*(B1), 595–603.

Menke, W. (2012), *Geophysical Data Analysis: Discrete Inverse Theory*, 3rd ed., Academic Press, Inc., San Diego.

Raymond, M., and G. Gudmundsson (2009), Estimating basal properties of ice streams from surface measurements: a non-linear Bayesian inverse approach applied to synthetic data, *The Cryosphere*, *3*, 265–278.

Thorsteinsson, T., C. Raymond, G. Gudmundsson, R. Bindschadler, P. Vornberger, and I. Joughin (2003), Bed topography and lubrication inferred from surface measurements on fast-flowing ice streams, *J. Glaciol.*, *49*(167), 481–490.

Truffer, M. (2004), The basal speed of valley glaciers: an inverse approach, *J. Glaciol.*, *50*(169), 236–242.

Truffer, M., and M. A. Fahnestock (2007), Rethinking ice sheet time scales, *Science*, *315*, 1508–1510.

Van den Broeke, M. R., J. L. Bamber, J. Lenaerts, and E. Rignot (2011), Ice Sheets and Sea Level: Thinking Outside the Box, *Surveys in Geophysics*, *32*(4-5), 495–505.

Van der Veen, C. J., and I. M. Whillans (1989), Force budget: I. Theory and numerical methods, *J. Glaciol.*, *35*, 53–60.

Chapter 2

Reconstruction of basal properties in ice sheets using iterative inverse methods[1]

Abstract

Inverse methods are used to estimate model parameters from observations. Many inverse problems are ill-posed because they lack stability, meaning it is not possible to find solutions that are stable with respect to small changes in input data. Regularization techniques are necessary to stabilize the problem. For nonlinear inverse problems iterative inverse methods can be used as a regularization method. These methods start with an initial estimate of the model parameters, update the parameters to match observation in an iterative process that adjusts large-scale spatial features first, and use a stopping criterion to prevent the overfitting of data. This criterion determines the smoothness of the solution and thus the degree of regularization. Here, iterative inverse methods are implemented for the specific problem of reconstructing basal stickiness of an ice sheet by using the Shallow Shelf Approximation as a forward model and synthetically derived surface velocities as input data. The incomplete Gauss-Newton method is introduced and compared to the commonly used steepest descent and nonlinear conjugate gradient methods. Two different stopping criteria, the discrepancy principle and a recent-improvement threshold, are compared. The incomplete Gauss-Newton method is favored because it is rapidly-converging, and it incorporates the discrepancy principle, which leads to optimally resolved solutions.

2.1 Introduction

Obtaining large-scale direct observations at the base of an ice sheet is inherently difficult. Conversely, surface velocity observations are widely available from satellite and *in situ* measurements. This situation where direct observations of one physical property are abundant while another physical property is inaccessible for direct observations occurs in many geophysical settings and is commonly solved through inverse methods. Examples in the glaciological literature include solutions for perturbations in basal topography and basal lubrication [*Gudmundsson*, 2003; *Thorsteinsson et al.*, 2003], ice viscosity [*Rommelaere and MacAyeal*, 1997; *Arthern and Gudmundsson*, 2010], and accumulation rates and patterns [*Waddington et al.*, 2007; *Eisen*, 2008; *Steen-Larsen et al.*, 2010]. Here we will concentrate on

[1]Published as Habermann, M., D. Maxwell, and M. Truffer (2012), Reconstruction of basal properties in ice sheets using iterative inverse methods, *Journal of Glaciology*, *58*(210), 795–807.

the reconstruction of basal stickiness through surface velocity observations, but the conclusions are widely applicable, and we begin with a general introduction of inverse methods.

An inverse problem is defined by the search for physical properties that cannot be directly observed, in a system where observations and an understanding of the physical system are given. In a forward sense these three parts are related by $\mathbf{d} = \mathbf{G}(\mathbf{m})$ where $\mathbf{d}$ is a set of observations (data), $\mathbf{m}$ is a set of model parameters and $\mathbf{G}$ is the well-posed forward model describing the physics of the system [e.g. *Aster et al.*, 2005]. In order to reconstruct model parameters $\mathbf{m}$ for given data $\mathbf{d}$ the forward model $\mathbf{G}$ has to be inverted. The process of solving an inverse problem is often unstable, in that a small change in observations can lead to a large change in the reconstructed parameters. Such problems are referred to as ill-posed. A key point is that it is commonly possible to stabilize the inversion by imposing additional constraints that bias the solution, a process that is generally referred to as regularization [*Aster et al.*, 2005].

One way to approach the inverse problem is by assessing the agreement between the observations $\mathbf{d}$ and the modeled data $\mathbf{G}(\mathbf{m})$ through a misfit functional: $J(\mathbf{m}) = \|\mathbf{d} - \mathbf{G}(\mathbf{m})\|^2$ (e.g. Eq. 2.7). Then J needs to be rendered sufficiently small to find suitable model parameters $\mathbf{m}$. Here $\|\cdot\|$ denotes a chosen norm in the data space, for example the familiar L^2 norm. Observations inherently contain some amount of error, and hence the exact minimizer of J will not correspond to the true model parameters. Moreover, for an unstable inverse problem it is not desirable to find an exact minimizer of the misfit functional J because fitting the observations below the level of error in the measurements will lead to disproportionately large unrealistic features in the model parameters, a phenomenon known as overfitting. Rather, an approximate minimizer should be sought subject to stabilizing criteria, via regularization.

2.1.1 Regularization

There are a number of forms of regularization; we describe several here to place our specific method in context. One method of imposing stabilizing constraints is to introduce a cost functional that contains a regularizing term. In Tikhonov regularization this is done by defining the cost functional

$$I(\mathbf{m}, \alpha) = \alpha J(\mathbf{m}) + |||\mathbf{m}|||^2, \tag{2.1}$$

where α is a regularization parameter that determines how much weight should be given to J [e.g. *Aster et al.*, 2005, ch. 5]. The second term involves a norm $|||\cdot|||$ in parameter space and it regularizes the problem by giving preference to a particular solution with desirable properties. The L^2 norm, for example, would select a small solution. It might be more desirable to introduce other norms that measure the level of roughness in order to select for smooth solutions [e.g. *Truffer*, 2004]. Non-trivial choices are necessary when choosing a value for α. Note that minimization of I with a free regularization parameter α would lead to $\frac{\partial I}{\partial \alpha} = 0 = J$ (if that solution exists), which is not desirable. The only control on the size of J in Tikhonov regularization is through the choice of α.

A more natural approach is to incorporate the tolerance T in the cost function

$$I(\mathbf{m}, \alpha) = \alpha |J(\mathbf{m}) - T^2| + |||\mathbf{m}|||^2. \tag{2.2}$$

This can be thought of as a minimization of $|||\mathbf{m}|||$ under the condition $J = T^2$ and α is then a Lagrange multiplier familiar from many optimization problems. The tolerance in the cost function prevents overfitting and the value for α is part of the solution [*Parker*, 1994, ch. 3.02]. The value of T is chosen based on *a-priori* estimates of measurement and model error.

For linear or linearized inverse problems the latter method is the method of choice and $I(\mathbf{m}, \alpha)$ can be minimized through a direct solve [*Truffer*, 2004] or through singular value decomposition [*De Paoli and Flowers*, 2009]. For nonlinear inverse problems direct methods are impractical. Instead, the problem can be approached by iteratively minimizing J without an added smoothness term:

$$I(\mathbf{m}) = J(\mathbf{m}). \tag{2.3}$$

Calculating $J(\mathbf{m})$ requires that the forward model be solved, and this definition of the misfit functional is equivalent to the one introduced by *MacAyeal* [1993] in Eq. 7 (or *Joughin et al.* [2004], Eq. 18) where the misfit is calculated by enforcing the model physics as a constraint (with Lagrange multipliers). If the forward problem, such as the one considered here, has a diffusive character, then iterative methods for minimizing J will tend to correct large scale features first. Generally iterative inverse methods start with an initial estimate for the model parameter and subsequently correct the initial estimate in each iteration. The simplest way to regularize these iterative inverse methods is to terminate the iterations

when the misfit functional J reaches the predefined tolerance T^2, this stopping criterion is called the **discrepancy principle** and was first suggested by *Morozov* [1966]. The final result of using the discrepancy principle as a stopping criterion in iterative inverse methods is a smooth perturbation of the initial estimate that produces modeled data, $\mathbf{G}(\mathbf{m})$, consistent with the error in the observations. Small-scale features are only added if they are justified by the observations. We refer to this as a 'principled' stopping criterion. The second stopping criterion addressed here, the recent-improvement threshold, is introduced below. It is not a principled stopping criterion in the sense that it depends solely on the solution algorithm and is not informed by the amount of observational error.

A different approach to solving inverse problems treats the forward model as something that operates on probability distribution. This is known as the Bayesian approach and has been used in glaciology by, e.g., *Raymond* [2007]. Data are represented as distributions (Gaussian in the case of random and independent errors). The Bayesian approach allows the use of a-priori assumptions about the model parameter distribution. It is particularly useful if multimodal distributions are possible. In the case of Gaussian distributions, the Bayesian solution is identical to using an L^2 norm in one of the above inverse methods [*Aster et al.*, 2005, ch. 11.2].

All regularization methods lead to a solution where additional information was added to the system in order to choose a preferred solution. This a-priori information can be the choice of a-priori distributions in Bayesian methods or the choice of norms in other methods. In this work we use iterative methods where $I(\mathbf{m}) = J(\mathbf{m})$ is reduced until a stopping criterion is reached. We will show that the a-priori information in this case is the choice of initial estimate, and the choice of the iteration method, which also involves a choice of norms. Together with the stopping criterion this provides an implicit way of regularizing the problem.

2.1.2 Previous work

MacAyeal [1992] introduced iterative inverse methods to glaciology. He described the basal stickiness using basis functions whose resolution was restricted to four times the ice thickness and consequently regularized the inversion. The misfit functional was then minimized with the steepest descent method. In later work [*MacAyeal et al.*, 1995; *Vieli and Payne*, 2003; *Vieli et al.*, 2006] the tolerance was calculated but the misfit functional was completely minimized with a conjugate gradient method. Multiple sensitivity tests were

performed where the solution of an inversion was only accepted if the found minimum of the misfit functional was below the tolerance. This means that every accepted solution is a solution where a certain degree of overfitting occurred. The majority of past studies used a misfit functional without any regularization and a steepest descent method where the misfit functional was minimized until the change in its value in the past few iterations fell below a certain threshold [*Rommelaere and MacAyeal*, 1997; *Joughin et al.*, 2001, 2004; *Larour*, 2005; *Joughin et al.*, 2006; *Khazendar et al.*, 2007; *Sergienko et al.*, 2008]. We call this type of stopping criterion the **recent-improvement threshold**. More recently *Morlighem et al.* [2010] used Tikhonov regularization and the minimization was performed with a conjugate gradient method. *Maxwell et al.* [2008] introduced an accelerated Kozlov-Maz'ya iteration where two alternating well-posed forward problems with different boundary conditions are solved. They employed a stopping criterion similar to the discrepancy principle. *Arthern and Gudmundsson* [2010] viewed the problem as an 'inverse Robin problem', also solved two well-posed forward problem iteratively and used the same stopping criterion as *Maxwell et al.* [2008].

The current literature on iterative inverse methods that solve for the basal stickiness is dominated by two minimization methods: steepest descent and the nonlinear conjugate gradient method. In some studies smoothness assumptions about the solution have been incorporated. However, the majority of past studies did not apply or discuss regularization. Without a smoothness term in the cost functional or a principled stopping criterion, two undesirable outcomes are possible. In the first case, the slowness of the iterative method can lead to a premature termination and therefore the solution does not exhibit the full resolution that would be possible given the errors in the observations (underfitting). This is especially relevant for the very slowly converging steepest descent method. In the second case, the iterations are continued into a regime where overfitting occurs.

2.1.3 Outline

We use different combinations of iterative methods and stopping criteria on two synthetic data sets, a simple rectangular ice stream and a more realistic funnel-shaped ice stream. The three different minimization methods are: the steepest descent method, the nonlinear conjugate gradient method and the incomplete Gauss-Newton method. The latter uses quadratic approximations of the misfit functional, which are minimized with the discrepancy principle. To our knowledge this iterative method is new to the field of in-

verse problems, not just to glaciology. We show that it leads to significantly faster convergence than either steepest descent or the conjugate gradient method. We implement these methods with two different stopping criteria: the discrepancy principle and the recent-improvement threshold.

2.2 Methods

2.2.1 Forward model

The forward model explored in this work is the Shallow Shelf Approximation (SSA), which was introduced by *MacAyeal* [1989] and approximates large-scale flow of a weak-bedded ice stream or a floating ice shelf. It is a vertically integrated approximation of the full Stokes equations derived by small parameter arguments, and is given by

$$\begin{aligned} \frac{\partial}{\partial x}\left[2\nu H\left(2\frac{\partial u}{\partial x}+\frac{\partial v}{\partial y}\right)\right]+\frac{\partial}{\partial y}\left[\nu H\left(\frac{\partial u}{\partial y}+\frac{\partial v}{\partial x}\right)\right]-\tau_{b,x}-\rho_{\text{ice}}gH\frac{\partial z_s}{\partial x}=0 \\ \frac{\partial}{\partial y}\left[2\nu H\left(2\frac{\partial v}{\partial y}+\frac{\partial u}{\partial x}\right)\right]+\frac{\partial}{\partial x}\left[\nu H\left(\frac{\partial u}{\partial y}+\frac{\partial v}{\partial x}\right)\right]-\tau_{b,y}-\rho_{\text{ice}}gH\frac{\partial z_s}{\partial y}=0, \end{aligned} \tag{2.4}$$

where x and y are the Cartesian coordinates defining the horizontal plane, u and v are the x and y components of velocity, ρ_{ice} is the density of ice, g is the acceleration due to gravity, z_s is the surface elevation, H is the ice thickness, $\tau_{b,x}$ and $\tau_{b,y}$ are the components of the basal shear stress in the x and y directions, and ν is the effective viscosity given by

$$\nu=\frac{B}{2}D^{\frac{1}{n}-1}, \tag{2.5}$$

where

$$D^2=\varepsilon_\nu^2+\left(\frac{\partial u}{\partial x}\right)^2+\left(\frac{\partial v}{\partial y}\right)^2+\frac{1}{4}\left(\frac{\partial u}{\partial y}+\frac{\partial v}{\partial x}\right)^2+\frac{\partial u}{\partial x}\frac{\partial v}{\partial y}$$

defines an effective strain rate D. Here B is the depth-averaged flow rate factor and n is the flow law exponent, set to $n=3$. The small term ε_ν^2 is introduced to linearize the flow law for low stresses ($\varepsilon_\nu = 1\times10^{-40}\,\text{s}^{-1}$). We use the finite element method and Picard iteration (i.e. computing solutions of the SSA with a viscosity determined by the previous iteration) to find numerical solutions of the forward model.

The basal shear stress is assumed to be a linear function of velocity;

$$\tau_{b,x} = \gamma u \text{ and } \tau_{b,y} = \gamma v, \tag{2.6}$$

where $\gamma \geq 0$ is a scalar function of position, called the basal stickiness. One physical model for such a linear relationship is a linearly-viscous till layer underneath the ice. A continuous spectrum of bed models from linear viscous to perfectly plastic is implemented in our algorithm, but only the viscous bed model is presented here. We solve for $\sqrt{\gamma}$ to enforce the positivity of γ.

This model - as well as all algorithms below - were implemented with Python, and FEniCS/DOLFIN [*Logg and Wells*, 2010] was used as the finite element library.

2.2.2 The inverse problem

The inverse problem seeks to find the basal stickiness γ (the model $\mathbf{m}$) by solving equations 2.4 given the velocity components u and v (data $\mathbf{d}$). For the purposes of this paper all other model parameters are assumed to be well known.

The ill-posedness of the inverse problem derives from the viscous nature of ice flow, which implies a smoothing property: high frequency oscillations of bed stickiness are not expressed at the surface. The SSA retains this property of ice flow. For illustration, we calculate the flow through a cross-section of an ice slab of uniform thickness inclined at a constant slope and with a smoothly varying basal stickiness, solved with the 1D SSA (Fig. 2.1). This is then compared to the solution of the same problem with a high frequency component added to the basal stickiness (black curve in Fig. 2.1). The two velocity responses are indistinguishable. This damping effect increases with the frequency of the oscillations, and illustrates the ill-posedness of the inverse problem: when basal stickiness is reconstructed from surface velocities, the damping becomes magnification, and the magnification is unbounded as the frequency increases.

2.2.3 Iterative inverse methods

The modeled surface-velocity field is calculated using the SSA given a basal stickiness function ($\mathbf{u}^{\text{mod}}(\gamma)$). This model velocity field can be compared with the observed surface

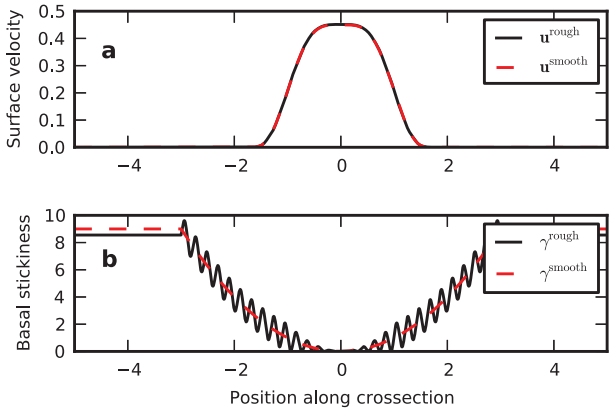

Figure 2.1. Smoothing property of viscous ice flow. Velocity solutions (a) to smooth (red) and highly variable (black) basal stickiness (b). The velocity solutions are indistinguishable. All plots have been non-dimensionalized.

velocities, $\mathbf{u}^{\text{obs}}$, and we define the misfit functional

$$J(\gamma) = \frac{1}{2}\int_{\Omega} \left|\mathbf{u}^{\text{obs}} - \mathbf{u}^{\text{mod}}(\gamma)\right|^2 d\Omega, \tag{2.7}$$

where Ω is the area of the computational domain.

Reconstructing basal stickiness is a nonlinear inverse problem where iterative inverse methods are most suitable. Any of the iterative methods applied in this study determine a sequence γ_k of candidate minimizers of J, starting with an initial estimate γ^{init}. At iteration k, a search direction $\delta\gamma_k$ is determined, and subsequently an inexact line-search is performed to find a scalar $\alpha_k > 0$ such that $J(\gamma_k + \alpha_k \delta\gamma_k)$ is approximately minimized. Having found the approximate minimizer in this direction, the candidate solution for the next iteration is updated

$$\gamma_{k+1} = \gamma_k + \alpha_k \, \delta\gamma_k \tag{2.8}$$

and the algorithm is repeated, as illustrated in Figure 2.2.

Iterative methods differ in how the search directions are selected. We use three iterative methods: steepest descent method, nonlinear conjugate gradient method and incomplete Gauss-Newton method.

For well-posed minimization problems iterations continue until γ_k is deemed sufficiently close to the true minimizer. For an ill-posed problem this is not a good strategy: the

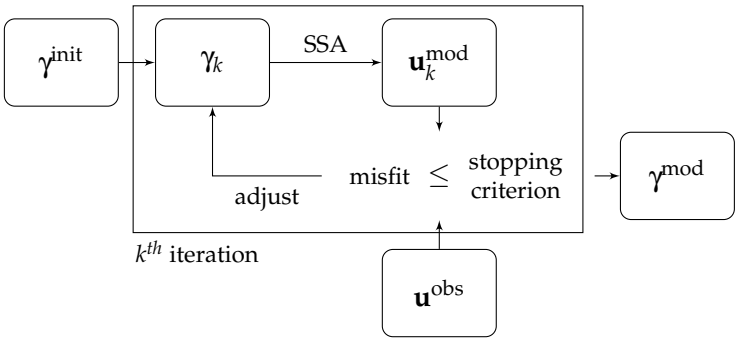

Figure 2.2. Schematic of iterative inverse method, where the forward model is the Shallow Shelf Approximation (SSA). For the iterative step ("adjust") we use three different iterative methods. The initial estimate of the basal stickiness is γ^{init}, γ_k is the basal stickiness in the k^{th} iteration, $\mathbf{u}_k^{\text{mod}}$ is the modeled surface velocity in the k^{th} iteration and $\mathbf{u}^{\text{obs}}$ are the observed data. The misfit is calculated between $\mathbf{u}_k^{\text{mod}}$ and $\mathbf{u}^{\text{obs}}$, when the stopping criterion is met γ^{mod} is the final modeled basal stickiness.

true minimizer (if it exists) will be severely contaminated by error. The iterations must be terminated early, and we discuss two methods for doing this. One of these, the discrepancy principle, is a core ingredient of the incomplete Gauss-Newton method (Eq. 2.21).

2.2.4 Stopping criteria

All three iterative methods used tend to correct large-scale features first. Intuitively this happens because large-scale features are less damped in the forward problem and therefore more readily transferred to the surface. The mathematical explanation is that all three methods use the gradient of J to generate new search directions. As shown in the Appendix this gradient is computed using an elliptic, and therefore smoothing, partial differential equation. The choice of when to stop the iteration influences the scale of features that appear in the solution. We performed experiments using the discrepancy principle, which is widely used in the inverse-problems community, as well as the recent-improvement threshold, commonly used in the glaciology community.

Discrepancy principle

The discrepancy principle stops the iterations when the desired tolerance T is reached,

$$J(\gamma) \leq \lambda^2 T^2. \tag{2.9}$$

Here $\lambda > 1$ is needed for formal proofs of convergence; we used $\lambda = 1.05$ in most experiments. The tolerance is set to the expected value of all accumulated errors. If we assume a Gaussian distribution for the random uncorrelated observation errors we arrive at an expected value of

$$T = \frac{\sqrt{2}\,\sigma^{\text{obs}}\,\Gamma\left(\frac{N+1}{2}\right)}{\Gamma\left(\frac{N}{2}\right)} \tag{2.10}$$

where σ^{obs} is the standard deviation of the distribution, N is the number of observations. For a derivation of this expression and a definition of the Γ function see *Parker* [1994], p.123. For large N the expression above can be approximated by

$$T = \sigma^{\text{obs}}\sqrt{N}. \tag{2.11}$$

The continuous version of this tolerance is $T = \sigma^{\text{obs}}\sqrt{|\Omega|}$ where $|\Omega|$ is the area of the computational domain. In any case the standard deviation σ^{obs} is a necessary algorithm input, here given in units of $\mathrm{m\,a^{-1}}$.

By stopping when the tolerance is first reached, we obtain a minimally-featured correction to the initial estimate that is consistent with surface measurements. Continuing iterations beyond this point leads to the introduction of finer scale features that are not supported by the quality of the observations, and thus leads to overfitting. In real world applications errors in observations are not the sole contributors to uncertainties. Model simplifications and the model parameter uncertainties that are part of the forward model also need to be included. This will be addressed in the discussion.

Recent-improvement threshold

Iterations are halted when the improvement in misfit functional falls below a certain threshold $\triangle$:

$$J(\gamma_{k+K}) - J(\gamma_k) \leq \triangle \tag{2.12}$$

where K is a fixed delay index.

This recent-improvement threshold stopping criterion is commonly used in the glaciology community, but values for $\triangle$ and K are generally not reported or discussed in the lit-

erature. For the present study we used $K = 10$ as used in *Joughin et al.* [2004] (Joughin, pers. comm., Dec. 2010).

How this stopping criterion relates to errors in observations or models is not known, and there is no guarantee that the last iteration will not result in a significantly larger or smaller discrepancy than the tolerance expected from the data. Therefore, we do not recommend the recent-improvement threshold as a stopping criterion and are merely assessing it here because of its past use in the literature.

2.2.5 Choice of search directions

The three methods we used for finding a search direction all make use of the gradient of J. The definition of the gradient depends on a choice of scalar product on the space of basal stickiness functions, and we used the familiar L^2 scalar product. With this choice, the gradient $\nabla J(\gamma)$ is the unique function such that for any search direction, $\delta\gamma$,

$$\left.\frac{d}{dt}\right|_{t=0} J(\gamma + t\delta\gamma) = \int_\Omega (\nabla J(\gamma)) \cdot (\delta\gamma)\, d\Omega. \tag{2.13}$$

In the case of the SSA, the computation of $\nabla J(\gamma)$ can be done by solving an adjoint partial differential equation that is similar to the SSA itself. Unlike most previous studies, we use the complete adjoint for the SSA (see Appendix).

Steepest descent

The most intuitive search direction is the direction of steepest descent, which leads to the rule

$$\delta\gamma_k = -\nabla J(\gamma_k). \tag{2.14}$$

This method turns out to be inefficient for ill-posed problems, but these inefficiencies can sometimes be tolerable with respect to the specific problem being solved and the available computing resources.

Nonlinear conjugate gradient method

The inefficiencies of steepest descent (for linear least-squares problems) were addressed by *Hestenes and Stiefel* [1952] with the conjugate gradient method (see also Shewchuck, J.R.

(1994), An introduction to the conjugate gradient method without the agonizing pain, *unpublished*). In it, the search directions are modified from the directions of steepest descent to take into account the directions previously searched (Fig. 2.3). When augmented with the discrepancy principle, the linear conjugate gradient method is a standard tool for solving linear ill-posed problems [*Hanke*, 1995].

The conjugate gradient method can be generalized to nonlinear least squares problems, although it is less well understood in this case. There is more than one generalization, and we use the Polak-Ribière rule [*Press*, 2007, p.518] for finding search directions. We first compute a scalar

$$\beta_k = \frac{\int_\Omega (\nabla J(\gamma_k) - \nabla J(\gamma_{k-1}))\, \nabla J(\gamma_k)\, d\Omega}{\int_\Omega (\nabla J(\gamma_k))^2\, d\Omega} \tag{2.15}$$

and then a search direction

$$\delta\gamma_k = -\nabla J(\gamma_k) + \beta_k\, \delta\gamma_{k-1}. \tag{2.16}$$

The amount of additional coding required for the nonlinear conjugate gradient method, compared to the method of steepest descent, is negligible.

Incomplete Gauss-Newton

The Gauss-Newton method is a standard tool for minimizing nonlinear least squares problems [*Björck*, 1996]. We describe here a modification, which we are are calling the incomplete Gauss-Newton (IGN) method that can be applied to solving ill-posed problems.

Let $\mathcal{F}$ be the map from basal stickiness γ to modeled velocities $\mathbf{u}^{\text{mod}}(\gamma)$. The misfit functional can then be written as

$$J(\gamma) = \frac{1}{2} \int_\Omega |\mathbf{u}^{\text{obs}} - \mathcal{F}(\gamma)|^2\, d\Omega. \tag{2.17}$$

Let $\mathcal{F}'_\gamma$ denote the linearization of $\mathcal{F}$ at γ, so

$$\mathcal{F}(\gamma + \delta\gamma) \approx \mathcal{F}(\gamma) + \mathcal{F}'_\gamma(\delta\gamma) \tag{2.18}$$

for small variations $\delta\gamma$. The computation of $\mathcal{F}'_\gamma$ involves solving a PDE, as described in the Appendix. In the Gauss-Newton method, at iteration k we work with the linearized

functional

$$J_{\text{lin}}(\delta\gamma) = \int_\Omega |\mathbf{u}^{\text{obs}} - \mathcal{F}(\gamma_k) - \mathcal{F}'_\gamma(\delta\gamma))|^2 \, d\Omega, \tag{2.19}$$

which is a linear least-squares problem and is an approximation of the original nonlinear least-squares problem. The minimizer $\delta\gamma_k$ of J_{lin} is then used as a search direction.

For an ill-posed problem, however, the linearized misfit functional J_{lin} is also ill-posed and cannot be minimized completely. Therefore, for the "incomplete" Gauss-Newton method we use the linear conjugate gradient algorithm, with the discrepancy principle stopping criterion, to find regularized minimizers of J_{lin}. Since J_{lin} is only an approximation of J, there is no need to minimize it all the way to the tolerance for the full problem (T in Eq. 2.11). Instead, we remove only a fraction of the remaining discrepancy. In particular, let T_k be the discrepancy of the full problem at iteration k, so

$$\int_\Omega |\mathbf{u}^{\text{obs}} - \mathcal{F}(\gamma_k)|^2 \, d\Omega = T_k^2. \tag{2.20}$$

In most cases, the discrepancy for J_{lin} is set to

$$T_{\text{lin}} = \frac{1}{2}(T_k + T), \tag{2.21}$$

so that half of the remaining discrepancy is removed when minimizing J_{lin}.[2] The approximate minimizer $\delta\gamma$ of J_{lin} found using the conjugate gradient method with the discrepancy principle is then used as the search direction:

$$\delta\gamma_k = (\text{approximate minimizer of } J_{\text{lin}}). \tag{2.22}$$

2.2.6 Illustration of steepest descent

Descriptively, the ill-posedness of a problem can be associated with the existence of small singular values, and this ultimately leads to greatly stretched contours of the misfit functional [*Trefethen and Bau*, 1997, Lecture 4]. We illustrate this by considering the projection of the misfit functional onto a two parameter space (Figure 2.3).

The tolerance, which is determined by observational errors, defines a contour along

[2] In practice the fraction of discrepancy to be removed is managed based on the success of the previous iteration. The IGN algorithm will be described in the mathematics literature (Maxwell, in prep.).

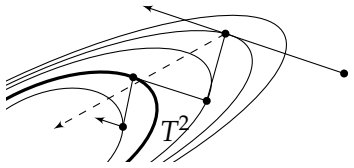

Figure 2.3. Projection of a misfit functional J onto a two dimensional parameter space. The bold contour indicates the tolerance T^2 and every parameter combination along this contour is an equally viable solution to the inverse problem. Parameter combinations inside the tolerance are overfitting the data and parameter combinations outside the tolerance are underfitting the data. Minimization paths of the steepest descent (solid line) and nonlinear conjugate gradient (dashed line) methods are displayed. Incomplete Gauss-Newton (IGN) is not easily illustrated as a 2-dimensional projection and therefore not shown here.

which all possible model parameter solutions lie. The figure also illustrates that the selected solution of the minimization depends on the initial estimate, the tolerance and the path taken. Reduced observational errors result in a smaller tolerance, and therefore less dependence on the initial estimate. The steepest descent (SD) method performs poorly in situations where the misfit functional is greatly stretched along some dimensions, due to the inefficient 'zig-zag' path. In higher dimensional parameter spaces SD performs more poorly than indicated in Figure 2.3, and might not reach the tolerance at all.

2.2.7 Synthetic ice stream examples

In synthetic data examples the quality of the reconstruction can be evaluated by comparing the 'true' basal stickiness with the modeled basal stickiness through the following procedure:

1. assume a basal stickiness distribution, γ^{true};
2. calculate the corresponding surface velocity, $\mathbf{u}^{\text{true}}$ (Eq. 2.4);
3. add Gaussian noise to simulate the random error in surface velocity observations, $\mathbf{u}^{\text{obs}}$;
4. use $\mathbf{u}^{\text{obs}}$ in the iterative inverse method to obtain γ^{mod}.

As a first simple example we define an idealized rectangular ice stream of 80 km $\times$ 160 km. We use a 60 $\times$ 120 rectangular mesh, a Gaussian bump was used for γ with the center at $x_0 = 60\,\text{km}$, $y_0 = 110\,\text{km}$, a minimum value of $5 \times 10^{-2}\,\text{kPa}\,\text{m}^{-1}\,\text{a}$, a maximum value

of $0.5\,\mathrm{kPa\,m^{-1}\,a}$ and a standard deviation of $7 \times 10^3\,\mathrm{m}$ for the x and y direction. The flow parameter was set to $B = 700\,\mathrm{a}^{1/3}\,\mathrm{kPa}$, velocity boundary conditions of zero were used on all boundaries except for the lower boundary, where a stress-free boundary was applied. The ice thickness decreases linearly from 1220 m at the upstream boundary to 900 m at the lower boundary. Figure 2.4 shows the true basal stickiness, γ_b^{true}, and the resulting true surface velocity, $\mathbf{u}^{\mathrm{true}}$.

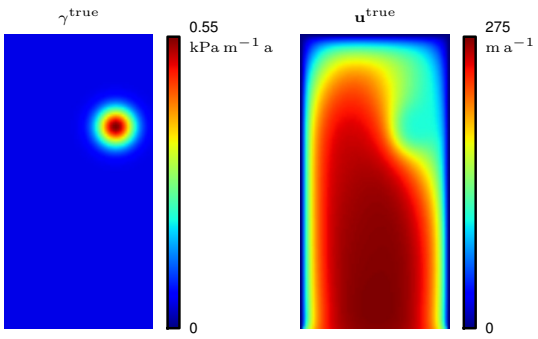

Figure 2.4. Map view of γ^{true} and $\mathbf{u}^{\mathrm{true}}$ for rectangular ice stream example. Values shown are magnitudes. Dimensions: 80 km × 160 km. Mesh: 60 × 120. Ice flows from top to bottom.

To illustrate how the choice of iterative method and stopping criterion can affect the conclusions of an experiment we recreated a synthetic ice stream example from *Joughin et al.* [2004]. They tested sensitivity to initial estimates by considering a funnel-shaped ice stream with different sets of γ^{init}. They did not add any random noise to the simulated surface velocities ($\mathbf{u}^{\mathrm{obs}} = \mathbf{u}^{\mathrm{true}}$), but they re-gridded the data sets for use in the inversion, which introduced minor sampling differences. To imitate this effect, we used the synthetic ice stream geometry and γ^{true} with 0.45 times the grid points of *Joughin et al.* [2004], then interpolated these values to the full grid and used our forward model to obtain $\mathbf{u}^{\mathrm{true}}$. The $\mathbf{u}^{\mathrm{obs}}$ were obtained from the forward model on the full grid synthetic data set. In this manner we achieved a slightly noisy set of simulated surface velocities with a mean difference between $\mathbf{u}^{\mathrm{obs}}$ and $\mathbf{u}^{\mathrm{true}}$ of $0.8\,\mathrm{m\,a^{-1}}$. The flow parameter was set to $B = 450\,\mathrm{a}^{1/3}\,\mathrm{kPa}$.

2.2.8 Evaluation of results

The synthetic data sets allow a direct comparison of the final modeled basal stickiness function with the γ^{true} used to calculate $\mathbf{u}^{\mathrm{obs}}$. To quantify the success of the inversion we

compute the mean, μ, and standard deviation, σ, of the difference $\gamma^{\text{true}} - \gamma^{\text{mod}}$. We use μ to assess biases in the inversion and σ to evaluate the overall quality of the reconstruction. Also included is the cross-correlation coefficient, ρ, between γ^{mod} and γ^{true} to evaluate how well the spatial structure is reproduced.

2.3 Results

We present results from the inversion of the rectangular ice stream and the funnel-shaped ice stream with three different iterative methods: steepest descent (SD), nonlinear conjugate gradient (NLCG) and incomplete Gauss-Newton (IGN). For SD and NLCG two different stopping criteria were used (the discrepancy principle and the recent-improvement threshold). For IGN only the discrepancy principle was used as a stopping criterion, because the discrepancy principle is necessary for finding regularized minimizers of the linearized misfit functional (Eq. 2.21). All examples with the rectangular ice stream use a constant basal stickiness as the initial estimate. All given misfit and tolerance values are normalized by the domain area and have units of ma^{-1}:

$$J^{\text{norm}} = \sqrt{\frac{J}{|\Omega|}}, \quad T^{\text{norm}} = \frac{T}{\sqrt{|\Omega|}}. \tag{2.23}$$

2.3.1 Convergence rates

Each iteration includes a line-search, and each line-search involves at least one, and sometimes several, forward-model calculations. Figure 2.5a shows the relative performance of SD, NLCG, and IGN in solving a particular inverse problem. For each iterative method, the outermost iteration is dominated by the line-search where nonlinear problems are solved, so this is a good proxy for speed. IGN is consistently faster than NLCG and SD, but the ratio of the convergence rates depends on the problem setup and the grid spacing. The reconstructed basal stickiness when using the discrepancy principle stopping criterion is virtually independent of the method of finding a search direction (Tab. 2.1). A constant initial estimate of basal stickiness and 1% error in the simulated surface velocities were used.

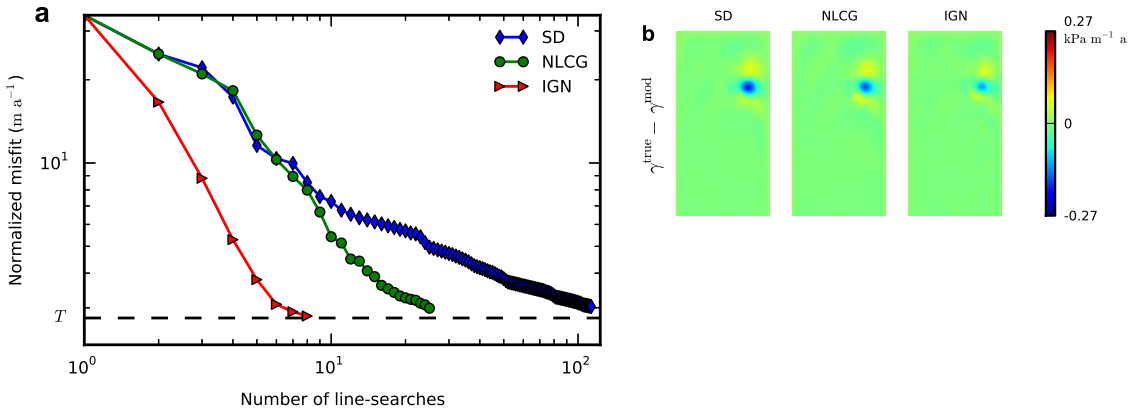

Figure 2.5. Convergence rates and results for discrepancy principle. (a) Convergence rates with the discrepancy principle and the rectangular ice stream for the three iterative methods. Each marker depicts a completed line-search and the dashed line shows the normalized tolerance T^{norm}. The algorithm stops when λT^{norm} is reached. (b) Map view of $\gamma^{\text{true}} - \gamma^{\text{mod}}$ for the three methods, see Figure 2.4 for $\mathbf{u}^{\text{true}}$ and γ^{true}. Green colors are areas where the inversion solution matches the 'true' basal stickiness well.

2.3.2 Stopping criteria

Using the discrepancy principle for all three iterative methods yields minimal differences in basal stickiness solutions, as Figure 2.5b shows. Green colors in the difference plots show areas where the inversion solution matches the 'true' basal stickiness well. Even though the figure might suggest that the IGN solution is superior to the other two solutions, inspection of the statistics in Table 2.1 shows that the IGN solution obtains a marginally better fit at the expense of a slightly worse correlation coefficient.

The recent-improvement threshold stopping criterion was directly implemented in SD and NLCG, and the results for an arbitrarily chosen threshold value of $\triangle = 1\,\text{ma}^{-1}$ are shown in Figure 2.6. The solution for SD does not reach the full possible resolution whereas NLCG coincidentally stops at the same normalized misfit value as in Figure 2.5.

The IGN algorithm is intrinsically joined to the idea of a discrepancy principle. Therefore, the recent-improvement threshold stopping criterion could not be implemented in the algorithm. But when iterations are continued past the actual tolerance T_0^{norm} (by setting $T^{\text{norm}} = 0.92\,T_0^{\text{norm}}$) a clear slow down of the convergence can be observed and the resulting basal stickiness is overfitted (Fig. 2.6). The lower correlation coefficient ($\rho = 0.89$) reflects the small-scale features that are not present in the 'true' solution (Tab. 2.2).

Table 2.1. Evaluation of results using the discrepancy principle ($T^{\text{norm}} = 2.8\,\text{m}\,\text{a}^{-1}$) with three different iterative methods. The mean, μ, and standard deviation, σ, of $\gamma^{\text{true}} - \gamma^{\text{mod}}$ are given in ($\text{kPa}\,\text{m}^{-1}\,\text{a}$). The correlation coefficient between γ^{true} and γ^{mod} is denoted by ρ. The misfit values, J^{norm}, are normalized by the domain area (Eq. 2.23) and have units of ma^{-1}.

	SD	NLCG	IGN
μ	-8.3×10^{-4}	-9.7×10^{-4}	-9.0×10^{-4}
σ	0.014	0.013	0.010
ρ	0.98	0.98	0.97
J^{norm}	2.9	2.9	2.8
No. line-searches	113	24	7

Table 2.2. Evaluation of results using the recent-improvement threshold ($\triangle = 1\,\text{m}\,\text{a}^{-1}$) for SD and NLCG (see Fig. 2.6). For comparison the IGN method was continued past the discrepancy principle tolerance ($T^{\text{norm}} = 2.8\,\text{m}\,\text{a}^{-1}$) until a visible slow down was reached. See Table 2.1 for description of variables.

	SD	NLCG	IGN
μ	-9.4×10^{-4}	-8.8×10^{-4}	-1.5×10^{-3}
σ	0.029	0.012	0.026
ρ	1.00	0.98	0.89
J^{norm}	4.7	2.9	2.7
No. line-searches	31	31	15

2.3.3 Fitting to known error

To assess the influence of error on the basal stickiness reconstruction, we performed inversions on the rectangular ice stream where the standard deviation of the added Gaussian noise is 1%, 5% and 15% of the maximum value of $\mathbf{u}^{\text{true}}$. The standard deviation of the added random error determines the value of the tolerance used (Eq. 2.11). Increased error in the simulated surface velocities leads to less capability of the model to resolve the irregularity in the velocity due to the Gaussian bump in basal stickiness (Fig. 2.7 and Table 2.3).

2.3.4 Symptoms of overfitting

To demonstrate how the data may be overfit we performed a series of experiments where the discrepancy principle was used as a stopping criterion. Instead of using the actual normalized tolerance T_0^{norm}, we only used a fraction θ of the tolerance. This leads to a tol-

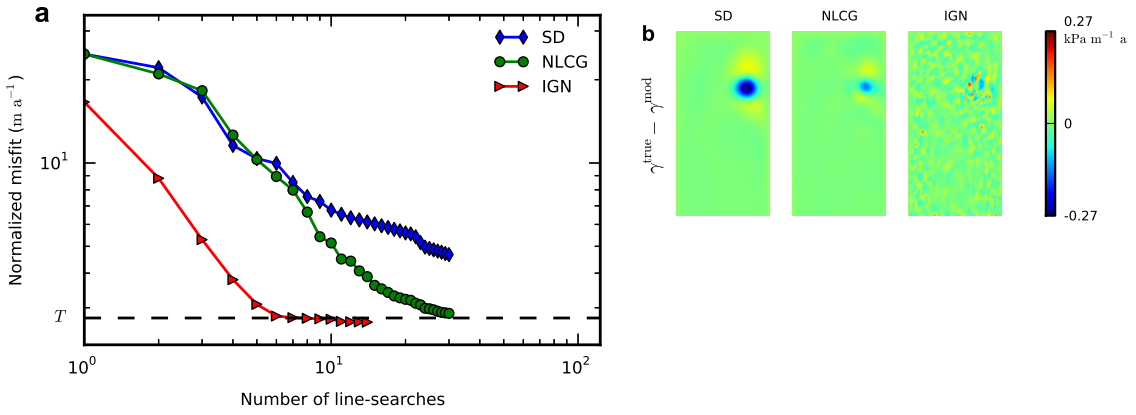

Figure 2.6. Convergence rates and results for recent-improvement threshold. (a) Convergence rate for SD and NLCG with the recent-improvement threshold ($\triangle = 1\,\mathrm{m\,a^{-1}}$). For comparison the IGN method was continued past the discrepancy principle tolerance by setting $T^{\text{norm}} = 0.92\,T_0^{\text{norm}}$. T_0^{norm} is shown as a dashed line for reference. (b) Differences between the true and the modeled basal stickiness for SD, NLCG and IGN. See Table 2.2 for an evaluation of these results. Constant initial estimate of basal stickiness and 1% error in the simulated surface velocities.

Table 2.3. Evaluation of results using 1%, 5% and 15% added error in the simulated surface velocities (see Fig. 2.7). See Table 2.1 for description of variables.

	Added error (%) , T^{norm} ($\mathrm{m\,a^{-1}}$)		
	1 , 2.8	5 , 13.8	15 , 41.3
μ	-8.6×10^{-6}	-1.5×10^{-5}	-2.3×10^{-5}
σ	1.0×10^{-4}	2.9×10^{-4}	4.2×10^{-4}
ρ	0.98	0.87	0.62
J^{norm}	2.8	14.2	42.8
No. line-searches	8	5	3

erance $T^{\text{norm}} = \theta\,T_0^{\text{norm}}$ where $0 \leq \theta \leq 1$. Therefore the iterations continue until that fraction of the error is matched in the modeled velocities; the values used are: $\theta = 0.96, 0.94, 0.93$.

In the last column of Figure 2.8 the error in the simulated surface velocities is clearly visible in the modeled velocity and the resulting basal stickiness contains very unrealistic features. See Table 2.4 for an evaluation of the results.

2.3.5 Dependence on initial estimates

We examined the sensitivity to different initial estimates by repeating synthetic inversions following *Joughin et al.* [2004]. Four different initial estimates are used: γ^{true} ('truth'), γ^{true}

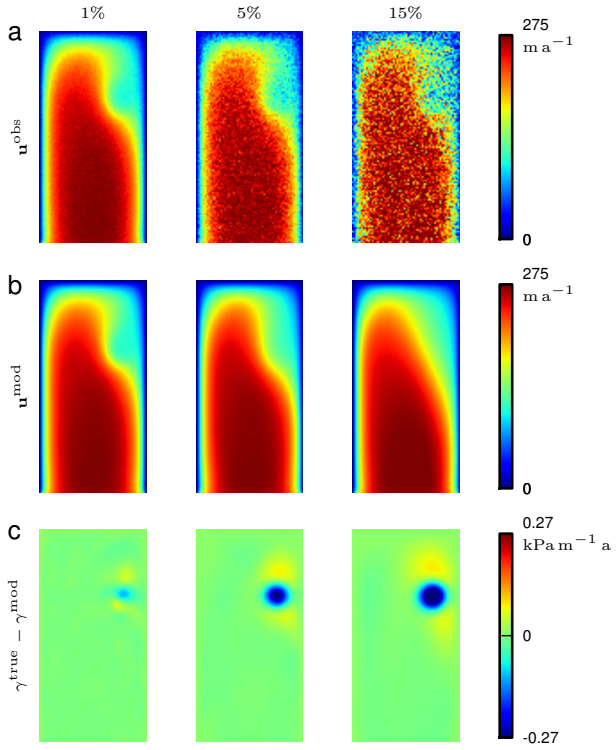

Figure 2.7. Symptoms of error in the simulated surface velocities on the resolving power of the inversion. Map view of the rectangular ice stream that flows from top to bottom. We used the IGN method and a constant initial estimate of basal stickiness. Each column shows the observed velocities (a), the modeled velocities (b) and the differences between the true and the modeled basal stickiness (c) for that particular run. The standard deviation of the added Gaussian noise is 1%, 5% and 15% of the maximum value of $\mathbf{u}^{true}$.

with added noise that has a minimum wavelength of 10 km ('noisy'), γ corresponding to 50% of the driving stress ('1/2 driving') and a constant γ ('constant') as shown in Figure 2.9a. To recreate the previous results we inverted for the basal stickiness with the SD method and a recent-improvement threshold of $10\,m\,a^{-1}$ over 10 iterations. This arbitrary value for the threshold gave results that resembled the original work by *Joughin et al.* [2004].

Figure 2.9b shows the resulting basal shear stress difference for the SD run that is comparable to Figure 3 in *Joughin et al.* [2004]. *Joughin et al.* [2004] report a value of $\rho = 0.99$ for the 'truth' example, but their figure shows discrepancies between the resulting basal shear stress and the 'true' value along the edges of the ice stream, which is also reflected in the high reported normalized misfit value of $J^{norm} = 3\,m\,a^{-1}$. Our SD 'truth' run exhibits better correspondence between the modeled and true basal shear stress: $\rho = 1$ and

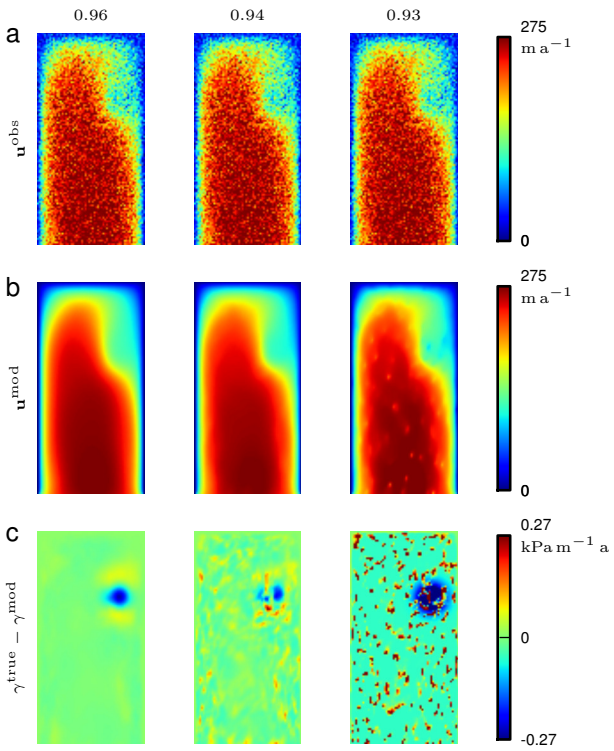

Figure 2.8. Symptoms of overfitting the data. Map view of the rectangular ice stream that flows from top to bottom. We used the IGN method and a constant initial estimate of basal stickiness. Each column shows the observed velocities (a), the modeled velocities (b) and the differences between the true and the modeled basal stickiness (c) for that particular run. Values of $\theta = 0.96, 0.94, 0.93$ were used when setting the normalized tolerance $T^{\mathrm{norm}} = \theta T_0^{\mathrm{norm}}$. All three runs have 10% error in the simulated surface velocities.

$J^{\mathrm{norm}} = 1.1\,\mathrm{m\,a^{-1}}$ (Tab. 2.5). These improved results are possibly due to the sampling differences mentioned in the methods section and to our use of the complete adjoint for the SSA equations.

We also used the IGN method with the discrepancy principle ($T^{\mathrm{norm}} = 1\,\mathrm{m\,a^{-1}}$ with $\lambda = 1.1$) as a stopping criterion on the same synthetic data set as above. This leads to the basal shear stress differences depicted in Figure 2.9c. The tolerance value $T^{\mathrm{norm}} = 1\,\mathrm{m\,a^{-1}}$ was chosen as a conservative estimate of standard deviation for the set of simulated surface velocities with a mean difference between $\mathbf{u}^{\mathrm{obs}}$ and $\mathbf{u}^{\mathrm{true}}$ of $0.8\,\mathrm{m\,a^{-1}}$ (see methods).

Table 2.4. Evaluation of results using three different amounts of overfitting (see Fig. 2.8). The actual normalized tolerance for the 10% error in the simulated surface velocities that was used in this example is: $T_0^{\text{norm}} = 27.5$. See Table 2.1 for description of variables.

	θ used in $T^{\text{norm}} = \theta T_0^{\text{norm}}$		
	0.96	0.94	0.93
μ	-8.0×10^{-6}	-2.3×10^{-5}	-3.0×10^{-4}
σ	2.3×10^{-4}	3.2×10^{-4}	3.9×10^{-3}
ρ	0.91	0.84	0.15
J^{norm}	27.5	27.3	26.8
No. line-searches	4	6	39

2.4 Discussion

2.4.1 Convergence rates and stopping criteria

The higher efficiency of IGN (Figure 2.5) makes it suitable for use with higher order forward models and in larger domains. However, this higher convergence rate also makes it more important to choose the tolerance in the discrepancy principle correctly, because we reach the regime of overfitting faster.

The iterative solution of an inverse problem is predicated on three choices: an initial estimate, an iterative method, and a stopping criterion. The experiments in Fig. 2.5 all use the same initial estimate and tolerance, and the three methods are all based on a variation of the steepest descent method. It should, therefore, not be surprising to obtain near

Table 2.5. Evaluation of results using four different initial estimates of basal shear stress and two different iterative methods: recent-improvement threshold ($\triangle = 10\,\text{m}\,\text{a}^{-1}$) for SD and discrepancy principle ($T^{\text{norm}} = 1\,\text{m}\,\text{a}^{-1}$ with $\lambda = 1.1$) for IGN (see Fig. 2.9). See Table 2.1 for description of variables. The variables μ, σ and ρ are calculated only over the fast moving parts of the ice stream (area moving faster than $300\,\text{m}\,\text{a}^{-1}$), whereas J^{norm} covers the entire domain.

	'truth'		'noisy'		'1/2 driving'		'constant'	
	SD	IGN	SD	IGN	SD	IGN	SD	IGN
μ	0.060	0.010	0.243	-0.143	-0.407	-0.062	-0.345	-0.065
σ	0.17	0.07	5.94	3.07	2.71	1.43	3.20	1.50
ρ	1.00	1.00	0.66	0.90	0.92	0.98	0.88	0.97
J^{norm}	1.1	0.8	19.4	1.1	14.5	1.0	15.0	1.1
No. line-searches	11	2	31	15	21	10	21	14

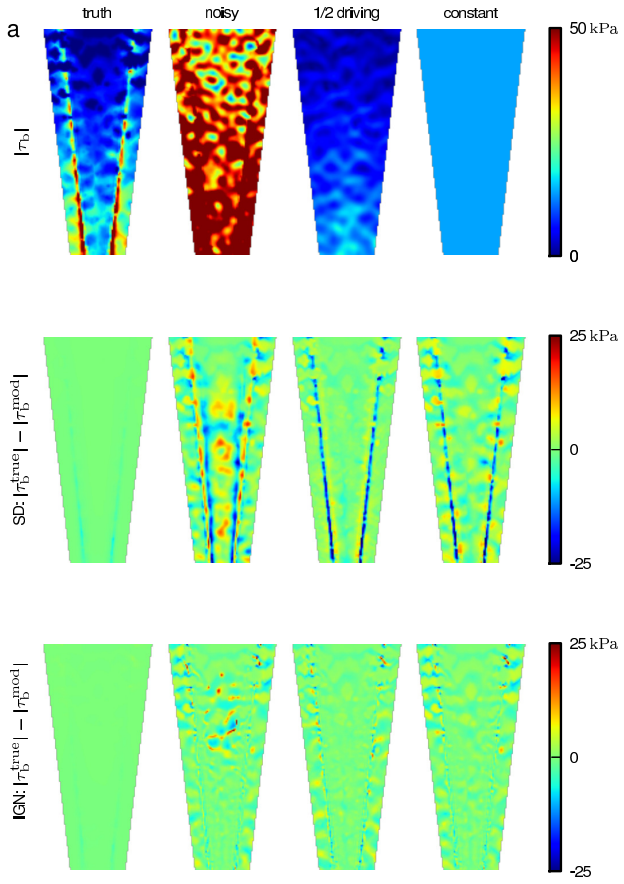

Figure 2.9. Synthetic tests with different initial estimates reproduced from *Joughin et al.* [2004]. Ice flows from top to bottom. (a) Different initial estimates of basal shear stress: 'truth', with added noise ('noisy'), 50% of the driving stress ('1/2 driving') and a constant τ_b ('constant'). (b) Difference between true and modeled basal shear stress for SD method with a recent-improvement threshold of $10\,\mathrm{m\,a^{-1}}$ in the past 10 iterations. (c) Difference between true and modeled basal shear stress for IGN method with a normalized tolerance of $T^{\mathrm{norm}} = 1\,\mathrm{m\,a^{-1}}$ with $\lambda = 1.1$.

identical solutions (Tab. 2.1). The primary difference between the methods is the rate of convergence and thus the efficiency of the algorithm.

However, with uninformed stopping criteria, such as the recent-improvement threshold, the basal stickiness solutions for the different methods can show different features for the same threshold (Fig. 2.6). The amount of observation error is not used by the algorithm, instead it is stopped when it slows down. This occurs at different times for the different methods, and consequently, the solutions can range from underfitting to overfitting (Tab. 2.2).

For larger and more complex systems the SD method will need a large number of iterations to reach the tolerance in the discrepancy principle and may not be a practical method to use. A probable reason for the popularity of the SD is that its convergence rate is slow enough that it does not reach the regime of overfitting. This can be an advantage because then the choice of stopping criterion is not crucial. On the other hand it likely lead to underfitted solutions.

2.4.2 Fitting to known error

When using the discrepancy principle as the stopping criterion the iterations stop before the model attempts to fit errors in the data. Large errors in observations lead to a large tolerance T, which results in a smaller number of line-searches (Tab. 2.3). Consequently, the algorithm only makes large-scale adjustments to the initial estimate of basal stickiness, and the resulting basal stickiness has a smooth appearance as long as the initial estimate itself was smooth (Fig. 2.7). The quality of the reconstruction decreases as the observation error increases (Tab. 2.3 and Fig. 2.7); however, this decreased quality does not manifest itself in a noisier appearance of the solution. With larger error in the observations we expect lower resolution in the solution, without any over- or underfitting.

2.4.3 Symptoms of overfitting

Fitting observation errors in the velocities means that we are trying to generate small-scale abrupt features at the surface by modifying the basal stickiness. The damping properties of the SSA lead to a magnification of these abrupt changes in the basal stickiness. This overfitting can be seen in the last column of Figure 2.8. Even though the SSA has the tendency to dampen and smooth jumps in basal stickiness, it is possible — at least in the simple rectangular ice stream used here — to fit a certain amount of observation error in the modeled surface velocities (Fig. 2.8b, last column). The positivity of the basal stickiness adds some constraint to the reconstruction but there is no other bound on the basal stickiness, so the features can get unrealistically large in order to fit the given velocities at the surface. Increased overfitting requires a sharp increase in the number of line-searches necessary to produce the unrealistically large features in basal stickiness. The smoothing properties of the SSA make it difficult to fit observation errors, especially with the added constraint of positive basal stickiness. This lead to the small range of chosen θ values for

the overffitting experiment ($\theta = 0.96, 0.94, 0.93$).

2.4.4 Dependence on initial estimates

Joughin et al. [2004] found that their inversion results depended on their initial estimates, even in synthetic examples with negligible error. We suspect that this dependence on initial estimates is due to the use of the recent-improvement threshold as a stopping criterion together with the slowly converging SD method and the resulting underfitting.

We reproduced the results shown in Figure 3 of *Joughin et al.* [2004] with the SD method and repeated the same experiment with the IGN method. *Joughin et al.* [2004] concluded from their SD run that the '1/2 driving' initial estimate gives the best basal stickiness solution and the same conclusion can be drawn from our SD results (Tab. 2.5). However, our IGN experiment Figure 2.9c shows a negligible difference between the solutions for 'constant' and '1/2 driving' initial estimates, and there is no dependence on initial estimates for these two cases when using IGN with the discrepancy principle. This shows the importance of achieving the maximum possible resolution. Only the 'noisy' initial estimate results in a slightly worse reconstruction when using IGN. The small-scale features that are present in the initial estimate are not corrected, which suggests that the initial estimate should not contain unjustified small-scale features. Using the SD method in this example, we were not able to obtain the resolution achieved by the IGN algorithm, even after allowing it to run for 1000 iterations.

Smoothness of a reconstruction should not be interpreted as a physical property of the basal stickiness, however, but rather as a lack of information about the solution; any additional features in the solution should be justified by the data. If in a certain situation it is known that the basal stickiness changes abruptly at a point in space, this additional information should be incorporated into the initial estimate. If the abrupt change is consistent with the observations at the surface, it will be preserved through the iterations to the final solution; if it is not consistent it will be corrected.

2.4.5 Modeling error

All examples in this work are synthetic examples where the error is well-known and the tolerance well defined. Real world situations are more complex because in addition to observational error, there are errors introduced by the simplifications of the physical model

(modeling errors) including the prescribed parameters therein. The accuracy of the prescribed parameters can sometimes be estimated, but other modeling errors are harder to quantify. In future work synthetic experiments comparing solutions of an inverse problem using a full-Stokes model to solutions using a simplified model, such as the SSA, could give a bound on modeling errors. Additionally, the SSA is a low order approximation of the Stokes equations and residual terms can be calculated that give an upper bound for the modeling error. In many cases modeling errors will quite possibly be larger than observational errors, especially when forward model parameters such as the ice thickness are assumed to be error free. *Gudmundsson and Raymond* [2008] note that basal stickiness is highly sensitive to un-modeled errors in basal topography, which highlights the importance of incorporating modeling errors by adjusting the stopping criterion in iterative inverse methods or by inverting for more parameters. In the case of Gaussian assumptions for model and observation errors, modeling and observational errors simply combine by addition of the respective covariance matrices, even when the forward problem is nonlinear [*Tarantola*, 2004, p. 35, example 1.36].

The abrupt change in slope of the IGN misfit curve in Figure 2.6 indicates the possible validity of the often-used 'L-curve criterion' [*Aster et al.*, 2005, p.91]. This refers to a procedure in which the tolerance is chosen at the point of the 'corner' in the misfit curve, defined by the point of maximum curvature. It defines a point at which further improvements to the misfit functional come at great cost to the norm of the solution. The sharpness of the corner will vary from problem to problem and it is not guaranteed that a clear corner will even be present. In real world examples, where the modeling error is difficult to quantify, a rapidly converging method might give a clear point of slow down that can serve as an estimate of the combined error in model and observations. While our results indicate that such an approach would be valid in our case, it needs to be stressed that the 'L-curve criterion' has no physical justification and has proven to be non-convergent in the sense that the selected regularization parameter vanishes too rapidly as the noise to signal ratio in the data goes to zero [*Hanke*, 1996].

2.5 Conclusions

Iterative inverse methods paired with a principled stopping criterion can be used to regularize and solve inverse problems. By stopping when a tolerance is reached, we obtain a minimally featured correction to an initial estimate that is consistent with observed ve-

locities. Every ill-posed inverse problem needs to be regularized and every method of regularization requires additional information in order to stably find a unique solution. The preferred approach presented here is the discrepancy principle stopping criterion together with the incomplete Gauss-Newton method, which is intrinsically tied to the discrepancy principle. The main advantage is that additional information needed to regularize the problem is very natural: all that is required is an initial estimate of the basal stickiness and a desired level of misfit, expressed as a normalized tolerance in $\mathrm{m\,a^{-1}}$.

Errors in velocity observations influence the basal stickiness solution. A stopping criterion that is informed about the amount of observation error will result in decreased resolution with increased observation error. Because the allowed misfit between observed and modeled velocity is larger with greater observation error, the algorithm will stop after correcting large-scale features. Increased noise or measurement error leads to a less detailed solution rather than a solution polluted with unphysical details.

Small-scale features in basal stickiness might and most likely do exist, but introducing small-scale features through overfitting has to be avoided. Any features in basal stickiness should be justified by surface observations, consequently any features in the initial estimate need to be based on prior information about the basal stickiness. If no prior information exists, a constant initial estimate is the recommended choice. For solutions of inverse problems smoothness should be interpreted as a lack of information in the system to determine smaller scale features.

Inevitable observation and model errors result in a risk of overfitting. Errors in observations can be largely magnified in the basal stickiness, and especially with faster converging methods such as incomplete Gauss-Newton this regime of overfitting can be reached easily. Consequently, the choice of a principled stopping criterion becomes even more important. The steepest descent method, however, has a slow convergence rate. Therefore, using steepest descent prevents overfitting, on the other hand it also inhibits us from reaching full resolution in the basal stickiness, and increases the dependence on initial estimates.

The benefits we observed using IGN may be of benefit to other nonlinear ill-posed inverse problems. An open-source implementation of the IGN algorithm is available as a part of siple: a small inverse problems library, which can be downloaded along with its tutorial from

`https://github.com/damaxwell/siple`.

These conclusions are valid for any situation where errors are present in observations or in the model (which is always the case in real world situations), even if only numerical errors are present. In all these situations there will be a possibility of over- or underfitting the data.

2.6 Acknowledgements

This work was supported by NSF CMG 0732602 and NASA MAP grant NNX09AJ38G. Ian Joughin provided data for the funnel-shaped ice stream tests. Ed Bueler, Constantine Khroulev, Andy Aschwanden and Ronni Grapenthin have patiently answered questions and provided feedback. Ralf Greve acted as Scientific Editor, and Michelle Koutnik and Olga Sergienko provided detailed comments that greatly improved the readability of the manuscript.

2.7 Appendix

The linearized SSA, its adjoint, and the gradient of J

The gradient computation needed for minimizing the misfit functional J is usually described in the glaciology literature using the framework of constrained functional minimization and Lagrange multipliers. We give an alternative derivation that allows us to also describe the PDE computations used by the incomplete Gauss-Newton method.

To write the SSA more compactly we introduce some notation. For a velocity field $\mathbf{u} = (u_1, u_2)$, the symmetric part of the derivative of $\mathbf{u}$ is $\mathbf{D}(\mathbf{u})$, so

$$D_{ij}\mathbf{u} = \frac{1}{2}\left(\frac{\partial u_i}{\partial x_j} + \frac{\partial u_j}{\partial x_i}\right). \tag{2.24}$$

Then $\operatorname{div}\mathbf{u} = \operatorname{tr}\mathbf{D}\mathbf{u} = \partial_i u_i$; the summation convention applies wherever an index is repeated. Given two square matrices $\mathbf{A} = [A_{ij}]$ and $\mathbf{B} = [B_{ij}]$ we define

$$\mathbf{A}\cdot\mathbf{B} = A_{ij}B_{ij} \tag{2.25}$$

and $|A|^2 = \mathbf{A}\cdot\mathbf{A}$. The viscosity appearing in the SSA can then be written as

$$\nu = \nu(\mathbf{u}) = \frac{B}{2}\left(\varepsilon_\nu^2 + \frac{1}{2}|\mathbf{D}\mathbf{u}|^2 + \frac{1}{2}(\operatorname{div}\mathbf{u})^2\right)^{(1-n)/2n}. \tag{2.26}$$

Assuming a linear basal stress $\tau_b = -\gamma\mathbf{u} = -\gamma(u, v)$ and a driving stress $\mathbf{f} = -\rho g H\nabla z_s$ the SSA

becomes

$$-\partial_i \left(2\nu(\mathbf{u})H\left[D_{ij}\mathbf{u} + \operatorname{div}\mathbf{u}\,\delta_{ij}\right]\right) + \gamma u_j = f_j \tag{2.27}$$

where $\delta_{ij} = 1$ if $i = j$ and is zero otherwise.

Let $\mathcal{SSA}(\mathbf{u})$ denote the left-hand side of (2.27). The linearized SSA (at $\mathbf{u}$) is given by

$$L_{\mathbf{u}}(\mathbf{w}) = \left.\frac{d}{dt}\right|_{t=0} \mathcal{SSA}(\mathbf{u} + t\mathbf{w}). \tag{2.28}$$

So if t is small,

$$\mathcal{SSA}(\mathbf{u} + t\mathbf{w}) \approx \mathcal{SSA}(\mathbf{u}) + tL_{\mathbf{u}}(\mathbf{w}) \tag{2.29}$$

A computation starting from Equation 2.28 shows that

$$\begin{aligned} L_{\mathbf{u}}(\mathbf{w}) \quad = \quad & -\partial_i \left(2\nu(\mathbf{u})H\left[D_{ij}\mathbf{w} + \operatorname{div}\mathbf{w}\,\delta_{ij}\right]\right) \\ & -\partial_i \left(2\zeta(\mathbf{u},\mathbf{w})H\left[D_{ij}\mathbf{u} + \operatorname{div}\mathbf{u}\,\delta_{ij}\right]\right) + \gamma w_j \end{aligned}$$

where

$$\begin{aligned} \zeta(\mathbf{u},\mathbf{w}) \quad = \quad & \left(\frac{1-n}{2n}\right)\frac{B}{2}\left(\varepsilon_{\nu}^2 + \frac{1}{2}|\mathbf{D}\mathbf{u}|^2 + \frac{1}{2}(\operatorname{div}\mathbf{u})^2\right)^{\frac{1-n}{2n}-1} \\ & \times\left[\mathbf{D}\mathbf{u}\cdot\mathbf{D}\mathbf{w} + \operatorname{div}\mathbf{u}\operatorname{div}\mathbf{w}\right]. \end{aligned}$$

If the SSA is being solved with periodic or Dirichlet boundary conditions, then $L_{\mathbf{u}}$ is solved with corresponding periodic or **zero** Dirichlet boundary conditions. The term involving $\zeta(\mathbf{u},\mathbf{w})$ has typically been omitted in previous studies with the SSA, but it is straightforward to include it when it is written as above and when using the finite-element method for the numerical computations. *Goldberg and Sergienko* [2011] include the term $\zeta(\mathbf{u},\mathbf{w})$ for a hybrid ice flow model and in some cases observed improved convergence rates for steepest descent inversion using the complete versus the incomplete adjoint.

Let $\mathcal{F}(\gamma)$ be the map from basal stickiness to the corresponding solution $\mathbf{u}$ of the SSA, (2.27). Implicitly differentiating (2.27) with respect to $\mathbf{u}$ and γ it follows that the derivative of $\mathcal{F}$ at γ in the direction $\delta\gamma$ (i.e. $\mathcal{F}'_{\gamma}(\delta\gamma)$) is the vector field $\mathbf{w}$ solving

$$L_{\mathbf{u}}\mathbf{w} = -\delta\gamma\mathbf{u} \tag{2.30}$$

where $\mathbf{u} = \mathcal{F}(\gamma)$. The map $\mathcal{F}'_{\gamma}$ described here is used crucially in the incomplete Gauss-

Newton method.

All of the algorithms we use employ the L^2 gradient of the misfit functional

$$J(\gamma) = \frac{1}{2}\int_\Omega \left|\mathbf{u}^{\text{obs}} - \mathcal{F}(\gamma)\right|^2 \, d\Omega. \tag{2.31}$$

Recall that the L^2 gradient $\nabla J(\gamma)$ is the unique function such that for any variation $\delta\gamma$,

$$\left.\frac{d}{dt}\right|_{t=0} J(\gamma + t\delta\gamma) = \int_\Omega (\nabla J(\gamma)) \cdot (\delta\gamma)\, d\Omega. \tag{2.32}$$

The derivative of J at γ in the direction $\delta\gamma$ is

$$\begin{aligned} J'_\gamma(\delta\gamma) \quad &= \int_\Omega \left(\mathbf{u}^{\text{obs}} - \mathcal{F}(\gamma)\right) \cdot \mathcal{F}'_\gamma(\delta\gamma)\, d\Omega \\ &= \int_\Omega \left((\mathcal{F}'_\gamma)^*(\mathbf{u}^{\text{obs}} - \mathcal{F}(\gamma))\right) \delta\gamma \, d\Omega. \end{aligned}$$

where $(\mathcal{F}'_\gamma)^*$ is the adjoint of $\mathcal{F}'_\gamma$. So

$$\nabla J(\gamma) = (\mathcal{F}'_\gamma)^*(\mathbf{u}^{\text{obs}} - \mathcal{F}(\gamma)). \tag{2.33}$$

To compute the gradient, we therefore need the adjoint of $\mathcal{F}'_\gamma$. From equation (2.30),

$$\mathcal{F}'_\gamma(\delta\gamma) = L_{\mathbf{u}}^{-1}\left(-\mathbf{u}\,\delta\gamma\right). \tag{2.34}$$

Just as for the matrix equation $(A^{-1}B)^* = B^*(A^{-1})^*$, it follows that

$$(\mathcal{F}'_\gamma)^*(\mathbf{r}) = -\mathbf{u} \cdot (L_{\mathbf{u}}^{-1})^*(\mathbf{r}) \tag{2.35}$$

for any velocity field $\mathbf{r}$. But $L_{\mathbf{u}}$ is a self-adjoint PDE, so

$$(\mathcal{F}'_\gamma)^*(\mathbf{r}) = -\mathbf{u} \cdot (L_{\mathbf{u}}^{-1})(\mathbf{r}). \tag{2.36}$$

In summary, to compute ∇J for a given γ,

1. compute $\mathbf{u} = F(\gamma)$ (i.e. solve the SSA with basal stickiness γ), and
2. find the vector field $\mathbf{z}$ solving the linear equation $L_u\mathbf{z} = \mathbf{u}^{obs} - \mathbf{u}$.

Then $\nabla J(\gamma)$ is the scalar field $-\mathbf{u}\cdot\mathbf{z}$ where $\mathbf{u}$ and $\mathbf{z}$ are computed in steps 1) and 2) above.

References

Arthern, R., and G. Gudmundsson (2010), Initialization of ice-sheet forecasts viewed as an inverse Robin problem, *J. Glaciol.*, *56*(197), 527–533.

Aster, R., B. Borchers, and C. Thurber (2005), *Parameter Estimation and Inverse Problems*, Elsevier Academic Press, New York.

Björck, A. (1996), *Numerical methods for least squares problems*, Society for Industrial and Applied Mathematics, Philadelphia, PA.

De Paoli, L., and G. Flowers (2009), Dynamics of a small surge-type glacier using one-dimensional geophysical inversion, *J. Glaciol.*, *55*(194), 1101–1112.

Eisen, O. (2008), Inference of velocity pattern from isochronous layers in firn, using an inverse method, *J. Glaciol.*, *54*(187), 613–630.

Goldberg, D., and O. Sergienko (2011), Data assimilation using a hybrid ice flow model, *Cryosphere*, *5*(2), 315–327.

Gudmundsson, G. (2003), Transmission of basal variability to a glacier surface, *J. Geophys. Res.*, *108*(B5), 2253, doi: 10.1029/2002JB002107.

Gudmundsson, G., and M. Raymond (2008), On the limit to resolution and information on basal properties obtainable from surface data on ice streams, *Cryosphere*, *2*, 167–178.

Hanke, M. (1995), *Conjugate gradient type methods for ill-posed problems*, Longman Scientific & Technical., Harlow.

Hanke, M. (1996), Limitations of the L-curve method in ill-posed problems, *BIT Num. Math.*, *36*(2), 287–301.

Hestenes, M., and E. Stiefel (1952), Methods of conjugate gradients for solving linear systems, *J. Res. Nat. Bur. Stand.*, *49*(6), 409–436.

Joughin, I., M. Fahnestock, D. MacAyeal, J. Bamber, and P. Gogineni (2001), Observation and analysis of ice flow in the largest Greenland ice stream, *J. Geophys. Res.*, *106*(D24), 34,021–34,034.

Joughin, I., D. MacAyeal, and S. Tulaczyk (2004), Basal shear stress of the Ross ice streams from control method inversions, *J. Geophys. Res.*, *109*(B9), B09,405, doi: 10.1029/2003JB002960.

Joughin, I., T. Scambos, M. Fahnestock, J. Bamber, S. Tulaczyk, and D. MacAyeal (2006), Integrating satellite observations with modelling: basal shear stress of the Filcher-Ronne ice streams, Antarctica., *Philos. Trans. R. Soc. London, Ser. A*, *364*(1844), 1795–1814.

Khazendar, A., E. Rignot, and E. Larour (2007), Larsen B Ice Shelf rheology preceding its disintegration inferred by a control method, *Geophys. Res. Lett.*, *34*(19), L19,503, doi: 10.1029/2007GL030980.

Larour, E. (2005), Rheology of the Ronne Ice Shelf, Antarctica, inferred from satellite radar interferometry data using an inverse control method, *Geophys. Res. Lett.*, *32*(5), L05,503, doi: 10.1029/2004GL021693.

Logg, A., and G. Wells (2010), DOLFIN: Automated finite element computing, *ACM T. Math. Software*, *37*(2), doi: 10.1145/1731022.1731030.

MacAyeal, D. (1989), Large-scale ice flow over a viscous basal sediment: theory and application to ice stream B, Antarctica, *J. Geophys. Res.*, *94*(B4), 4071–4087.

MacAyeal, D. (1992), The basal stress distribution of ice stream E, Antarctica, inferred by control methods, *J. Geophys. Res.*, *97*(B1), 595–603.

MacAyeal, D. (1993), A tutorial on the use of control methods in ice-sheet modeling, *J. Glaciol.*, *39*(131), 91–98.

MacAyeal, D., R. Bindschadler, and T. Scambos (1995), Basal friction of ice stream E , West Antarctica, *J. Glaciol.*, *41*(138), 247–262.

Maxwell, D., M. Truffer, S. Avdonin, and M. Stuefer (2008), An iterative scheme for determining glacier velocities and stresses, *J. Glaciol.*, *54*(188), 888–898.

Morlighem, M., E. Rignot, H. Seroussi, E. Larour, H. Ben Dhia, and D. Aubry (2010), Spatial patterns of basal drag inferred using control methods from a full-Stokes and simpler models for Pine Island Glacier, West Antarctica, *Geophys. Res. Lett.*, *37*(14), L14,502, doi: 10.1029/2010GL043853.

Morozov, V. (1966), On the solution of functional equations by the method of regularization, *Dokl. Akad. Nauk SSSR*, *7*, 414–417.

Parker, R. (1994), *Geophysical Inverse Theory*, Princeton University Press, Princeton, NJ.

Press, W. (2007), *Numerical Recipes: the art of scientific computing*, 3rd ed., Cambridge University Press, Cambridge.

Raymond, M. (2007), Estimating basal properties of glaciers and ice streams from surface measurements, Ph.D. thesis, ETH Zürich.

Rommelaere, V., and D. MacAyeal (1997), Large-scale rheology of the Ross Ice Shelf, Antarctica, computed by a control method, *Ann. Glaciol.*, *24*, 43–48.

Sergienko, O., R. Bindschadler, P. Vornberger, and D. MacAyeal (2008), Ice stream basal conditions from block-wise surface data inversion and simple regression models of ice stream flow: Application to Bindschadler Ice Stream, *J. Geophys. Res.*, *113*(F4), F04,010, doi: 10.1029/2008JF001004.

Steen-Larsen, H., E. Waddington, and M. Koutnik (2010), Formulating an inverse problem to infer the accumulation-rate pattern from deep internal layering in an ice sheet using a Monte Carlo approach, *J. Glaciol.*, *56*(196), 318–332.

Tarantola, A. (2004), *Inverse Problem Theory and Methods for Model Parameter Estimation*, Society for Industrial and Applied Mathematics, Philadelphia, PA.

Thorsteinsson, T., C. Raymond, G. Gudmundsson, R. Bindschadler, P. Vornberger, and I. Joughin (2003), Bed topography and lubrication inferred from surface measurements on fast-flowing ice streams, *J. Glaciol.*, *49*(167), 481–490.

Trefethen, L., and D. Bau (1997), *Numerical Linear Algebra [Paperback]*, 373 pp., Society for Industrial and Applied Mathematics, Philadelphia, PA.

Truffer, M. (2004), The basal speed of valley glaciers: an inverse approach, *J. Glaciol.*, *50*(169), 236–242.

Vieli, A., and A. Payne (2003), Application of control methods for modelling the flow of Pine Island Glacier, West Antarctica, *Ann. Glaciol.*, *36*(1), 197–204.

Vieli, A., A. Payne, Z. Du, and A. Shepherd (2006), Numerical modelling and data assimilation of the Larsen B ice shelf, Antarctic Peninsula., *Phil. Trans. R. Soc. London, Ser. A*, *364*(1844), 1815–1839.

Waddington, E., T. Neumann, and M. Koutnik (2007), Inference of accumulation-rate patterns from deep layers in glaciers and ice sheets, *J. Glaciol.*, *53*(183), 694–712.

Chapter 3

Changing basal conditions during the speed-up of Jakobshavn Isbræ, Greenland[1]

Abstract

Ice-sheet outlet glaciers can undergo dynamic changes such as the rapid speed-up of Jakobshavn Isbræ following the disintegration of its floating ice tongue. These changes are associated with stress changes on the boundary of the ice mass. We invert for basal conditions from surface velocity data throughout a well-observed period of rapid change and evaluate parameterizations currently used in ice-sheet models. A Tikhonov inverse method with a Shallow Shelf Approximation forward model is used for diagnostic inversions for the years 1985, 2000, 2005, 2006 and 2008. Our ice softness, model norm, and regularization parameter choices are justified using the data-model misfit metric and the L-curve method. The sensitivity of the inversion results to these parameter choices is explored. We find a lowering of basal yield stress in the first 7 km of the 2008 grounding line and no significant changes higher upstream. The temporal evolution in the fast flow area is in broad agreement with a Mohr–Coulomb parameterization of basal shear stress, but with a till friction angle much lower than has been measured for till samples. The lowering of basal yield stress is significant within the uncertainties of the inversion, but it cannot be ruled out that there are other significant contributors to the acceleration of the glacier.

3.1 Introduction

Ice sheet outlet glaciers can evolve much more dynamically than formerly thought [Truffer and Fahnestock, 2007]. Modeling and understanding the processes involved in these rapid changes is challenging. Despite the abundant surface data available from satellites, conditions within the ice and at the base of the ice are still difficult to observe, but these are crucial components of successful prognostic ice sheet models.

Jakobshavn Isbræ is one of the most active outlet glaciers in Greenland and has a century-long record of observations [Weidick et al., 1990]. This outlet glacier drains about 5.5% of the ice sheet area [Rignot and Kanagaratnam, 2006] and has undergone a rapid evolution in the last two decades. During the 1990s Jakobshavn Isbræ had a relatively stationary terminus position [Sohn et al., 1998], but starting in 1997, increased thinning of the floating ice tongue was observed [Thomas et al., 2003], followed by the retreat and

[1] Accepted for publication as Habermann, M., M. Truffer, and D. Maxwell (2013), Changing basal conditions during the speed-up of Jakobshavn Isbræ, Greenland, *The Cryosphere Discuss.*, *7*(3), 21532190.

complete disintegration of the 15 km-long ice tongue in 2003 [Podlech and Weidick, 2004]. Coinciding with the retreat of the ice front, the ice underwent a significant speed-up, almost doubling its speed by 2003 [Joughin et al., 2004]. After the disintegration of the ice tongue, the ice front retreat and the accelerations in speed have decreased but are still ongoing today [Joughin et al., 2012].

Three main processes have been identified that can contribute to the changes in outlet glaciers generally and at Jakobshavn Isbræ specifically [Joughin et al., 2012]. The first process is a speed up of the ice to compensate for a loss of downstream contact with the bed and/or fjord walls during the retreat of the ice front. The relationship between front position and speed has been well observed on longer time-scales and on seasonal time scales [Joughin et al., 2008b; Amundson et al., 2010]. The second process is a loss of overburden pressure through thinning of the ice, while the basal water pressure is assumed to be fixed by connection to the ocean. This leads to a decrease in effective pressure and a decrease in basal shear stress, which in turn leads to an increase in sliding speed [Meier and Post, 1987; Pfeffer, 2007]. The third process is a steepening of slopes induced by the strong thinning on the main trunk, causing the speed-up to diffuse inland [Joughin et al., 2008b; Payne et al., 2004]. Other possible processes include weakening of the ice in the lateral shear margins and increase in basal water pressure through changes in the hydrological system [Van der Veen et al., 2011]. The observational evidence strongly favors an acceleration mechanism that is ocean and terminus driven [Motyka et al., 2011; Joughin et al., 2012].

The well-observed changes of Jakobshavn Isbræ make it possible to investigate temporal changes in basal yield stress by inverting surface velocities for different years. Joughin et al. [2012] performed one inversion for the 1990's velocities and one for the 2009 velocities. Here we expand on this by inverting all available velocity fields and by conducting an extensive parameter study to discuss the robustness of the inversion results.

To take advantage of the wealth of surface data we use inverse methods to reconstruct conditions at the ice-bed boundary. Inverse methods were first introduced to the field of glaciology by MacAyeal [1992], and have since been used, improved and extended in multiple studies [e.g. Truffer, 2004; Maxwell et al., 2008; Raymond and Gudmundsson, 2009]. Much like other recent studies [Morlighem et al., 2010; Konovalov, 2012; Petra et al., 2012] we use a Tikhonov regularization to stabilize the solution, and we focus on justifying the choices that accompany this method.

In this study we investigate different parameter choices for the basal yield stress in-

version of Jakobshavn Isbræ, where decisions are mostly based on the data-model misfit metric. The chosen parameters are then used to invert for basal yield stress for the surface velocity data sets of the years 1985, 2000, 2005, 2006 and 2008. We discuss the robustness of these results and the agreement with commonly used parameterizations of basal yield stress.

3.2 Methods

3.2.1 Model

To investigate spatial changes and characteristics of basal shear stress we use the Shallow Shelf Approximation (SSA) [Morland, 1987] as the forward model in a Tikhonov inversion.

Forward model

The Parallel Ice Sheet Model (PISM) is a 3-D thermomechanically coupled hybrid ice sheet model that solves a combination of the Shallow Ice and Shallow Shelf Approximations [Bueler and Brown, 2009, `http://www.pism-docs.org`]. In this study only the SSA is used and the vertically averaged ice softness does not vary horizontally. Details about the SSA can be found in Schoof and Hindmarsh [2010] and the implementation in PISM is described in Bueler and Brown [2009].

We follow Joughin et al. [2012] and use the SSA as a forward model. Despite being depth-averaged the model does consider membrane stresses, vertical shear on the other hand is not considered. Ignoring vertical shear can be justified by the weak temperate basal ice layer that is present at Jakobshavn Isbræ, which concentrates vertical motion near the bottom, and by the weak bed compared to the driving stresses, which leads to motion that is dominated by basal ice motion, at least in the lower regions of the glacier [Lüthi et al., 2002]. However, it is important to keep in mind that the results derived in this paper are basal yield stress fields that are consistent with the SSA and surface observations, and might not reflect actual physical till properties.

The input fields needed for the forward SSA are: ice thickness H, surface elevation z_s, ice softness A, and a basal shear stress τ_b. The model output is the surface velocity $\mathbf{u}$. PISM treats the SSA as if it applies to the entire grid domain, even in ice-free locations. Each grid point can be either icy or ice-free, and either grounded or ocean, for a total of four states. A point is ice-free if the ice thickness H falls below a small threshold

(set to 0.01 m). The distinction between ground and ocean is made by computing what the surface elevation would be at that location for grounded ice and for floating ice; the maximum elevation determines the state. In regions where H is zero, the product of effective viscosity and thickness is regularized with a constant (set to $1 \times 10^{13}\,\mathrm{Pa\,s\,m}$), for details see `http://www.pism-docs.org`. The value of τ_b is adjusted based on the ice/ice-free grounded/ocean status of a grid point. For floating locations, the value is set to 0, and for ice-free ground it is a large constant. Consequently, τ_b depends on the effective yield stress τ_c only for grounded ice. Dirichlet boundary conditions (i.e. locations where $\mathbf{u}$ is known) are applied to the outermost 5 km of the rectangular domain (500 by 500 m grid). No additional boundary conditions are applied to the terminus of the glacier, instead the ice thickness simply decreases to zero from one grid point to the next. In this way the glacier outline is determined by the ice thickness given in the DEM for each year. We chose a grid resolution of 500 by 500 m. A finer resolution is not warranted by the data and tests with coarser grids show convergence. A finer grid might be desirable in the area of the deep trough, where basal topography changes rapidly.

The basal shear stress τ_b is parametrized through a power law:

$$\tau_b = \tau_c \frac{|\mathbf{u}|^{q-1}}{u_{\text{threshold}}^{q}} \mathbf{u}, \tag{3.1}$$

where $\mathbf{u}$ is the basal sliding velocity, and the threshold velocity $u_{\text{threshold}}$ is set to $100\ \mathrm{m\,a^{-1}}$. The purely plastic case is achieved by setting $q = 0$, whereas $q = 1$ leads to the common treatment of basal till as a linearly viscous material: $\tau_{b,x} = \gamma u$ and $\tau_{b,y} = \gamma v$, where $\gamma \geq 0$ is a scalar function of position, called the basal stickiness. When setting $q = 1$ the basal stickiness, γ, and the basal yield stress, τ_c, are related through $\gamma = \frac{\tau_c}{u_{\text{threshold}}}$. Here, instead of setting $q = 1$ and solving for γ we solve for τ_c, which has units of stress and is the basal yield stress if $q = 0$. Despite approximating the perfectly plastic case by setting $q = 0.25$ for this study, we call τ_c the *basal yield stress*. Test inversions with $q = 0.1$ and $q = 0.001$ for the 1985 and 2006 data sets result in different τ_c values, but the pattern and amplitude of changes in τ_c remain and the main conclusions of this paper are unchanged. The positivity of τ_c is enforced by solving for ζ in $\tau_c = \tau_{c,\text{scale}} \exp(\zeta)$ where $\tau_{c,\text{scale}}$ is a scale parameter to keep ζ of order 1 for typical values of τ_c.

The chosen values for q and $u_{\text{threshold}}$ used here were found to provide the best representation of observed ice motion (Bueler, personal communication, 2012). As mentioned

before, the results derived in this paper are basal yield stress fields that are consistent with our model choices and surface observations, and might not reflect actual physical till properties. The main conclusions of this paper, namely a weakening of the till near the terminus, remain valid for different choices of q and $u_{\text{threshold}}$.

We assume the instantaneous (diagnostic) surface velocities represent instantaneous deformation rates and basal yield stress at depth. In other words, no time-dependent (prognostic) runs are performed and instead the forward model calculates a velocity field from basal yield stress τ_c, and the inversion is an attempt to recover τ_c from measured surface velocities at a given time.

Inferring basal yield stress

Solving for the basal yield stress distribution is an ill-posed inverse problem, one consequence being the multitude of possible solutions. Often these ill-posed problems can be stabilized by imposing additional constraints that bias the solution. This is referred to as regularization [Aster et al., 2005]. We apply the widely used Tikhonov regularization, which defines a cost functional, $I(\tau_c, \alpha)$, with an added regularization term:

$$I(\tau_c, \alpha) = \alpha \mathbf{M}^2 + \mathbf{N}^2, \tag{3.2}$$

$$\mathbf{M}^2 = \frac{1}{\Omega} \int_\Omega ||\mathbf{u}(\tau_c) - \mathbf{u}^{\text{obs}}||^2 d\Omega \tag{3.3}$$

$$\mathbf{N}^2 = \frac{1}{\Omega} \int_\Omega c_{L^2}(\tau_c - \tau_c^{\text{prior}})^2 + K^2 c_{H^1} |\nabla(\tau_c - \tau_c^{\text{prior}})|^2 d\Omega \tag{3.4}$$

where $\mathbf{M}$ is the data-model misfit, $\mathbf{N}$ is the model norm (regularization term) and α is the regularization parameter. Note that, depending on the application, α is sometimes attached to the model norm instead of the data-model misfit. This only changes the value of α, but not any of the results. We discretize the functional $I(\tau_c, \alpha)$ by representing τ_c via a finite-element approximation, and by computing a finite element solution for $u(\tau_c)$. The gradient of this discretized functional can be computed exactly, and a minimum can be sought by any one of a number of gradient-based minimization algorithms. We use a limited-memory, variable-metric method from the Toolkit for Advanced Optimization

(TAO) [Munson et al., 2012] to seek an exact minimum of the discretized cost function, $I(\tau_c, \alpha)$. Assuming that there is a unique minimum (which is true at the very least when α is small), an exactly computed minimum of the discretized functional will be independent of the numerical method used to find it. The area Ω is defined by grounded ice (determined by hydrostatic equilibrium) and the consistent availability of velocity observations over the time periods considered. This is only part of the model domain (see Fig. 3.1), but all interpretations will be restricted by it. Below we refer to Ω as the 'misfit area'. The model norm in Eq. 3.4 is composed of two parts: the Euclidian L^2 norm and a Sobolov H^1 norm that measures the function's roughness. The factors c_{L^2} and c_{H^1} determine the relative weights of these two norms. The variable K defines a typical length scale to rescale the H^1 norm (set to 5×10^4 m). The model norm is measured as a difference from a prior estimate τ_c^{prior}. A choice of $c_{L^2} = 1$ and $c_{H^1} = 0$ results in a pure L^2 model norm, which gives preference to solutions with a small departure from the prior estimate. At the other end of the spectrum, setting $c_{L^2} = 0$ and $c_{H^1} = 1$ results in a pure H^1 model norm, which biases the solution towards smooth differences to the prior estimate.

Achieving a better data-model misfit $\mathbf{M}$ carries the cost of a larger model norm. Each choice of the regularization parameter α determines a unique value for the data-model misfit and hence the model norm. To discuss the choice of regularization parameter, α, we introduce the following vocabulary. The observation error is defined as T^{obs}, the system error is defined as $T^{\text{tot}} = T^{\text{mod}} + T^{\text{obs}}$, where the modeling error, T^{mod}, contains errors from model simplifications and errors in input parameters such as ice geometry. For an ill-posed inverse problem it is not desirable to find an exact minimizer of the data-model misfit, $\mathbf{M}$, because this would lead to overfitting of the data [Habermann et al., 2012]. The achieved data-model misfit should not be smaller than the combined error of observations, model simplifications, and parameter choices, T^{tot}. On the other hand, if the data-model misfit is too large, because we are forcing a high degree of smoothness in the basal yield stress solution, the highest possible resolution is not achieved and the data are underfit.

There are different ways to choose the regularization parameter α. The 'discrepancy principle', which sets the data-model misfit equal to T^{tot} is useful in situations where all errors in the system are known or where the observation errors can be estimated and the model errors are negligible. For the Tikhonov regularization the discrepancy principle cannot be applied directly. Instead a value for the regularization parameter α is chosen and the resulting data-model misfit value is compared to T^{tot}, if it is known.

A more common situation arises when the errors in the system are not known. It is particularly difficult to quantify model errors that originate from the use of lower order forward models, such as the SSA, and the effect of poorly constrained model parameters, such as the ice softness and bed topography, that are not part of the inversion procedure. In such cases it is possible to use a heuristic 'L-curve' method [Jay-Allemand et al., 2011; Gillet-Chaulet et al., 2012]. It has been proposed for its ease of use, despite some potential shortcomings (discussed in e.g. Vogel [1987, ch. 7]). In the L-curve method the data-model misfit is plotted against the model norm (either on a log-log or a linear scale). This curve typically has an L-shape and the regularization parameter value corresponding to the 'corner' of the curve, which is usually defined as the point of highest curvature, is chosen. The rationale behind this choice of regularization parameter is that past this corner even a small improvement in the data-model misfit can only be achieved through a large increase in the roughness of the solution.

The actual value of the data-model misfit depends on the misfit area. Therefore, the data-model misfit value can only be used to compare different inversion results if the misfit areas are identical. Here we use the same misfit area for all years, given by the consistent availability of velocity observations and by grounded ice (the 2008 grounding line limits the misfit area in the terminus region). This misfit area is shown in Figure 3.1. An appropriate data-model misfit can still lead to overfitting in some subareas and underfitting in others.

3.2.2 Data

A combination of previously published airborne and spaceborne data sets, collected between 1985 and 2008, are used as input to the model. All data sets are given on or interpolated to a 500 by 500 m grid, which is the grid size chosen for the model. Table 3.1 gives a summary of surface elevations and velocity fields used for each year.

Surface elevation

We used the 1985 and 2007 digital elevation models (DEM) derived by Motyka et al. [2010]. The 1985 DEM is based on aerial photos, whereas the 2007 DEM was derived from SPOT-5 imagery under the SPIRIT (stereoscopic survey of Polar Ice: Reference Images and Topographies) Polar Dali Program [Korona et al., 2009]. To extend the model domain we

Table 3.1. Summary of data sets used for each year. Velocity fields and surface elevation data sets used for each year, including details on acquisition dates and source references. The 2007 SPOT DEM that is mentioned was obtained July 24, 2007. The outline of the glacier is given by the ice thickness of the DEM for each inverted year. The misfit area is the same for all years (see Fig. 3.1).

Year	Period covered by vel. field	Reference for vel.	Date of surface DEM	Reference for DEM
1985	7 – 24 July, 1985	courtesy of M. Fahnestock	24 July, 1985 (aerial photo)	Motyka et al. [2010]
2000	3 Sep, 2000 – 24 Jan, 2001 (RADARSAT-1 satellite)	Joughin et al. [2010]	2007 SPOT DEM - dh/dt for 2000 courtesy of B. Smith	Motyka et al. [2010] & Joughin et al. [2012]
2005	13 Dec, 2005 – 20 Apr, 2006 (RADARSAT-1 satellite)	Joughin et al. [2010]	2007 SPOT DEM - dh/dt for 2005 courtesy of B. Smith	Motyka et al. [2010] & Joughin et al. [2012]
2006	Winter average 2006 – 2007, no further detail given	Joughin et al. [2010]	2007 SPOT DEM - dh/dt for 2006 courtesy of B. Smith	Motyka et al. [2010] & Joughin et al. [2012]
2008	Winter average 2008 – 2009, no further detail given	Joughin et al. [2010]	2007 SPOT DEM - dh/dt for 2008 courtesy of B. Smith	Motyka et al. [2010] & Joughin et al. [2012]

took lower resolution surface elevations given by Bamber et al. [2001], and substituted the high resolution DEMs in the coverage area. As a result there are sharp transitions from the high resolution DEM to the low resolution DEM. These sharp transitions result in unphysical driving stresses and we smooth the DEM by performing a short (2 week) non-sliding Shallow Ice Approximation run on a regional scale with PISM. The model domain was chosen beyond the extent of the high resolution DEMs to minimize the impact of boundary effects on the results. Model results are only evaluated within the coverage area of the high resolution DEMs (Fig. 3.1).

For the years 2000-2008 we used the 2007 DEM together with annual elevation-difference maps from Joughin et al. [2012].

Bed elevation

The bed DEM was developed at the University of Kansas using data collected by their airborne depth-sounding radar [Plummer et al., 2008]. It is important to point out that the bed elevation is one of the model input fields with significant uncertainties. Even though the Jakobshavn Isbræ drainage area has been flown repeatedly with a radar depth sounder, the deep trough with its steep margins often does not allow for clear bed returns.

We investigate the influence of bed topography on the inversion results in Habermann [in print] and we find that errors in bed topography lead to residuals that are larger than the residuals due to errors in velocity observations. This large expected error is consistent over all inversions performed here and we do not expect a significant influence on the changes in basal yield stress.

Ice flow velocity

NASA's Making Earth System Data Records for Use in Research Environments (MEaSUREs) program, provides annual ice-sheet-wide velocity maps for Greenland, derived using Interferometric Synthetic Aperture Radar (InSAR) data from the RADARSAT-1 satellite. The data set contains ice velocity data for the winter of 2000-2001 and 2005-2006, 2006-2007, and 2007-2008 acquired from RADARSAT-1 InSAR data from the Alaska Satellite Facility (ASF), and a 2008-2009 mosaic derived from the Advanced Land Observation Satellite (ALOS) and TerraSAR-X data [Joughin et al., 2010]. Here we are using all available velocity data sets except for 2007-2008, which contains data gaps.

For the 1985 inversion we use a velocity data set derived from feature tracking of orthophotos used in the formation of the 1985 DEM [Motyka et al., 2011].

Model domain

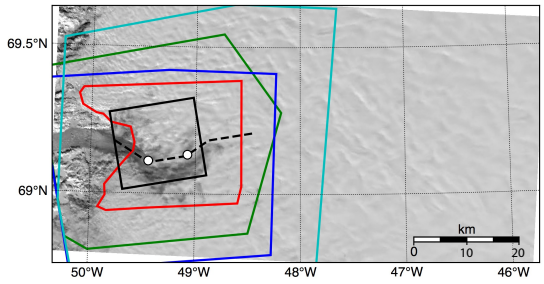

Figure 3.1. Overview of model domain and data extents. Model domain (entire area shown) with MODIS image for reference (single pass MODIS image, spring 2001, courtesy of M. Fahnestock). Also shown are the extent of the higher resolution bed topography (cyan), 2007 DEM (green), 1985 DEM (blue), misfit area (red), straightened centerline (dashed black), and the area later shown in all the map-view figures (solid black). The white circles mark the two 'bends' mentioned in the text.

The forward model has to be evaluated repeatedly in the inversion, but all runs are instantaneous. This eliminates the need for a careful treatment of the boundary areas or the solution of the SSA in the entire drainage area, as done in regional time-dependent models. Instead we choose a limited model domain for efficiency, but include enough area around the used data sets (DEMs and bed elevation) to minimize boundary effects. We evaluate results spatially and along a centerline, which was extracted by approximately following the minimum bed elevation (Fig. 3.1). Figure 3.1 shows the model domain and the areas of high resolution DEMs and bed elevation as well as the misfit area used to calculate the data-model misfit in the inversion. The SSA is solved over the entire model domain, but only velocity data within the misfit area is used to adjust the basal yield stress. Results are only interpreted within the misfit area, which is taken to be the same for all years. Areas outside the misfit area are shaded or excluded in all figures.

3.3 Choices in forward model and inversion

The model outlined above contains several poorly constrained parameter choices. In this section we discuss the choice for ice softness A in the forward model, the choice of model norm in the regularization term, the prior estimate for the basal yield stress, and the magnitude of the regularization parameter. For the model norm and the prior estimate of basal yield stress we used the 2006 data set, for all other parameters all inverted years where considered to determine the value. Final parameter choices were made after several iterations. We arrived at the following default values:

- Ice softness: $A = 2.5 \times 10^{-24}$ Pa^{-3}s^{-1}
- Model norm: $c_{L2} = 0$, $c_{H1} = 1$
- Prior estimate: $\tau_c^{prior} = 1.4 \times 10^5$ Pa
- Regularization parameter: $\alpha = 10$

Below we will discuss each choice by studying the effects of varying one parameter at the time, while holding the others at their default value.

3.3.1 Ice softness

The forward model contains many parameter choices, here we only discuss the ice softness parameter. All other values for the forward model are discussed in Section 3.2.1. Default values, or values that have proven to be good choices in other studies are used whenever possible. The SSA uses a viscosity that is dependent on a vertically averaged ice softness parameter A which in turn depends on the temperature of the ice. Temperature has only been measured in a few boreholes [Lüthi et al., 2002] and its spatial distribution is not known. Here the vertically averaged ice softness does not vary horizontally for the entire model domain and we test different ice softness values. A spatially-variable ice softness would lead to basal yield stress fields that are consistent with the ice softness and therefore different than the basal yield stress fields found here. Nonetheless, we would expect all main findings about the changes and sensitivities of basal yield stress to stay true. Additionally, we conducted time-dependent numerical experiments (spin-ups), where not only the ice flow but also temperature fields were computed. These experiments show little horizontal variability in the vertically averaged ice softness.

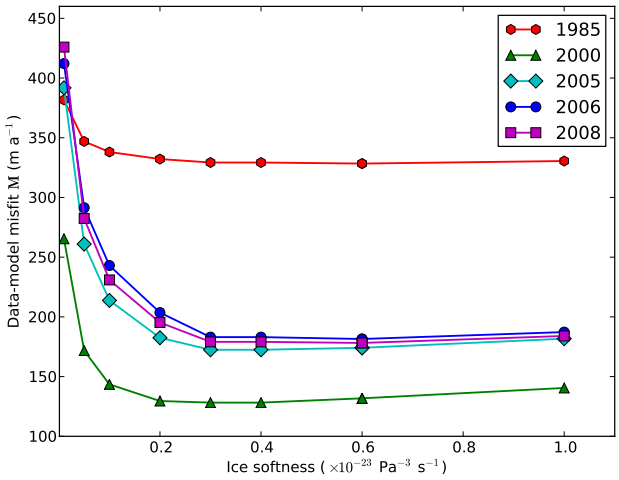

Figure 3.2. Data-model misfit for different ice softness values. Hard ice (small value of ice softness A) leads to a marked increase in data-model misfit, whereas softer ice only slightly increases the data-model misfit. We choose the ice softness $A = 2.5 \times 10^{-24}$ Pa^{-3}s^{-1} for all years and the range from 2 - 3×10^{-24} Pa^{-3}s^{-1} is discussed.

Suggested values of ice softness in Cuffey and Paterson [2010, chapter 3.4.6, p.72ff] range from 0.01×10^{-24} Pa^{-3}s^{-1} for ice at -40°C to 2.4×10^{-24} Pa^{-3}s^{-1} for temperate ice, while values as high as 9.3×10^{-24} Pa^{-3}s^{-1} have been reported from laboratory tests [Budd and Jacka, 1989]. Higher values of ice softness are often used and justified by the anisotropy of ice or effects of grain size and/or impurities [Lüthi et al., 2002].

The achieved data-model misfit for different ice softnesses (Fig. 3.2) shows that only very hard ice (low A) leads to a marked increase in the data-model misfit. This confirms the finding of Joughin et al. [2012] that a hard ice model is not a good representation of the ice rheology of Jakobshavn Isbræ. On the other hand, Joughin et al. [2012] find with a terminus-driven model that a soft ice model ($A = 10 \times 10^{-24}$ Pa^{-3}s^{-1}) does not transfer seasonal changes far enough inland. Here the ice softness value 2.5×10^{-24} Pa^{-3}s^{-1} is chosen for all years as a compromise between 2 and 3×10^{-24} Pa^{-3}s^{-1}, which give the lowest data-model misfit for 1985, 2000 and 2005, 2006, 2008, respectively. This ice softness is equivalent to an isothermal ice column with a temperature of ~ 3°C using the flow law temperature dependence given by Cuffey and Paterson [2010]. For comparison, at a site on the ice sheet adjacent to the ice stream Lüthi et al. [2002] measured borehole temperatures that provide an estimate of ice softness equivalent to ~15°C isothermal ice, indicating our

chosen ice softness has some enhancement relative to the borehole.

3.3.2 Model norm

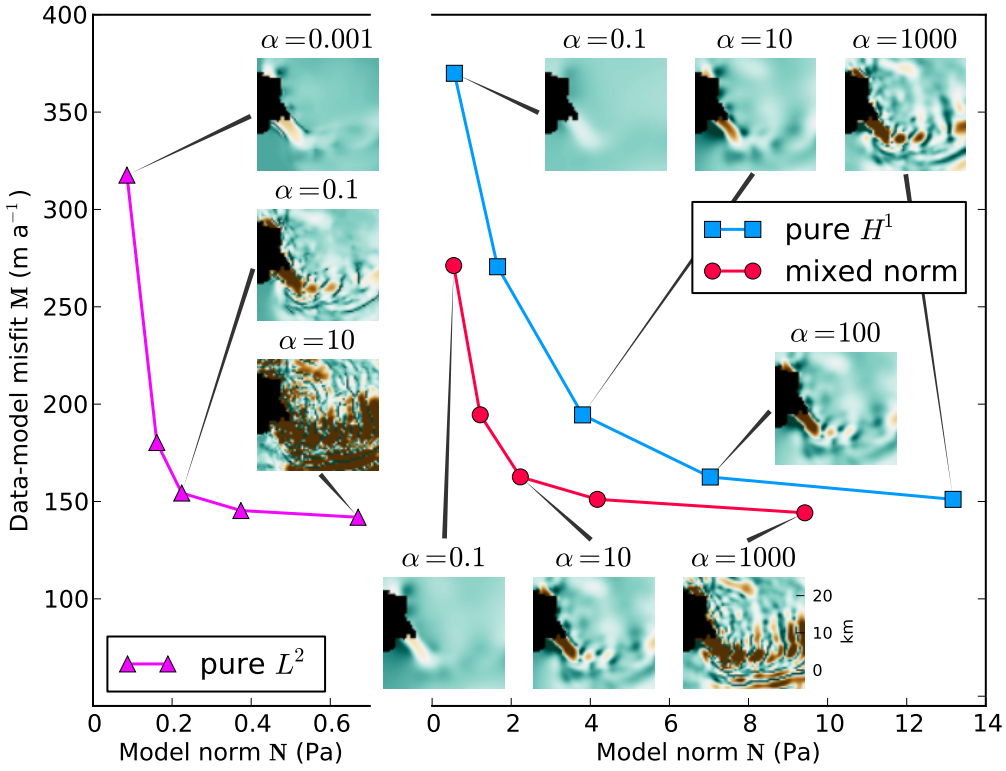

Figure 3.3. L-curves for three different model norms; pure H^1 (c_{L^2} = 0, c_{H^1} = 1), pure L^2 (c_{L^2} = 1, c_{H^1} = 0) and a mixed norm (c_{L^2} = 0.9, c_{H^1} = 0.1). All inversions are for the 2006 velocity data with ice softness A =2.5 $\times 10^{-24}$ Pa^{-3}s^{-1}. The small insets show map views of τ_c solutions for different regularization parameters to illustrate the increase in small-scale features with higher α's.

The regularization term of the cost function contains a model norm (Eq. 3.4). This term is necessary to stabilize the inversion. Choosing a model norm biases the solution and needs to be considered in the interpretation. As outlined in the Methods section (3.2.1) the type of model norm used here allows for a bias towards 1) 'small' solutions, where the departure from a prior estimate of basal yield stress is penalized, 2) 'smooth' solutions where the derivative of $\tau_c - \tau_c^{prior}$ is held small, which tends to preserve the shape of τ_c^{prior},

or 3) a mix between these two options.

Figure 3.3 shows L-curves for three different model norms: pure L^2 norm, pure H^1 norm and L^2 norm with an additional small amount of H^1 norm. By increasing α more emphasis is placed on the data-model misfit minimization and more roughness is allowed in the solution. Calculating data-model misfit values can be computationally expensive because each data point requires an inversion run and the inversions with very high α take many iterations to converge. We show examples of modeled basal yield stress for under- and overfitting of the data, as well as a solution for the approximate 'corner' of the L-curve. The corner of the pure H^1 norm is at a data-model misfit approximately 50 m/a higher than the corner of the pure L^2 norm, and the basal yield stress field of the H^1 norm results in an accordingly smoother solution. All chosen model norms result in L-curves with different values for α at their corners, but with similar limits for data-model misfits. This can be an indication of the total error, T^{tot}, in the system.

The pure L^2 norm produces large jumps in basal yield stress, especially with higher regularization parameter values, making it more sensitive to the choice of α. Here we prefer the pure H^1 norm solution because the non-localized nature of the SSA does not account for small-scale features in basal yield stress. Additionally, as long as the regularization parameter is chosen to yield similar data-model misfit values, the choice of norm influences the solution only within an acceptable range (see Section 3.5.1).

3.3.3 Prior estimate

In Tikhonov regularization, the cost function (Eq. 3.2) is minimized, and a prior estimate of basal yield stress is necessary as a starting point for the iterations and for the model norm term. Within the misfit area the latter seems to outweigh the former. A prior estimate commonly used in glaciology is the driving stress field divided by two [Joughin et al., 2004]. This choice was suggested because in the Shallow Ice Approximation the driving stress is locally balanced by the basal shear stress, but this is not necessarily the case for the SSA, where membrane stresses are considered.

Figure 3.4 shows two Tikhonov inversions with the prior estimate set to $\tau_d/2$ and to a constant value, respectively. Both of the resulting basal yield stress fields lead to almost identical residual velocity fields; in other words both solutions can account for the main features of the observed velocities. Small scale features that are introduced in the $\tau_d/2$ prior estimate remain unchanged because they do not affect the velocity field sufficiently. The

commonly used L^2 norm was applied for this figure; the H^1 norm would exacerbate the problem because the shape of the initial estimate tends to be preserved.

Without prior knowledge about the basal shear stress a constant prior estimate is most appropriate to avoid introducing small scale features that may not be real. For the pure H^1 model norm adding a constant value to τ_c^{prior} will not influence the solution inside the misfit area. But we find that the inversion converges only for values within a certain range (approximately 5×10^4 - 8×10^5 Pa). Therefore a good prior estimate could be the average of τ_d inside the misfit area (here: $\overline{\tau_d} \approx 1 \times 10^5$ Pa). Here we performed an inversion and used the value of modeled basal yield stress along the centerline at the upstream edge of the misfit area as the prior estimate (1.4×10^5 Pa). In this way the algorithm does not have to introduce extreme basal shear stress values to compensate for values outside the misfit area that lead to wrong ice velocities. All prior estimates in the remainder of this study were set to 1.4×10^5 Pa.

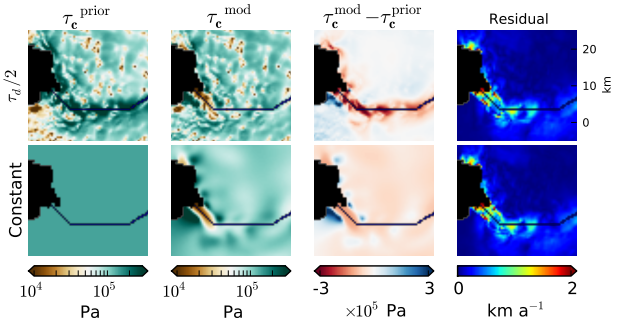

Figure 3.4. Influence of different prior estimates. Inversions with 2006 velocity data and a prior estimate of basal yield stress of Top) $\tau_c^{prior} = \tau_d/2$ and Bottom) $\tau_c^{prior} = 1.4 \times 10^5$ Pa. The columns show the prior estimate, the inferred basal yield stress, the change of the prior to the modeled τ_c and the residual in velocity ($|\mathbf{u}^{obs} - \mathbf{u}^{mod}|$). Pure L^2 model norm, $\alpha = 0.1$.

3.3.4 Regularization parameter

Given the choice of parameters discussed above, the L-curve criterion can now be used to choose the appropriate regularization parameter, α. Commonly the L-curve is displayed as a log-log plot, but for our inverse problem no clear corner emerges (not shown). There are different reasons for the lack of corner in the L-curve, one of which is an increase in problem size [Hansen, 2001]. As suggested by Calvetti et al. [2000] it is acceptable to

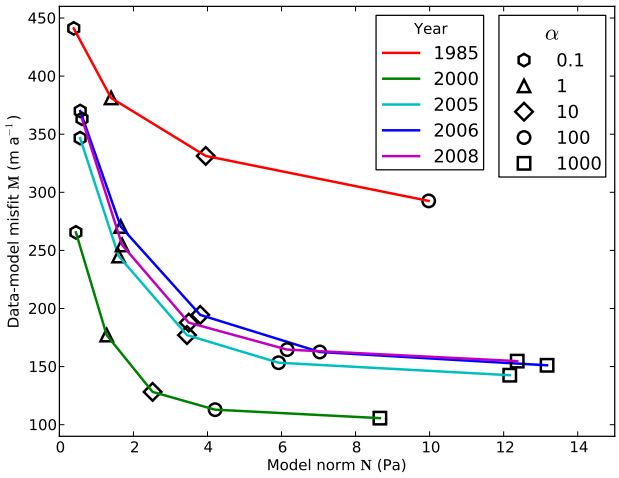

Figure 3.5. L-curves for all years plotted on a linear scale. The range of regularization parameters is $\alpha = 0.1$ - 1×10^3. Based on this figure $\alpha = 10$ is chosen for all years.

plot data-model misfit against model norm on a linear scale to find the corner of the L-curve. Figure 3.5 shows the linear plot of the L-curve for all years with the above chosen parameters. We choose a regularization parameter of $\alpha = 10$ for all years based on this figure.

Data-model misfit values in Figure 3.5 do not reach below $100\,\mathrm{m\,a^{-1}}$, which is much higher than the expected root mean square error in surface velocity observations; assuming a 3% error [Joughin et al., 2012] the root mean square error over the misfit area is $\sim 7\,\mathrm{m\,a^{-1}}$. Errors are thus dominated by those introduced by the simplified model and/or geometry input fields. The high data-model misfit ensures that no overfitting of the observed surface velocity data occurs, but overfitting due to the model and parameter errors would still be a possibility without the regularization term. Since T^{obs} is much smaller than the data-model misfit we use the L-curve method to improve parameters of the model such as the ice softness.

3.4 Results

Inversions for all years with the parameter choices discussed above are shown in Figure 3.6. All inversions reproduce the overall pattern of observed surface velocities. This shows that, in general, our data and model choices are capable of reproducing the observations by only adjusting basal yield stress. But a small data-model misfit by itself does not speak

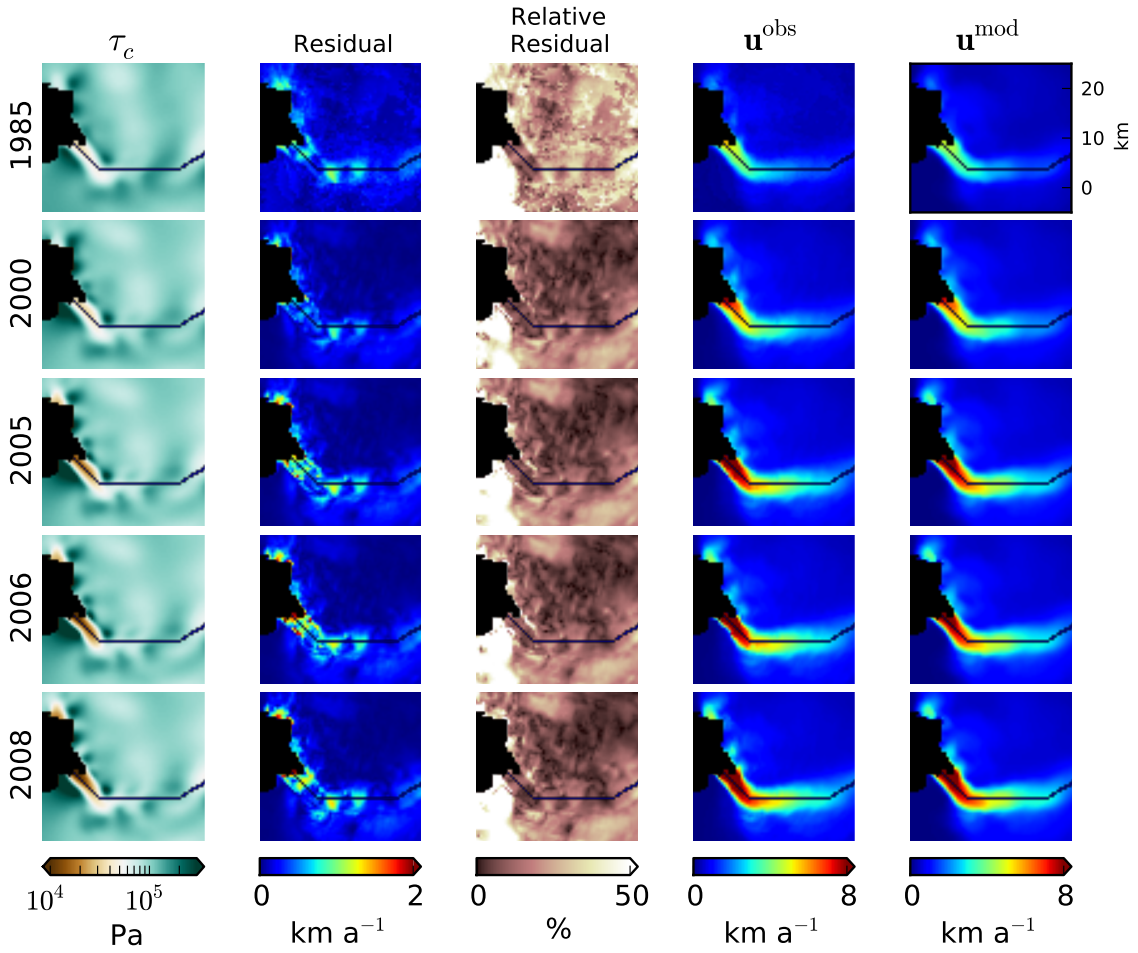

Figure 3.6. Inversion results for 1985, 2000, 2005, 2006 and 2008. The columns show the modeled τ_c (logarithmic scale), the velocity residual ($|\mathbf{u}^{obs} - \mathbf{u}^{mod}|$), the relative velocity residual ($100\,|\mathbf{u}^{obs} - \mathbf{u}^{mod}|/\mathbf{u}^{obs}$), the observed velocities $\mathbf{u}^{obs}$ and the modeled velocities $\mathbf{u}^{mod}$. The area past the 2008 grounding line is not included in the misfit area and is blacked out.

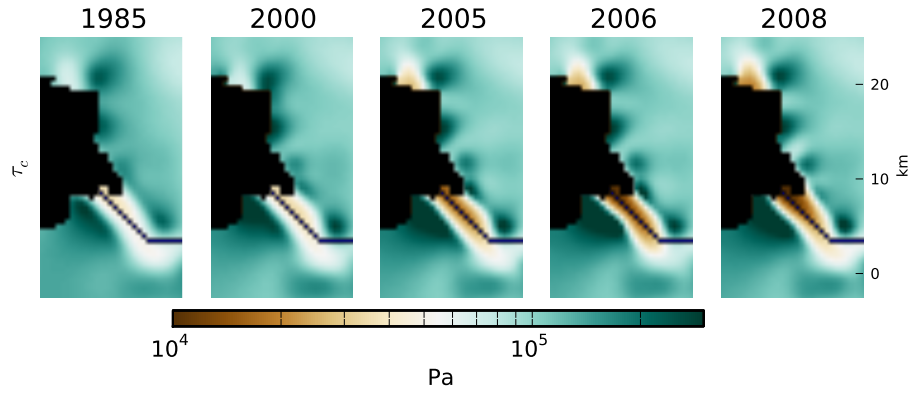

Figure 3.7. Close-up of inversion results for 1985, 2000, 2005, 2006 and 2008. The columns show the modeled τ_c for each year. The area past the 2008 grounding line is not included in the misfit area and is blacked out.

to the quality of the resulting basal yield stress solution.

The first leg (lower 5 km of the glacier) shows a trend from higher to lower basal yield stresses over the years. Additionally, a slight widening of the area with low basal yield stresses is evident. The 2008 inversion results show continued widening, but the low basal yield stress area does not extend as far inland as in the 2006 results. Despite the use of independently produced DEMs and observed surface velocity data sets, the general spatial distribution of basal yield stress outside of the main fast flowing glacier remains fairly constant in all inversions compared to the large changes in the first leg. This consistency across years in areas with minimal observed changes in geometry and flow is encouraging and justifies the use of constant parameters for all inversion runs.

Our main area of interest is the lower glacier with the largest changes in basal yield stress across the years. This area entails high values of observed surface velocities and a deep trough in the bed topography. Residual velocities (difference of modeled and observed) are generally high in this area of fast flow, but relative residuals are in fact similar or lower than in the slow flowing areas (Figure 3.6).

To compare the results for the different years in more detail Figure 3.8 shows the results along the centerline for all years. Here the basal shear stress, τ_b, calculated according to Eq. 3.1, is shown and compared to the driving stress. As seen in the spatial distribution of basal yield stress, the values in the first leg are clearly lowered compared to higher upstream, and they generally decrease over time. Despite minimal changes in driving stress from

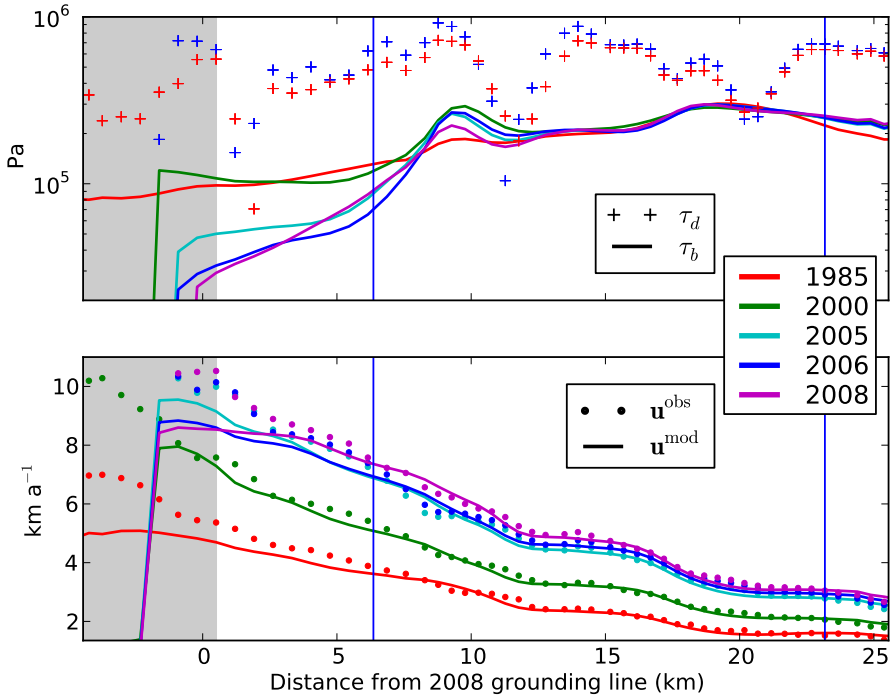

Figure 3.8. Inferred basal shear stress along centerline for all years. Area outside of misfit area is shaded gray and the blue vertical lines show the position of the two bends in the centerline. Top) Crosses mark the driving stresses, τ_d, for the years 1985 and 2006. The sharp peak in τ_b occurs at the grounding line for each year. Bottom) Modeled (solid lines) and observed (points) velocities for all years.

1985 to 2006 the basal shear stress changes significantly over this time period. In 2000 only a lowering close to the first bend is visible, whereas basal shear stress close to the terminus increases compared to 1985. Past the first bend, the inverted basal shear stresses are generally higher; for 2008 the average value of τ_b in the first leg is 0.2×10^5 Pa, whereas the average value between the first and the second bend is 1.8×10^5 Pa. Upstream of the first leg no clear trend in basal shear stress is visible, which is in contrast to the general increase in basal shear stress in this area inferred by Joughin et al. [2012]. The basal shear stress accounts for about 20-40% of the driving stresses along the entire centerline, with a few single peaks reaching 80-100% of the driving stresses.

3.5 Discussion

3.5.1 Robustness of inversion

The solution to our inverse problem is not unique, many of the parameters are not well constrained and a range of parameter choices would be equally acceptable. The emphasis here is on temporal changes in basal yield stress, and little significance should be given to the actual value of the stress in a given inversion. To evaluate the robustness of our results we explore a range of parameters for the years 1985 and 2006.

We chose an ice softness value of 2.5×10^{-24} $\text{Pa}^{-3}\text{s}^{-1}$ for all years, while the minimum data-model misfit values are reached for ice softness values between 2 and 3×10^{-24} $\text{Pa}^{-3}\text{s}^{-1}$ (see Fig. 3.2). Figure 3.9 shows an envelope of solutions of basal yield stress along the centerline for this range of ice softness. The solutions for $A = 3 \times 10^{-24}$ $\text{Pa}^{-3}\text{s}^{-1}$ lead to generally higher τ_c values than the $A = 2 \times 10^{-24}$ $\text{Pa}^{-3}\text{s}^{-1}$ solutions, because softer ice leads to a more localized stress balance and therefore to higher values in basal yield stress. The 2006 basal yield stress solution exhibits a higher sensitivity to changes in ice softness and the basal yield stress is affected most just upstream of the first bend. It is important to keep in mind that we are using a constant value of ice softness over the entire model domain. Larger variations of basal yield stress are possible for more realistic representations of the temperature distribution in the ice. As a thermomechanically-coupled ice sheet model, PISM is capable of producing realistic ice temperature fields, which could be achieved through spin-ups. But it is not clear which basal yield stress values to use for such a spin-up. Joughin et al. [2009] for example used iterative spin-ups to find an ice temperature field that is consistent with the basal yield stress.

One of the most important sources of uncertainty is the choice of regularization pa-

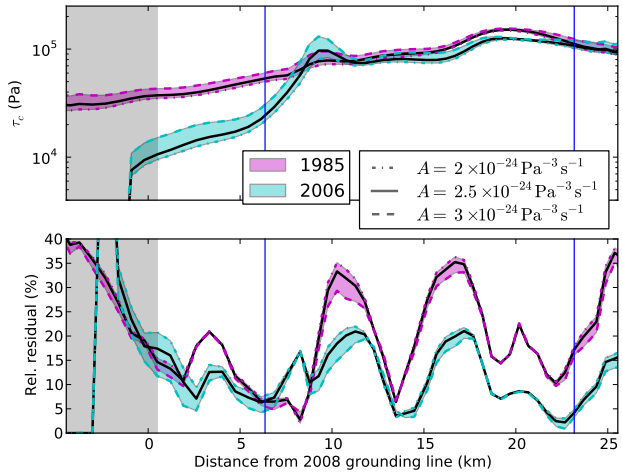

Figure 3.9. Robustness of basal yield stress results for a range of ice softness values (same centerline as Fig. 3.8). Top: Softness values of 2×10^{-24} $\mathrm{Pa}^{-3}\mathrm{s}^{-1}$ and 3×10^{-24} $\mathrm{Pa}^{-3}\mathrm{s}^{-1}$ are shown as lower and upper envelopes, respectively, the black line indicates the 2.5×10^{-24} $\mathrm{Pa}^{-3}\mathrm{s}^{-1}$ solution for both years. Bottom: Data-model misfit of velocities relative to observed speed for the range of ice softnesses.

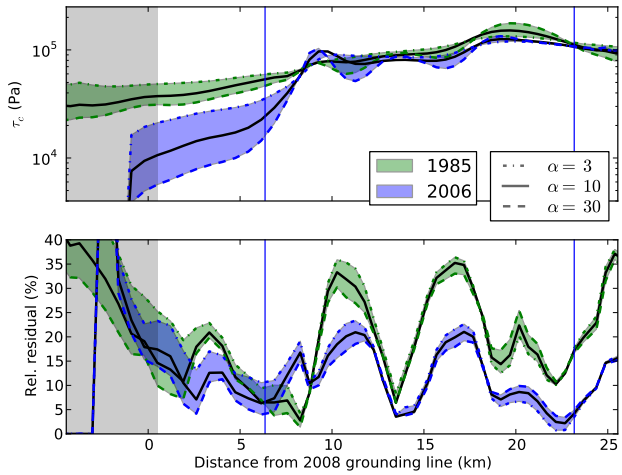

Figure 3.10. Robustness of basal yield stress for regularization parameter values, $\alpha = 3$ (upper envelope) and $\alpha = 30$ (lower envelope), the black line indicates the $\alpha = 10$ solution.

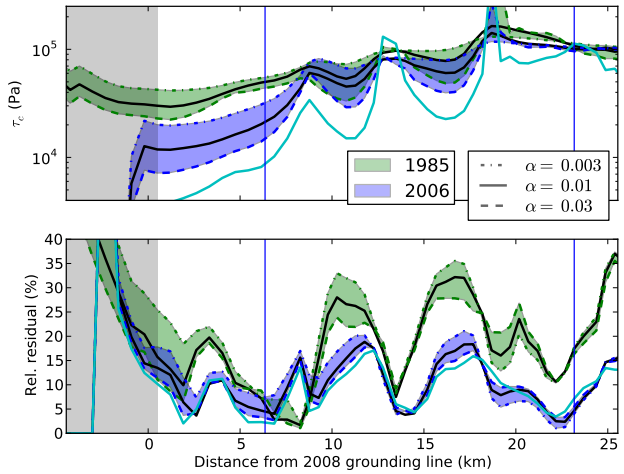

Figure 3.11. Robustness of basal yield stress results for L^2 norm with the conservative regularization parameter values $\alpha = 0.003$ (upper envelope) and $\alpha = 0.03$ (lower envelope), the black line indicates the $\alpha = 0.01$ solution. The actual corner of the L^2 L-curve is at $\alpha = 0.1$ and the solution for this regularization parameter is shown in cyan.

rameter. As mentioned before, it is not straight forward to choose the exact location of the 'corner' in the L-curve. In other studies the regularization parameter is chosen by calculating the point of maximum curvature [Vogel, 1987, ch. 7.4]. But even when this point is calculated exactly, the L-curve criterion remains an approximate method. Therefore, we chose the approximate value of $\alpha = 10$ and an upper and lower bound ($\alpha = 3$ and $\alpha = 30$). Figure 3.10 shows that the choice of regularization parameter mostly affects the first leg where a smaller data-model misfit in velocities is expensive (in the model norm sense) because the narrow trough makes abrupt changes in τ_c necessary. The data-model misfit is a root mean square over the misfit area, meaning that local under- or overfitting is possible (and very probable). When plotting the data-model misfit relative to $\mathbf{u}^{obs}$ along the centerline for different regularization parameters (Fig. 3.10) it becomes clear that in the first leg the fit to velocity observations is still improving, unlike in areas higher upstream. A higher α could be justified when focusing on the inversion results of τ_c in the first leg.

We also want to investigate how a different choice of model norm would have affected our solution. For a direct comparison with the range of regularization parameters used for Figure 3.10 we chose a conservative $\alpha = 0.01$ as the 'ideal' solution and a range from $\alpha = 0.003$ to $\alpha = 0.03$ (Fig. 3.11). The sharp features in τ_c for $\alpha = 0.03$ between the two bends reach values of 4.1×10^5 and 2.6×10^5 Pa for 1985 and 2006, respectively, showing the

sensitivity of this norm to overfitting. Note that the relative residual does not improve significantly even though such large features are introduced. The actual corner of the L^2 L-curve is at $\alpha = 0.1$ and the solution for this regularization parameter is shown as well in Figure 3.11. The value of the modeled τ_c is generally lower in this case and displays sharper features, while the improvement in relative residual is not significant.

To illustrate how a prior estimate with small scale features can influence the solution, Figure 3.12 shows the centerline solutions for a prior estimate of $\tau_d/2$. When using prior estimates with small scale features, the L^2 norm is more useful because it does not try to conserve the shape of the prior estimate. The centerline solution only contains fast flow, where τ_c is adjusted well, in slow flow areas there are more places where the small scale features of the prior estimate remain. Half of the driving stress might be a good first order approximation of basal yield stress, but when applied un-smoothed as a prior estimate, it introduces spurious features. To initialize entire or drainage basin wide ice sheet models a continuous field of basal yield stress is needed. The inversion algorithm only calculates the data-model misfit where surface velocity observations are available. This can lead to large areas where the prior estimate will determine the final τ_c. Future work should consider what the best strategies for the prior estimate in such situations are. To compare inverse results of different years, ideally we would use inverse methods where the cost function also includes a penalization for changes in time as done in time-dependent seismic tomography [Julian and Foulger, 2010]. In this manner years with larger velocity data coverage would adjust τ_c in areas with data gaps in other years.

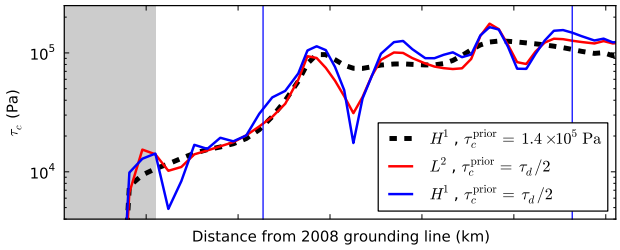

Figure 3.12. Robustness of basal yield stress for $\tau_d/2$ prior estimate. In red the L^2, $\alpha = 0.01$, $\tau_c^{\text{prior}} = \tau_d/2$ solution, in blue the H^1, $\alpha = 10$, $\tau_c^{\text{prior}} = \tau_d/2$ solution. The dashed black line indicates the H^1, $\alpha = 10$, $\tau_c^{\text{prior}} = 1.4 \times 10^5$ Pa solution for comparison.

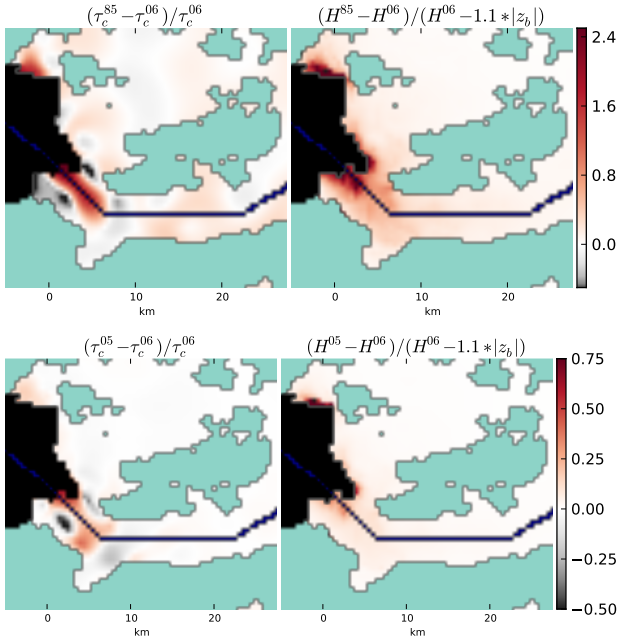

Figure 3.13. Comparison to Mohr-Coulomb parameterization. Relative change in inferred τ_c (left) compared to the change predicted by the Mohr-Coulomb parameterization used in PISM. Areas where the bed topography, z_b, is above sea level are masked out.

3.5.2 Changes in basal yield stress

Figure 3.6 shows a general decrease in basal yield stress close to the grounding line, here we explore how this relates to changes in geometry. We solely concentrate on snapshots of ice geometry and do not investigate causes of the change in geometry, such as increased melt or decreased buttressing at the ice front. In other words, the inversion examines an instantaneous stress state given a certain geometry and surface velocity, but it can, by itself, not attribute any causes

A common way to parameterize the basal yield stress in time dependent model runs is through a Mohr-Coulomb model [Iverson et al., 1998]:

$$\tau_c = \tan(\phi)\,(\rho g H - p_w), \tag{3.5}$$

where $(\rho g H - p_w)$ is the effective pressure, p_w is the pore water pressure, g is the gravitational acceleration, ρ is the density of ice (set to $917\,\mathrm{kg/m^3}$), and ϕ is a "till friction angle," a strength parameter for the till comparable to "angle of repose" for granular piles. To

find out if the changes in the inverted τ_c are in agreement with such a parametrization, we compare the relative change in τ_c (LHS of Eq. 3.6) to the relative change in height above floatation (RHS of Eq. 3.6). We assume that the basal water pressure is equivalent to oceanic pressure ($p_w = \rho_w g|z_b|$, ρ_w is the density of water and set to $1025\,\mathrm{kg/m^3}$) where the bed elevation is below sea level and $p_w = 0$ otherwise. The term $\tan(\phi)$ cancels when calculating the relative change (e.g. for 1985 and 2006):

$$\frac{\tau_c^{85} - \tau_c^{06}}{\tau_c^{06}} = \frac{H^{85} - H^{06}}{H^{06} - \frac{\rho_w}{\rho_i}|z_b|}. \tag{3.6}$$

The proximity to floatation is important in this calculation and we are subtracting 30 m (approximate offset at the 2007 terminus) from $|z_b|$ to correct for the geoid-ellipsoid separation in the area of terminus. The area of interest lies entirely in the ablation area, so that density variations due to firn do not need to be considered. Density variations caused by heavy crevassing, however, can occur, but are not considered here.

Figure 3.13 shows that the relative change in inferred τ_c is much more localized to the trough than the relative change in height above floatation. A slight increase in τ_c is visible near the margins of fast flow. But the broad pattern is similar, confirming that the relative change in height above floatation accounts for most of the relative changes in τ_c. Also for shorter time scales and after the disintegration of the floating ice tongue (2005-2006) similar patterns of relative change are visible (Fig. 3.13)). An increase in sliding due to more melt water at the base, for example, would lead to a spatial pattern of relative change distributed over the entire area of melt. Because we do not see this spatial pattern related to melt area, our results support the findings of Joughin et al. [2008a] that increase in seasonal melt is not the main driver of the observed speedup.

Figure 3.14 shows how the relative change in inferred τ_c (LHS of Eq. 3.6) and the predicted relative change in height above floatation (RHS of Eq. 3.6) compare along the centerline. The relative changes in inferred τ_c are shown for a range of regularization parameters and ice softnesses. The relative change in height above floatation has a different qualitative shape, but falls within the envelope of regularization parameters. The choice of regularization parameter gives a large uncertainty in relative changes in τ_c, especially in the terminus area. Above we showed that there is a significant lowering in τ_c in the first leg, even when taking into account the uncertainties introduced by the parameter choices in the inversion. Figure 3.14 on the other hand, shows that these same uncertainties of

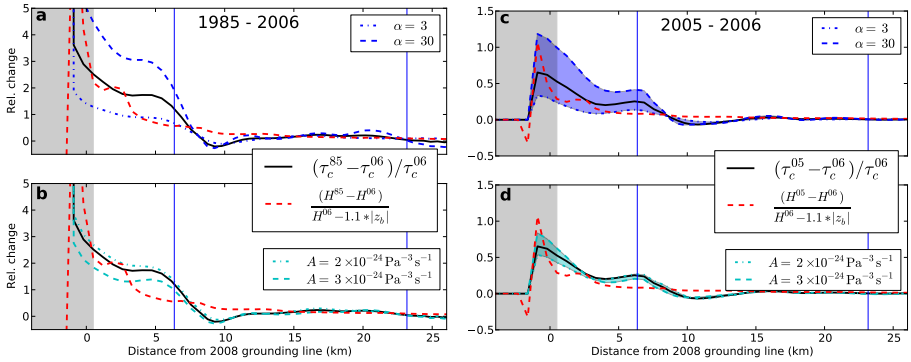

Figure 3.14. Relative change in inferred τ_c along the centerline for a range of regularization parameters (top) and ice softnesses (bottom). The red line shows the change in height above floatation predicted by the Mohr-Coulomb parameterization used in PISM. a) compares years 1985 and 2006, b) compares the years 2005 and 2006.

the inversion method make it difficult to judge the validity of parameterizations for τ_c (Eq. 3.5).

To investigate if using a constant-in-time value for the till friction angle ϕ is reasonable, we plot the inferred value of τ_c against the predicted effective pressure for each grid point. In areas with a constant till friction angle we would expect a linear relationship between τ_c and effective pressure ($\rho g H - p_w$) with a slope of $\tan(\phi)$. The overall thinning from 1985 to 2006 should lead to a decrease in effective pressure and a simultaneous decrease in τ_c. We expect the same linear relationship for both years, but with a data point cloud shifted towards lower values of effective pressure for 2006. When taking into account the entire misfit area, no relationship is apparent (Fig. 3.15), but when we limit the analyzed points to the areas of fast flow, a linear relationship emerges (Fig. 3.15). The slope of this linear fit indicates that $\tan(\phi) \approx 0.02^\circ$ and thus $\phi \approx 2^\circ$, which is a very low value of till friction angle compared to the measured values between 19° and 26° [Iverson et al., 1998; Kamb, 1991]. The consistent linear relationship in the fast flow area and the shift in data points to lower values are in agreement with the assumption of a constant $\tan(\phi)$ in time. The unphysical value of ϕ and the lack of relationship between τ_c and the effective pressure over larger spatial scales, however, show that a simple parameterization might not adequately represent the actual bed properties under Jakobshavn Isbræ. In this study we use an approximation to a perfectly plastic sliding law, therefore, τ_c is only an approximation to a basal yield stress. We test additional smaller values of q ($q = 0.1$ and $q = 0.001$) in Equa-

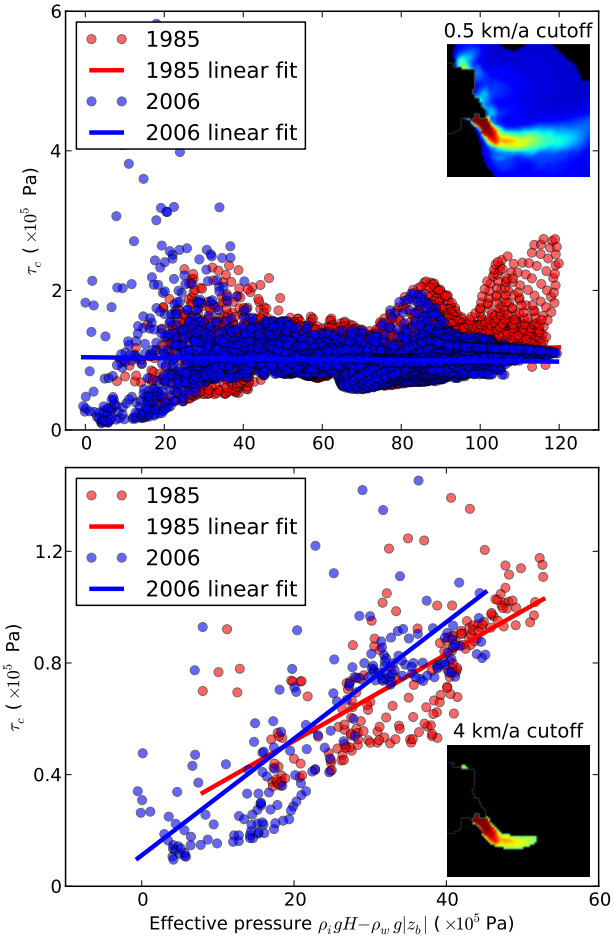

Figure 3.15. Inferred τ_c against effective pressure ($\rho gH - p_w$) for each grid point where the observed velocities are greater than the threshold velocity given above the inset plots. A linear fit is given for both years, the slope is 0.016 (0.019) and the intercept is 1.37×10^4 (0.97×10^4) for 1985 (2006).

tion 3.1 to see if a closer approximation to a plastic till affects our findings. The actual value of τ_c increases by up to 2×10^5 Pa, but the lowering of τ_c in the first 7 km during the time of acceleration is a robust result. Comparing τ_c to effective pressure leads to slightly higher values of till friction angle ($\phi \sim 3^\circ$), but these values are still low compared to measured values mentioned above. The inversion calculates the best fit to observed velocities, given an SSA forward model and the restrictions from the regularization. If results from the inversion are used in prognostic forward models that are based on the SSA, it might be more appropriate to use these inversion values, even if they differed significantly from actual *in situ* measurements of till friction angle or basal yield stress (if those were indeed measurable). In that sense, the goal of an inversion is not always to find the true physical parameters, but rather those that are consistent with a simplified physical model and the observations.

3.6 Conclusions

A careful choice of parameters in an inversion is especially important when comparing basal yield stress distributions independently inferred for different years. To estimate the influence of the parameter choices, reasonable ranges are explored and we find that the weakening of basal yield stress over the years close to the terminus area is a real temporal variation. The observed changes are in agreement with a Mohr-Coulomb parameterization of basal yield stress, where the change in effective pressure is the main driver for the changes in basal yield stress. Despite this broad agreement, the involvement of other processes cannot be excluded and the sensitivity of the inversion to parameter choices, in particular the regularization parameter, makes it difficult to evaluate basal yield stress parameterizations. The spatial distribution of residuals shows that for Jakobshavn Isbræ less simplified models, improved bed topography and/or a spatially varying ice softness could potentially improve the inversion results. With the currently available satellite data and the length of observational record on many other fast changing glacier systems it is possible to apply these methods to other systems and to further advance our understanding of the changes at the base of the ice.

3.7 Acknowledgements

This work was supported by NASA NNX09AJ38G, NSF CMG 0732602, NSF CMG 0724860, and in part by a UAF Center for Global Change Student Research Grant with funds from

the Cooperative Institute for Alaska Research and the UAF Vice Chancellor for Research, and Alaska EPSCoR. We acknowledge the use of data and data products from CReSIS generated with support from NSF grant ANT-0424589 and NASA grant NNX10AT68G, as well as Joughin, I., B. Smith, I. Howat, and T. Scambos. 2010. MEaSUREs Greenland Ice Velocity Map from InSAR Data. Boulder, Colorado, USA: National Snow and Ice Data Center. Digital media. Ian Howat acted as scientific editor and two anonymous reviewers provided detailed comments that greatly improved the manuscript. Mark Fahnestock, Constantine Khroulev, Andy Aschwanden and Ed Bueler have patiently answered questions and provided feedback.

References

Amundson, J. M., Fahnestock, M. A., Truffer, M., Brown, J., Lüthi, M. P., and Motyka, R. J.: Ice mélange dynamics and implications for terminus stability, Jakobshavn Isbræ, Greenland, J. Geophys. Res., 115, F01 005, doi: 10.1029/2009JF001405, 2010.

Aster, R., Borchers, B., and Thurber, C.: Parameter Estimation and Inverse Problems, Elsevier Academic Press, New York, 2005.

Bamber, J. L., Layberry, R., and Gogineni, S.: A new ice thickness and bed data set for the Greenland ice sheet. 1. Measurement, data reduction, and errors, J. Geophys. Res., 106, 33,773–33,780, 2001.

Budd, W. F. and Jacka, T. H.: A review of ice rheology for ice sheet modelling, Cold Reg. Sci. Technol., 16, 107–144, 1989.

Bueler, E. and Brown, J.: Shallow shelf approximation as a "sliding law" in a thermomechanically coupled ice sheet model, J. Geophys. Res., 114, F03 008, doi: 10.1029/2008JF001179, 2009.

Calvetti, D., Morigi, S., Reichel, L., and Sgallari, F.: Tikhonov regularization and the L-curve for large discrete ill-posed problems, J. Comput. Appl. Math., 123, 423–446, 2000.

Cuffey, K. M. and Paterson, W.: The Physics of Glaciers, Academic Press, Inc., Amsterdam, 4 edn., 2010.

Gillet-Chaulet, F., Gagliardini, O., Seddik, H., Nodet, M., DURAND, G., Ritz, C., Zwinger, T., Greve, R., and Vaughan, D. G.: Greenland ice sheet contribution to sea-level rise from a new-generation ice-sheet model, The Cryosphere, 6, 1561–1576, 2012.

Habermann, M.: Basal shear strength inversions for ice sheets with an application to Jakobshavn Isbrae, Greenland, Ph.D. thesis, University of Alaska, Fairbanks, in print.

Habermann, M., Maxwell, D., and Truffer, M.: Reconstruction of basal properties in ice sheets using iterative inverse methods, J. Glaciol., 58, 795–807, 2012.

Hansen, P. C.: The L-curve and its use in the numerical treatment of inverse problems, Computational inverse problems in electrocardiology, 5, 119–142, 2001.

Iverson, N. R., Hooyer, T. S., and Baker, R. W.: Ring-shear studies of till deformation: Coulomb-plastic behavior and distributed strain in glacier beds, J. Glaciol., 44, 634–642, 1998.

Jay-Allemand, M., Gillet-Chaulet, F., Gagliardini, O., and Nodet, M.: Investigating changes in basal conditions of Variegated Glacier prior to and during its 1982–1983 surge, The Cryosphere, 5, 659–672, 2011.

Joughin, I., MacAyeal, D. R., and Tulaczyk, S.: Basal shear stress of the Ross ice streams from control method inversions, J. Geophys. Res., 109, B09 405, doi: 10.1029/2003JB002960, 2004.

Joughin, I., Das, S. B., King, M. A., Smith, B. E., Howat, I. M., and Moon, T.: Seasonal Speedup Along the Western Flank of the Greenland Ice Sheet, Science, 320, 781–783, 2008a.

Joughin, I., Howat, I. M., Fahnestock, M. A., Smith, B. E., Krabill, W. B., Alley, R. B., Stern, H., and Truffer, M.: Continued evolution of Jakobshavn Isbrae following its rapid speedup, J. Geophys. Res., 113, F04 006, doi: 10.1029/2008JF001023, 2008b.

Joughin, I., Tulaczyk, S., Bamber, J. L., Blankenship, D., Holt, J. W., Scambos, T., and Vaughan, D. G.: Basal conditions for Pine Island and Thwaites Glaciers, West Antarctica, determined using satellite and airborne data, J. Glaciol., 55, 245–257, 2009.

Joughin, I., Smith, B. E., Howat, I. M., Scambos, T., and Moon, T.: Greenland flow variability from ice-sheet-wide velocity mapping, J. Glaciol., 56, 415–430, 2010.

Joughin, I., Smith, B. E., Howat, I. M., Floricioiu, D., Alley, R. B., Truffer, M., and Fahnestock, M.: Seasonal to decadal scale variations in the surface velocity of Jakobshavn Isbrae, Greenland: Observation and model-based analysis, J. Geophys. Res., 117, F02 030, doi: 10.1029/2011JF002110, 2012.

Julian, B. R. and Foulger, G. R.: Time-dependent seismic tomography, Geophys. J. Int., 182, 1327–1338, 2010.

Kamb, B.: Rheological nonlinearity and flow instability in the deforming bed mechanism of ice stream motion, J. Geophys. Res., 96, 16 585–16 595, 1991.

Konovalov, Y. V.: Inversion for basal friction coefficients with a two-dimensional flow line model using Tikhonov regularization, Research in Geophysics, 2:e11, 82–89, 2012.

Korona, J., Berthier, E., Bernard, M., Rémy, F., and Thouvenot, E.: SPIRIT. SPOT 5 stereoscopic survey of Polar Ice: Reference Images and Topographies during the fourth International Polar Year (2007–2009), ISPRS Journal of Photogrammetry and Remote Sensing, 64, 204–212, 2009.

Lüthi, M., Funk, M., Iken, A., Gogineni, S., and Truffer, M.: Mechanisms of fast flow in Jakobshavn Isbrae, West Greenland: Part III. Measurements of ice deformation, temperature and cross-borehole conductivityin boreholes to the bedrock, J. Glaciol., 48, 369–385, 2002.

MacAyeal, D. R.: The Basal Stress Distribution of Ice Stream E, Antarctica, Inferred by Control Methods, J. Geophys. Res., 97, 595–603, 1992.

Maxwell, D., Truffer, M., Avdonin, S., and Stuefer, M.: An iterative scheme for determining glacier velocities and stresses, J. Glaciol., 54, 888–898, 2008.

Meier, M. and Post, A.: Fast tidewater glaciers, J. Geophys. Res.-Solid Earth, 92, 9051–9058, 1987.

Morland, L. W.: Unconfined ice-shelf flow, in: Dynamics of the West Antarctic ice sheet, edited by Van der Veen, C. J. and Oerlemans, J., pp. 99–116, D. Reidel Publishing Company, Dordrecht, 1987.

Morlighem, M., Rignot, E., Seroussi, H., Larour, E., Dhia, H. B., and Aubry, D.: Spatial patterns of basal drag inferred using control methods from a fullStokes and simpler models for Pine Island Glacier, West Antarctica, Geophys. Res. Lett., 37, L14 502, doi: 10.1029/2010GL043853, 2010.

Motyka, R. J., Fahnestock, M., and Truffer, M.: Volume change of Jakobshavn Isbrae, West Greenland: 1985–1997–2007, J. Glaciol., 56, 635–646, 2010.

Motyka, R. J., Truffer, M., Fahnestock, M., Mortensen, J., Rysgaard, S., and Howat, I.: Submarine melting of the 1985 Jakobshavn Isbræ floating tongue and the triggering of the current retreat, J. Geophys. Res., 116, F01 007, doi: 10.1029/2009JF001632, 2011.

Munson, T., Sarich, J., Wild, S., Benson, S., and Curfman McInnes, L.: TAO 2.1 Users Manual, Tech. Rep. ANL/MCS-TM-322, 2012.

Payne, A. J., Vieli, A., Shepherd, A. P., Wingham, D. J., and Rignot, E.: Recent dramatic thinning of largest West Antarctic ice stream triggered by oceans, Geophys. Res. Lett., 31, L23 401, doi: 10.1029/2004GL021284, 2004.

Petra, N., Zhu, H., Stadler, G., Hughes, T. J. R., and Ghattas, O.: An inexact Gauss–Newton method for inversion of basal sliding and rheology parameters in a nonlinear Stokes ice sheet model, J. Glaciol., 58, 889–903, 2012.

Pfeffer, W. T.: A simple mechanism for irreversible tidewater glacier retreat, J. Geophys. Res., 112, F03S25, doi: 10.1029/2006JF000590, 2007.

Plummer, J., Gogineni, S., van der Veen, C. J., Leuschen, C., and Li, J.: Ice thickness and bed map for Jakobshavn Isbræ, CReSIS, Tech. rep., 2008.

Podlech, S. and Weidick, A.: A catastrophic break-up of the front of Jakobshavn Isbrae, West Greenland, 2002/03, J. Glaciol., 50, 153–154, 2004.

Raymond, M. J. and Gudmundsson, G. H.: Estimating basal properties of ice streams from surface measurements: a non-linear Bayesian inverse approach applied to synthetic data, The Cryosphere, 3, 265–278, 2009.

Rignot, E. and Kanagaratnam, P.: Changes in the Velocity Structure of the Greenland Ice Sheet, Science, 311, 986–990, 2006.

Schoof, C. G. and Hindmarsh, R. C.: Thin-film flows with wall slip: an asymptotic analysis of higher order glacier flow models, Q. J. Mech. Appl. Math., 63, 73–114, 2010.

Sohn, H.-G., Jezek, K. C., and van der Veen, C. J.: Jakobshavn Glacier, West Greenland: 30 years of spaceborne observations, Geophys. Res. Lett., 25, 2699–2702, 1998.

Thomas, R. H., Abdalati, W., Frederick, E., Krabill, W. B., Manizade, S., and Steffen, K.: Investigation of surface melting and dynamic thinning on Jakobshavn Isbrae, Greenland, J. Glaciol., 49, 231–239, 2003.

Truffer, M.: The basal speed of valley glaciers: an inverse approach, J. Glaciol., 50, 236–242, 2004.

Truffer, M. and Fahnestock, M.: Rethinking ice sheet time scales, Science, 315, 1508–1510, 2007.

Van der Veen, C. J., Plummer, J., and Stearns, L.: Controls on the recent speed-up of Jakobshavn Isbræ, West Greenland, J. Glaciol., 57, 770–782, 2011.

Vogel, C. R.: Computational methods for inverse problems, vol. 23, SIAM Series Frontiers in Applied Mathematics, Philadelphia, 1987.

Weidick, A., Oerter, H., Reeh, N., Thomsen, H. H., and Thorning, L.: The recession of the Inland Ice margin during the Holocene climatic optimum in the Jakobshavn Isfjord area of West Greenland, Global Planet. Change, 2, 389–399, 1990.

Chapter 4
Residual patterns, resolution and sensitivity of basal yield stress inversions for Jakobshavn Isbræ, Greenland [1]

Abstract

For glaciers and ice sheets, the basal interface is not directly observable, except for rare localized access points. Geophysical inverse methods are used to infer parameters at the basal interface from surface observations of velocity. Such methods can be used to infer physical parameters from observations, but they can also provide additional information about potential inadequacies of the forward model used to relate the parameters to the observations. The observations may contain insufficient information to reject large and physically unrealistic oscillations in the inferred parameters, and spurious structures can appear in the solution. Therefore, we must stabilize, or regularize, the solution to find a preferred model. In an ideal world, where we can perfectly characterize our physical model, an inverse problem can be regularized so that the difference between modeled and observed surface velocities reflect the error in observations. However, deficiencies in the forward model result in additional errors. The velocity residual (modeled minus observed) and its spatial pattern have the potential to distinguish the main error sources for a given problem. In this study, we calculate residual patterns from synthetic inversions with different error sources and compare these residual patterns to residual patterns from real inversions to deduce the error sources for Jakobshavn Isbræ, Greenland. Synthetic tests with prescribed checkerboard patterns of basal yield stress with varying length scales are used to investigate the weighting of the data-model misfit and the ability of the inversion to resolve details in basal yield stress. We then test real-data inversions for their sensitivities to prior estimate, forward model parameters, data gaps, and temperature fields. We find that velocity observation errors are not sufficient to explain the residual patterns of real-data inversions. Conversely, ice geometry errors and especially errors in model simplifications are capable of reproducing similar patterns and magnitudes. In the upstream parts of the drainage basin, the resolution strength of inferred basal yield stress is limited, and the inferred solution depends critically on the initial estimate used in the inversion.

[1] To be submitted to *Journal of Glaciology* as Habermann, M., M. Truffer, D. Maxwell, Residual patterns, resolution and sensitivity of basal yield stress inversions for Jakobshavn Isbræ, Greenland

4.1 Introduction

Due to the changing climate, our ability to predict centennial-scale future ice sheet behavior through modeling has received considerable attention. These predictions are benefiting from an increasing amount of ground-based and remote-sensing observations and improving capabilities of ice-flow models. Advancements in numerical methods and in computing power are starting to make full-order stress solutions of ice flow on ice-sheet scales possible [*Alley and Joughin*, 2012]. Depending on the scientific questions, different data resolutions and model complexities are needed. For many questions, it is unclear whether the data or the model need improvement, for example, to what extent would a finer grid of observations or a more complex model improve the ability to answer the question at hand.

Inverse methods are used to infer parameters from observations assuming a numerical model that describes how the parameters are related to the observations. The process of solving an inverse problem is often unstable, for example, a small change in observations can lead to a large change in the reconstructed parameters. This leads to the predicament that even small errors in observations can lead to unphysical changes in the reconstructed parameters when the observations are matched too closely. This overfitting can occur because of errors in the observations, but also because of errors in the physical model used to describe the physical system, in our case, the ice flow. It is usually possible to stabilize the inversion by imposing additional constraints that bias the solution, a process that is generally referred to as regularization [*Aster et al.*, 2005]. When the inversion is properly regularized, the field of data residuals, $\|d^{\text{obs}} - d^{\text{mod}}\|$, contains information about the error in the system. Residuals that are much larger than the expected errors in observations indicate problems in the ice-flow model assumptions, inputs, or geometry that are large enough to prevent a more accurate representation of observations when only one parameter can be adjusted. In this sense, residuals and residual patterns have the potential to identify sources of errors in a system, and to guide data and modeling campaigns.

Jakobshavn Isbræ, one of the largest outlet glaciers on the west coast of Greenland has received a lot of attention due to its rapid changes in the beginning of this century [e.g. *Thomas et al.*, 2003; *Podlech and Weidick*, 2004; *Joughin et al.*, 2004]. The importance of the dynamic behavior of outlet glaciers became clear and caused a surge of data campaigns and modeling efforts, especially for the Jakobshavn Isbræ drainage basin [e.g. *Holland et al.*, 2008; *Joughin et al.*, 2008; *Amundson et al.*, 2008; *Motyka et al.*, 2010; *Joughin et al.*, 2012]. Nevertheless, Jakobshavn Isbræ remains a challenging glacier to study. The deep trough

with its steep sides makes it difficult for radar surveys to receive clear bed returns [*Bamber et al.*, 2013], and this ice geometry also makes it difficult to use simplified models that are based on shallowness. When inverting for basal conditions, the velocity residuals in the deep trough are larger than velocity observation errors, and in this study we investigate if sources of error can be determined with the help of the residual pattern.

In *Habermann et al.* [2013] basal yield stress inversions of Jakobshavn Isbræ for multiple years were performed and the changes in the first ∼20 km from the terminus were examined. Here, we extend the area of interest but focus on the velocity residuals and residual patterns. In a series of synthetic experiments, the velocity residual pattern and magnitude for surface velocity, ice geometry and modeling errors is examined. These experiments all concentrate on the terminus region (first ∼100 km) where the residuals are high in real data inversions.

Away from the terminus and the deep trough, residual values are small and the residual patterns suggest that the errors in velocity observations are the main cause for the mismatch. It is unclear, however, how far upstream basal yield stress can be resolved with present day ice velocities. To address this question, we switch to drainage-basin-wide synthetic experiments to investigate the resolution strength with different checkerboard patterns of synthetic basal yield stress. Finally, real-data inversions are performed over the entire drainage basin, focusing on the sensitivity to different models and prior estimates. We discuss self-consistency of ice geometry and model and how this affects inversion results.

4.2 Methods

The quantitative model, also called 'forward model', describes how direct measurements, here instantaneous surface velocities $\mathbf{u}$, would be predicted from a set of physical parameters, here the basal yield stress τ_c. The forward model thus contains a chosen simplification of ice flow, including some physical properties that are assumed to be known: ice softness B, Glen's flow law parameter n, density of ice ρ_{ice} and gravitational acceleration g. Here, the geometry input fields are part of the forward model: ice thickness H and ice surface elevation z_s are prescribed. Henceforth, we separate these effects and refer to the ice flow simplification and the physical properties as the 'model' and we describe the ice-geometry input fields separately.

The Parallel Ice Sheet Model (PISM) is a 3-D thermomechanically coupled ice sheet

model that solves a combination of the Shallow Ice and Shallow Shelf Approximations, here called the 'hybrid model' [*Bueler and Brown*, 2009]. The Shallow Shelf Approximation (SSA) [*Schoof and Hindmarsh*, 2010] considers membrane (longitudinal and lateral) stresses and allows for sliding, while the Shallow Ice Approximation (SIA) considers a local stress-balance without sliding. In PISM the SSA and SIA are both calculated for each grid point and the modeled surface velocity is given as the sum. In this manner, the SSA is used as a 'sliding law' and the transition from mostly sliding to non-sliding occurs without inconsistencies or singularities.

The basal shear stress τ_b is parametrized through a power law:

$$\tau_b = \tau_c \frac{\|\mathbf{u}\|^{q-1}}{u_{\text{threshold}}^q} \mathbf{u}, \tag{4.1}$$

where $\mathbf{u}$ is the basal sliding velocity, and the threshold velocity $u_{\text{threshold}}$ is set to 100 $\text{m}\,\text{a}^{-1}$. The purely plastic case is achieved by setting $q = 0$, whereas $q = 1$ leads to the common treatment of basal till as a linearly viscous material. Here, we solve for τ_c, which has units of stress and is the basal yield stress if $q = 0$. Despite setting $q = 0.25$ for this study, we call τ_c the basal yield stress. The chosen values for q and $u_{\text{threshold}}$ used here were found to provide the best representation of observed ice motion (Bueler, personal communication, 2012). The main conclusions of this paper remain valid for different choices of q and $u_{\text{threshold}}$.

We use the hybrid model in the inversion by first calculating SIA velocities $\mathbf{u}^{\text{SIA}}$ from a given geometry and ice softness (the basal yield stress is not needed), and then subtracting $\mathbf{u}^{\text{SIA}}$ from the observed surface velocities $\mathbf{u}^{\text{obs}}$. The inversion is then run with only the SSA forward model using a target velocity of

$$\mathbf{u}^{\text{target}} = \mathbf{u}^{\text{obs}} - \mathbf{u}^{\text{SIA}}. \tag{4.2}$$

In SSA-only experiments we set $\mathbf{u}^{\text{target}} = \mathbf{u}^{\text{obs}}$. For both cases the residual is calculated as $\|\mathbf{u}^{\text{target}} - \mathbf{u}^{\text{mod}}\|$ and the relative residual as

$$\frac{\|\mathbf{u}^{\text{target}} - \mathbf{u}^{\text{mod}}\|}{\|\mathbf{u}^{\text{target}}\|}, \tag{4.3}$$

where $\mathbf{u}^{\text{mod}}$ is the modeled surface velocity at the end of the inversion. The hybrid model

is mainly applied in Sec. 4.4.2 where remote sensing observations are used.

We apply the widely used Tikhonov inversion, which defines a cost functional, $I(\tau_c, \alpha)$, with an added regularization term:

$$I(\tau_c, \alpha) = \alpha \mathbf{M}^2 + \mathbf{N}^2, \tag{4.4}$$

$$\mathbf{M}^2 = \frac{1}{\Omega} \int_\Omega \|\mathbf{u}(\tau_c) - \mathbf{u}^{\text{target}}\|^2 d\Omega \tag{4.5}$$

$$\mathbf{N}^2 = \frac{1}{\Omega} \int_\Omega \|\nabla(\tau_c - \tau_c^{\text{prior}})\|^2 d\Omega \tag{4.6}$$

where $\mathbf{M}$ is the data-model misfit, $\mathbf{N}$ is the model norm (regularization term) and α is the regularization parameter. The misfit area Ω is defined by grounded ice (determined by hydrostatic equilibrium) and the availability of velocity observations, additionally a 10 km ($\sim 10H$) border around the model domain boundary is not contained in the misfit area. The model norm in Eq. (4.6) is a Sobolov H^1 norm, which biases the solution towards smooth differences to the prior estimate. Different model norms or combinations of model norms are possible as outlined in *Habermann et al.* [2013]. The L-curve method is applied to find the appropriate value for α: the data-model misfit is plotted against the model norm, this curve typically has an L-shape and the regularization parameter value corresponding to the "corner" of the curve is chosen. The rationale behind this choice of regularization parameter is that past this corner even a small improvement in the data-model misfit can only be achieved through a large increase in the model norm (e.g. the roughness of the solution).

In the first part of this study, synthetic experiments are performed where a given basal yield stress, τ_c^{synth}, is used in a forward model to produce a surface velocity, $\mathbf{u}^{\text{synth}}$. Different versions of the forward model are used here, with different model simplifications, physical properties or geometry input fields. The synthetic surface velocity is then applied as $\mathbf{u}^{\text{target}}$ in an inversion, either as is, or with added noise. All synthetic experiments then invert for τ_c given $\mathbf{u}^{\text{target}}$ with the ice geometry given by bed topography from *Plummer et al.* [2008] and a 2006 surface DEM. This 2006 DEM is produced with a 2007 DEM [*Motyka et al.*, 2010] and annual elevation-difference maps from *Joughin et al.* [2012] for $\sim$ 100 km around the terminus. In the remainder of the drainage basin we used the *Bamber et al.* [2001] DEM (for details see *Habermann et al.* [2013]). The prior estimate for the basal yield stress is set to $\tau_c^{\text{prior}} = 1.4 \times 10^5$ Pa, the H^1 norm is used as the model norm $\mathbf{N}$, the Glen's flow law

parameter is set to $n = 3$, the ice softness is set to $A = 2.5 \times 10^{-24}$ $\mathrm{Pa}^{-3}\mathrm{s}^{-1}$ and the SSA is used as a forward model (see *Habermann et al.* [2013] for a justification of these choices). We call this setup the 'reference' inversion, with reference ice geometry and physical properties.

4.2.1 Data

For the inversions in Section 4.3.1 and 4.4, where our analysis is limited to the terminus area, we use NASA's Making Earth System Data Records for Use in Research Environments (MEaSUREs) velocity map for the winter 2006-2007 [*Joughin et al.*, 2010]. In later inversions of the entire drainage basin we prefer a more complete data set of surface velocities and therefore, we use an average of winter velocities for 2000, 2006-2009 [*Joughin et al.*, 2010]. The reference inversion is performed with the bed topography given by *Plummer et al.* [2008]. In section 4.3.1 we use a newer bed topography data set (Gogineni, Prasad. (2012), CReSIS Radar Depth Sounder Data, Lawrence, Kansas, USA. Digital Media. `http://data.cresis.ku.edu/`) to simulate errors in bed topography.

4.3 Experiments

In section 4.3.1 velocity residuals are investigated and we use a model domain limited to the terminus area of Jakobshavn Isbræ. Experiments on this limited model domain are performed on a uniform 500 by 500 m grid. In later sections the entire drainage basin is used, as determined from the surface topography and an assumption of downhill ice flow. We expand the drainage basin to make it a rectangular domain that contains it entirely, and solutions are found on this simpler domain. Inversions on this larger rectangular domain are performed on a uniform 1 by 1 km grid. For the limited model domain we assume a constant ice softness; for the entire domain we tested constant ice softnesses as well as ice softness fields derived from spin-ups. Table 4.1 and Table 4.2 contain summaries of the experiments that we performed.

4.3.1 Velocity Residual Pattern

In *Habermann et al. [2013]* we show that even though the residuals in the trough close to the terminus are high, the relative residuals in the area of interest when studying the rapid changes close to the terminus are small. When we restrict ourselves to the 2006 inversion, but extend our field of view and plot the residuals on a log scale, distinct patterns in resid-

ual become visible (Fig. 4.1). With the following set of experiments we want to investigate which of the possible sources of error is most likely causing these residual patterns.

Different $\mathbf{u}^{\text{target}}$ are produced by means of adding noise to the synthetic velocities, by using different input parameters to produce the synthetic velocities, and by using different forward models (Table 4.1). For all experiments in this section τ_c^{synth} is set to the τ_c^{mod} in Figure 4.1. The different $\mathbf{u}^{\text{target}}$ are then used in a reference inversion and the resulting τ_c^{mod} and velocity residuals are investigated.

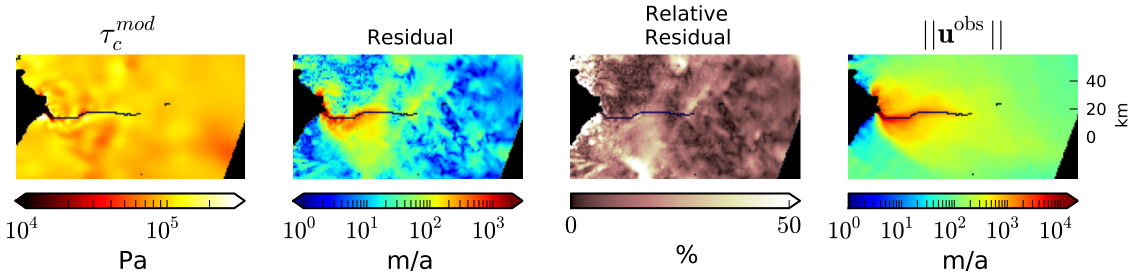

Figure 4.1. Real-data inversion and residual pattern for the 2006 surface velocities. The columns show modeled basal yield stress, residual ($||\mathbf{u}^{\text{obs}} - \mathbf{u}^{\text{mod}}||$), relative residual ($||\mathbf{u}^{\text{obs}} - \mathbf{u}^{\text{mod}}||/||\mathbf{u}^{\text{obs}}||$) and observed velocities.

Surface velocity errors

First, the influence of noise in the surface velocity observations is examined. For all four experiments in this category the reference ice geometry and model are used to produce $\mathbf{u}^{\text{synth}}$, then different types of noise are added (Table 4.1). Experiment 1 is performed without added noise for comparison. Experiment 2 adds a Gaussian distribution for random uncorrelated surface velocity errors with standard deviation of $5\,\text{m}\,\text{a}^{-1}$. Experiment 3 uses a Gaussian distribution of surface velocity errors that is scaled with the magnitude of the surface velocities ($\mathbf{u}^{\text{synth}}$). Experiment 4 adds a Gaussian distribution of surface velocity errors scaled and smoothed with a 1 km Gaussian kernel to approximate the stated observed velocity error.

Figure 4.2 shows results for all four experiments. Experiments 2 and 3 reproduce τ_c^{synth} very well, with larger discrepancies in the trough close to the terminus for experiment 3 and in the slow flow areas for experiment 2. When mimicking the velocity errors given in the observations (exp. 4) the relative difference between τ_c^{mod} and τ_c^{synth} increases even though the residual patterns suggests a better fit than in experiment 2. The residual pat-

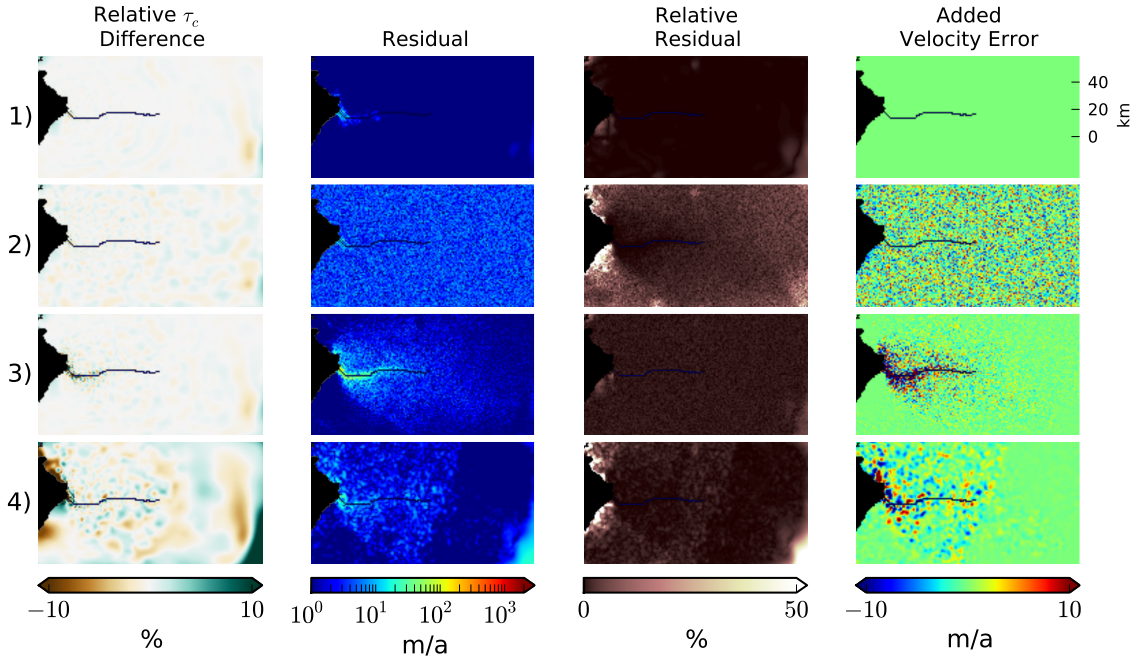

Figure 4.2. Synthetic inversions with errors in observations. The columns show the relative τ_c difference ($(||\tau_c^{\text{synth}} - \tau_c^{\text{mod}}||)/\tau_c^{\text{synth}}$), the residual ($||\mathbf{u}^{\text{target}} - \mathbf{u}^{\text{mod}}||$), the relative residual ($||\mathbf{u}^{\text{target}} - \mathbf{u}^{\text{mod}}||/||\mathbf{u}^{\text{target}}||$), and the added velocity error ($||\mathbf{u}^{\text{target}}|| - ||\mathbf{u}^{\text{synth}}||$). The rows show the different experiments: 1) inversion without added error (for comparison), 2) Gaussian noise of rms 5m/a added, 3) Gaussian noise scaled to velocity, and 4) noise according to the error values given in the observation file.

tern mirrors the pattern of added velocity error in all three experiments. The area of high relative residual (white area) on rock-terminating ice on either side of the Jakobshavn Isbræ terminus for experiments 2 and 4 suggests that high relative velocity errors in these slow flowing areas largely affect the ability to match the target velocities.

The four experiments discussed here reach very low data-model misfit values. This can be seen in the L-curves (Fig. 4.5), which show the misfit as a function of the regularizing model norm. The asymptotic value of the L-curve indicates how well observations can be fit. We conclude that realistic amounts of surface velocity errors can only account for a small amount of the data-model misfit that is observed in real-data inversions. Because the $\mathbf{u}^{\text{synth}}$ is known in these synthetic experiments, the data-model misfit can be calculated directly; for experiment 2 this value is shown in the inset of Figure 4.5.

Ice geometry errors

As a second step, we investigate the influence of errors in the surface elevation and the bed topography. In experiment 5, we add a Gaussian distribution of uncorrelated random noise with standard deviation of 5m to the surface elevation before calculating the synthetic surface velocities. In experiment 6 the CReSIS bed elevation is used. The differences between the reference fields (surface elevation and bed topography) and the synthetic fields are shown in the far-right column of Figure 4.3. As for all other synthetic experiments, the reference inversion (model and input fields) is then used to find τ_c^{mod}.

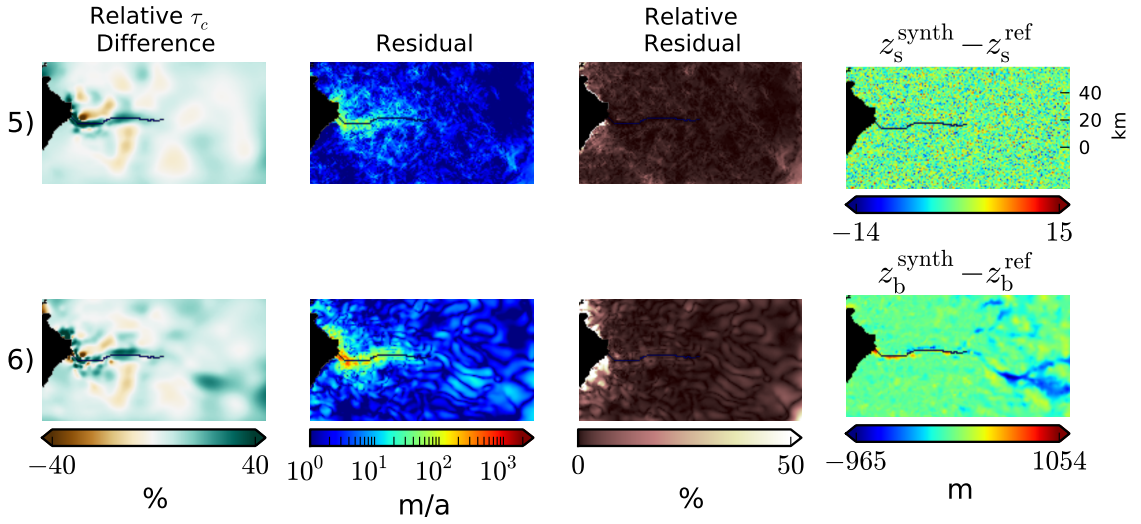

Figure 4.3. Synthetic inversions with errors in ice geometry. The columns show the relative τ_c difference ($||\tau_c^{\text{synth}} - \tau_c^{\text{mod}}||/\tau_c^{\text{synth}}$), the residual ($||\mathbf{u}^{\text{target}} - \mathbf{u}^{\text{mod}}||$), the relative residual ($||\mathbf{u}^{\text{target}} - \mathbf{u}^{\text{mod}}||/||\mathbf{u}^{\text{target}}||$), and the added geometry error in ice surface elevation/bed topography for experiments 5/6. The rows show results for experiments 5) added error in ice surface elevation (Gaussian distribution of uncorrelated random noise with standard deviation of 5m), 6) added error in bed topography by using newer CReSIS topography for forward model, then Plummer topography for the inversion.

Figure 4.3 shows the results for these two experiments. The residual fields show higher residuals in the areas close to the terminus, suggesting that ice geometry errors lead to larger residuals in the fast-flow areas compared to slow flow areas. The large topography errors in the upstream area (bottom right corner of residual plot in Fig. 4.3) are also reflected in the residual field. The modeled basal yield stress fields for both experiments show large deviations from the synthetic value because they compensate for the errors in

geometries. It is surprising how similar the deviations from τ_c^{synth} are for experiments 5 and 6 despite the vastly different errors that are introduced in the geometries. A common pattern is that τ_c^{mod} is lowered in the deep trough. In area close to the terminus, where the ice stream has a bend, the modeled basal yield stress switches from being higher and lower than τ_c^{synth} in an attempt to match the observed velocities despite the wrong ice geometry.

Figure 4.5 shows L-curves for experiments 5 and 6 with sharp corners. This shape is in contrast to the shape of the L-curve for the real-data inversion, and suggests that errors in ice geometry alone cannot recreate the shape of the real-data L-curve. The surface elevation errors lead to similarly low data-model misfit values ($\sim 6\,\text{m}\,\text{a}^{-1}$) as experiments 2 – 4, whereas the experiment with topography errors leads to data-model misfit values around $30\,\text{m}\,\text{a}^{-1}$. For both ice geometry error experiments the L-curves begin at high data-model misfits and descend rapidly, creating sharp corners that make it easy to choose the regularization parameter, nonetheless even with the large errors in topography the data-model misfit is still lower than in the real-data inversion.

Model errors

Lastly, errors in the ice-flow model are investigated. In experiment 7 Glen's flow law parameter is set to $n = 2.5$ and the constant ice softness is adjusted to $A = 1.7 \times 10^{-21}\,\text{Pa}^{-3}\,\text{s}^{-1}$ according to *Funk et al.* [1994]. For experiment 8 the synthetic surface velocities are produced with the reference ice geometry and model, but $\mathbf{u}^{\text{SIA}}$ is added before the inversion. Again, the inversion itself is then performed with the reference values (SSA-only, $n = 3$ and $A = 2.5 \times 10^{-24}\,\text{Pa}^{-3}\,\text{s}^{-1}$).

Figure 4.4 shows that errors in the model can strongly affect the ability to match the target velocities. The residuals are high and widespread and the patterns in experiment 7 resemble the residuals in real-data inversions. Despite the large deviations of basal yield stress from the target values, the target velocities cannot be matched well. Experiment 8 displays the typical wave-like patterns that arise from the $\mathbf{u}^{\text{SIA}}$ calculation. This pattern is visible in the residual as well as in the difference $\mathbf{u}^{\text{ref}} - \mathbf{u}^{\text{target}}$ and will be discussed in the next section. Note that the wave-like pattern in residual in Experiment 8 is not visible in the real-data inversion.

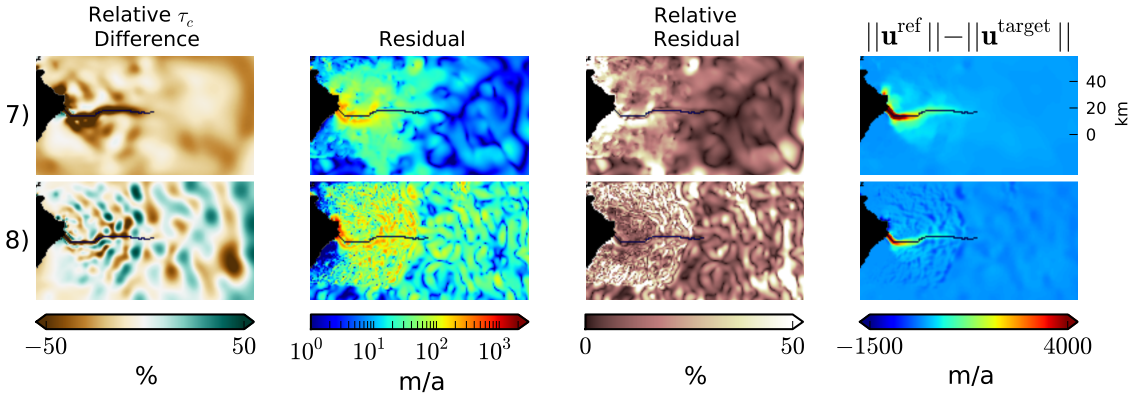

Figure 4.4. Synthetic inversions with errors in ice flow model. The columns show the relative τ_c difference ($||\tau_c^{\text{synth}} - \tau_c^{\text{mod}}||/||\tau_c^{\text{synth}}||$), the residual ($||\mathbf{u}^{\text{target}} - \mathbf{u}^{\text{mod}}||$), the relative residual ($||\mathbf{u}^{\text{target}} - \mathbf{u}^{\text{mod}}||/||\mathbf{u}^{\text{target}}||$), and the difference between $||\mathbf{u}^{\text{target}}||$ used in the inversion and $||\mathbf{u}^{\text{ref}}||$ which is the velocity resulting from the reference forward model. The rows show results for experiments 7): the $\mathbf{u}^{\text{target}}$ are produced with a Glen's flow law constant set to $n = 2.5$ and the ice softness set accordingly to $A = 1 \times 10^{-21}$ $\text{Pa}^{-3}\text{s}^{-1}$, 8): the $\mathbf{u}^{\text{target}}$ are produced by adding SIA velocities to $\mathbf{u}^{\text{synth}}$

Discussion of residual pattern experiments

Experiment 8 displays a distinct wave-like pattern in residuals. This wave-like pattern is a result of wave-like SIA velocity fields that cannot be achieved with the SSA-only inversion. The wave-like features most likely represent the mismatch between bed topography and surface elevations. If both of these fields would be perfect, the SIA would produce a wrong surface velocity field (because the SIA is not necessarily a good model simplification), but this velocity field would not display such a distinct wave-like pattern. When running the hybrid model forward in time and allowing the surface to evolve, these wave-like patterns in SIA velocities smooth out. This in turn, reduces the wave-like patterns in the residual fields when using the evolved surface instead of the measured surface elevations in the inversion (see Section 4.4.2).

Investigating the residual patterns, we see that the residual pattern of the bed topography experiment (Exp. 6) has high values in the fast-flowing terminus region, but the widespread $50 - 100\,\text{m}\,\text{a}^{-1}$ residuals seen in the real-data inversion are not present. The difference between the two bed topography fields is largest in the deep trough, which is the area where actual uncertainties in bed topography are expected to be large because of the difficult bed return recovery. In this sense, our experiment represents a realistic as-

sumption about bed topography uncertainties and we expect similar residual patterns for actual uncertainties in bed topography. The model error experiment (Exp. 7) is the only one with the characteristic widespread pattern of $50 - 100\,\mathrm{m\,a^{-1}}$ residuals, but the residuals in the deep trough are not as high as in the real-data inversion.

Figure 4.5 shows that only with the hybrid model experiment are we able to reach the high data-model misfit values displayed in the real-data inversions. The residual patterns on the other hand, show that the high residuals in the hybrid model experiment are due to the addition of unrealistic SIA velocities. The wide-spread high residual pattern of experiment 7 is very similar to the real-data inversion, but the L-curve shows that the data-model misfit over the entire misfit area is still too low. Adding the residuals from the bed topography experiment (Exp. 6) would lead to a data-model misfit value that is closer to the real-data inversion. The flat shape of the L-curve occurs for both model error experiments. This makes it difficult to find a clear corner, which introduces additional uncertainties into the inversion results. But this is also the case for real-data inversions, so we are able to reproduce the residual patterns and the shape of the L-curve of the real-data inversion.

The synthetic experiments might suggest that the real-data inversions could be improved by using the newer CReSIS bed topography, or a model that uses a Glen's flow law parameter of $n = 2.5$ with an adjusted ice softness, which has been suggested to be a better choice for the Jakobshavn Isbræ [*Funk et al.*, 1994]. Inspection of the L-curves for these inversions shows that the CReSIS topography actually increases the data-model misfit and that the improvement when using $n = 2.5$ is negligible (Fig. 4.6). The residual patterns for these inversions (not shown) are almost indistinguishable from the pattern in Figure 4.1. The hybrid model applied to the real-data inversion leads to higher data-model misfit values than the reference inversion. We conclude that even with the newest bed topography and an adjusted Glen's flow law parameter, the residual patterns are not significantly improved. Therefore, we conclude that even further improvements in bed topography data and/or more complex models are necessary for an improved data-model misfit in the terminus region.

4.4 Weighted misfit function

In the experiments discussed above, all points within the misfit area have been equally weighted, regardless of the magnitude of velocity or the expected error at that point. It has been suggested by *Morlighem et al.* [2010] that such unweighted cost functions work

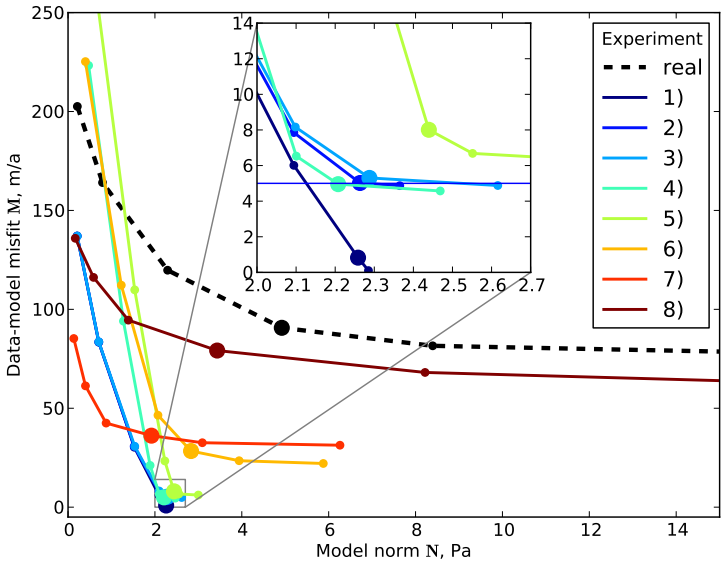

Figure 4.5. L-curves for all velocity residual pattern experiments. The bold dots mark the inversions that are shown in the map-view figures above for each experiment. The blue line in the inset shows the calculated data-model misfit for experiment 2.

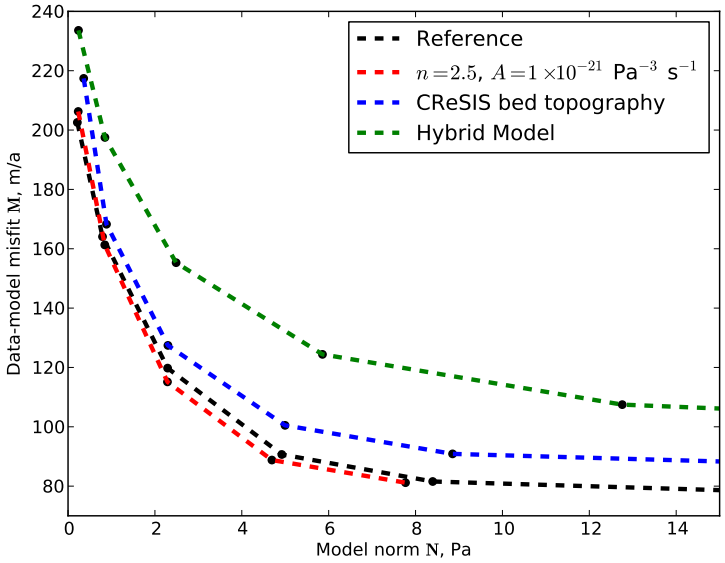

Figure 4.6. L-curves for real-data inversions with different model and ice geometry

Table 4.1. Summary of synthetic residual pattern experiments. 'Ref.' refers to the reference inversion: geometry given by bed topography from *Plummer et al.* [2008] and the 2006 surface DEM described in *Habermann et al.* [2013]. The Glen's flow law parameter is set to $n = 3$, the ice softness is set to $A = 2.5 \times 10^{-24}$ $\mathrm{Pa}^{-3}\mathrm{s}^{-1}$ and the SSA as a forward model.

	Bed Elevation	Surface Elevation	Model	Velocity Noise	$\mathbf{u}^{\mathrm{target}}$
1)	Ref.	Ref.	Ref.	None	$\mathbf{u}^{\mathrm{synth}}$
2)	Ref.	Ref.	Ref.	Gaussian	$\mathbf{u}^{\mathrm{synth}} + \mathbf{u}^{\mathrm{noise}}$
3)	Ref.	Ref.	Ref.	Rel. Noise	$\mathbf{u}^{\mathrm{synth}} + \mathbf{u}^{\mathrm{noise}}$
4)	Ref.	Ref.	Ref.	Obs. Noise	$\mathbf{u}^{\mathrm{synth}} + \mathbf{u}^{\mathrm{noise}}$
5)	Ref.	Gaussian	Ref.	None	$\mathbf{u}^{\mathrm{synt}}_{\mathrm{surf}}$
6)	CReSIS	Ref.	Ref.	None	$\mathbf{u}^{\mathrm{synt}}_{\mathrm{bed}}$
7)	Ref.	Ref.	$n = 2.5$, $A = 1.7 \times 10^{-21}\,\mathrm{Pa}^{-3}\mathrm{s}^{-1}$	None	$\mathbf{u}^{\mathrm{synt}}_{\mathrm{n=2.5}}$
8)	Ref.	Ref.	Hybrid Model	None	$\mathbf{u}^{\mathrm{synth}} + \mathbf{u}^{\mathrm{SIA}}$

better in fast-flow areas because the gradients of the misfit functional are larger where $||\mathbf{u}^{\mathrm{target}} - \mathbf{u}^{\mathrm{mod}}||$ is high, which occurs in regions of fast flow. According to this, a misfit functional that weights the slow flow areas stronger would lead to improved resolution of basal yield stress there. Here, we test the resolution strength of weighted and unweighted misfit functionals.

Checkerboard pattern experiments were performed on the limited domain close to the terminus. The first inversion is performed with a constant weighting in the misfit functional. The second one excludes all points with speeds above $600\,\mathrm{m\,a}^{-1}$ from the misfit area (giving them zero weight). Figure 4.7 shows that this reduced weight of the misfit function only affects the fast-flow areas. The slow-flow areas on the other hand do not improve their resolution of the checkerboard pattern despite the increase in relative weight. There are no visible differences in the velocity fields of the slow-flow areas generated with or without the checkerboard pattern in basal yield stress. The ice flow in these areas is too slow to be affected by the changes in basal yield stress [*Gudmundsson*, 2003], therefore the inversion is not able to resolve the basal yield stress here.

We conclude that the limited transfer of changes in basal conditions to the surface is

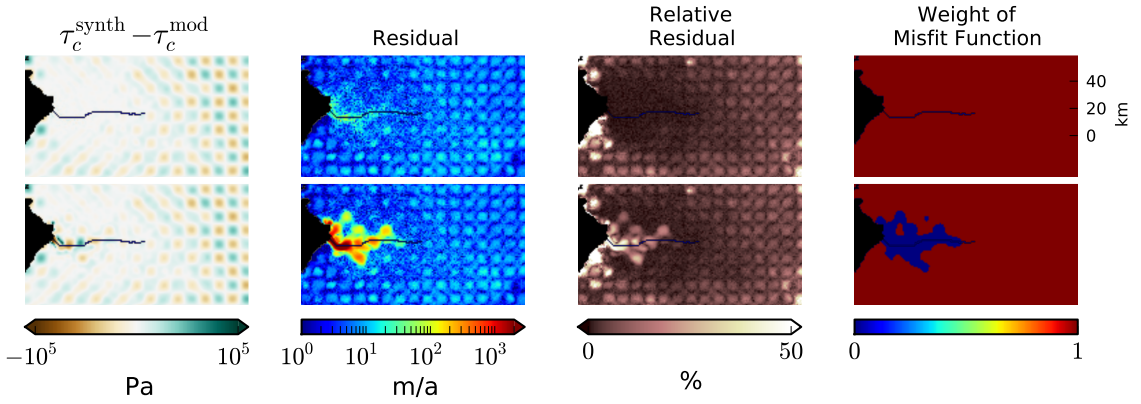

Figure 4.7. Influence of a simple weighted misfit functional on the resolution strength of a synthetic checkerboard pattern of basal yield stress. The columns show the difference between the true basal yield stress and the recovered basal yield stress (white areas indicate perfect recovery), velocity residuals ($||\mathbf{u}^{\text{target}} - \mathbf{u}^{\text{mod}}||$), the relative residual ($||\mathbf{u}^{\text{target}} - \mathbf{u}^{\text{mod}}||/||\mathbf{u}^{\text{target}}||$), and the weighting of the misfit function. For the top row the entire misfit area is weighted equally, for the bottom row the areas where ice flow is above $600\,\text{m}\,\text{a}^{-1}$ is given zero weight. Checkerboard amplitude is 5×10^4 Pa and the wavelength is 20 km.

the main reason for the lack of resolution in slow-flow areas. Even a more sophisticated logarithmic misfit functional as used in [*Morlighem et al.*, 2010] would not improve the inversion results for the case of Jakobshavn Isbræ. Therefore, in this study we weight all points within the misfit area equally.

4.4.1 Resolution of basal yield stress in entire drainage basin

Useful estimates of basal yield stress for prognostic ice-sheet or drainage basin wide models need to cover the entire area that is modeled. The Shallow Shelf Approximation is applicable to fast flowing ice streams but not for the slower flowing areas in the interior of the ice sheet. Here we investigate the resolution strength of SSA inversions for the entire drainage basin of Jakobshavn Isbræ.

Figure 4.9 shows that the larger the amplitude of the variation the higher upstream it will be resolved. Amplitudes in the order of 1×10^3 Pa (not shown) cannot be resolved with a 5 m/a Gaussian noise.

We performed several synthetic tests on the entire domain. A checkerboard pattern of basal yield stress is produced by taking τ_c^{mod} from Figure 4.1 and overlaying it with lateral and longitudinal variations of basal yield stress with a certain amplitude and wavelength.

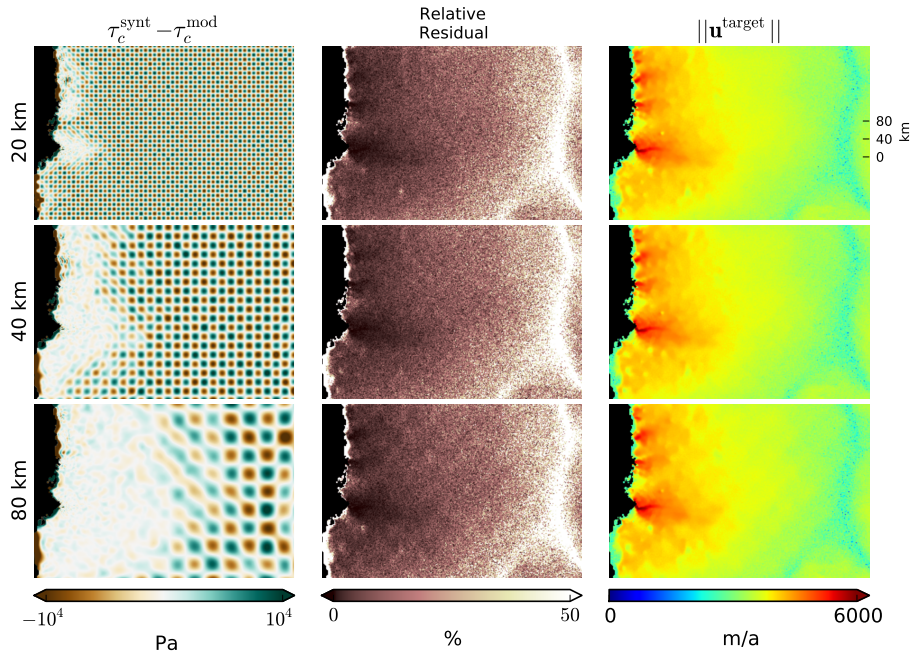

Figure 4.8. Resolution of checkerboard patterns of different wavelengths. The amplitude of the basal yield stress checkerboard pattern is 1×10^4 Pa for all rows. White areas in the first column signify a good resolution of the checkerboard pattern.

In cases where the amplitude of the checkerboard pattern would cause negative values of basal yield stress, τ_c is set to zero. This checkerboard pattern is used in a SSA forward model to get $\mathbf{u}^{\text{synth}}$, a small amount of uncorrelated Gaussian noise (standard deviation of 5 m/a) is added and the resulting $\mathbf{u}^{\text{target}}$ is used in the inversion. Checkerboard patterns of different wavelengths and amplitudes for τ_c are produced. The prior estimate of basal yield stress was set to $\tau_c^{\text{prior}} = 1 \times 10^5$ Pa for all inversions in this section. Figure 4.8 shows that even variations of 60 km wavelength ($\sim$ 60 times the ice thickness in the channel) can only be resolved in the downstream half of the domain.

The improved resolution strength for faster flowing ice is in agreement with *Gudmundsson* [2003], who found that the transfer of basal topography and basal yield stress to the surface is highly dependent on the amount of motion at the base. Figures 4.8 and 4.9 show that the checkerboard pattern is transferred to the surface (visible in $\mathbf{u}^{\text{target}}$) mainly for the fast-flow areas. An expression of the checkerboard pattern in $\mathbf{u}^{\text{target}}$ is only visible for the large amplitudes and wavelengths. And even in these extreme cases, the checkerboard pattern is not entirely recovered in τ_c^{mod}. The experiments performed in this section are

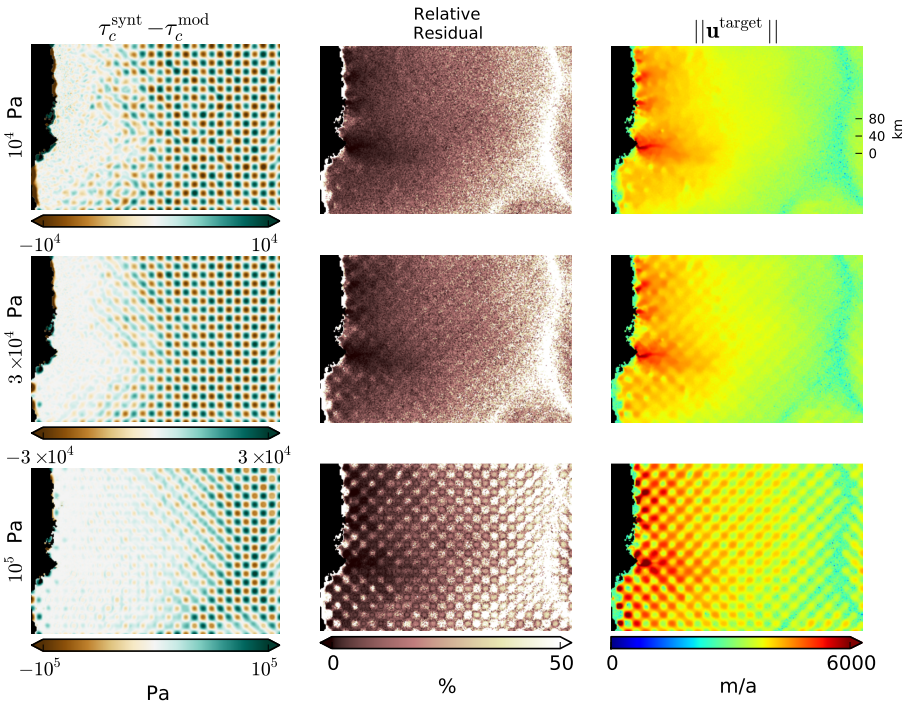

Figure 4.9. Resolution of checkerboard patterns of different amplitudes. The wavelength of the basal yield stress checkerboard pattern is 40 km for all rows. White areas in the first column signify a good resolution of the checkerboard pattern.

a best case scenario, where the only source of uncertainty is introduced as noise in the surface velocity and the SSA is assumed to be valid for the entire drainage basin. Additional sources of error such as model or input parameter will most likely decrease the resolution strength further.

4.4.2 Initial conditions for Jakobshavn Isbræ

The limitations in resolution strength outlined in the last section exacerbate the problem that different solutions for the basal yield stress of the entire drainage basin are possible. The influences of prior estimate, ice softness, hybrid model, ice geometry and gaps in data coverage are investigated with the experiments listed in Table 4.2 and results are shown in Figure 4.10. For all inversions the H^1 model norm is used in the regularization term and the regularization parameter is found with the L-curve method. The goal is to show sensitivities of the basal yield stress solutions and to suggest a basal yield stress field that should be used for prognostic model runs with the hybrid model of PISM. Therefore, most

inversions in this section are performed with the hybrid model.

Inversions 1 and 2 illustrate a high and low prior estimate, respectively. The low-resolution, slow-flow area is most affected; for the high prior estimate the basal shear stress is already strong enough to lead to ice velocities that are in good agreement with the observations. The low prior estimate, on the other hand, causes higher ice velocities than observed and therefore, the basal shear stress is corrected upwards until a satisfactory match with observations is achieved. In this manner, choosing a low prior estimate will give a lower limit on the necessary basal shear stress to reproduce observed surface velocities.

Inversion 3 was performed with a spatially-varying ice temperature field from a constant-climate spin-up performed with PISM as outlined in *Aschwanden et al.* [2013]. The general pattern of basal yield stress is similar to the constant ice softness experiment (Inversion 2), but the slow-flow area shows lower residuals compared to inversion 2. The constant ice softness used in inversion 2 was chosen to achieve an optimal fit in the terminus region, resulting in relatively soft ice. The ice softness from the spin-up on the other hand indicates harder ice in the slow-flow areas. Therefore the ice velocities match the observations better even without introducing a stiff bed. In the fast-flow area the basal yield stress patterns are very similar and differences are only visible north of Jakobshavn Isbræ. This justifies the choice of a constant ice softness for the area close to the terminus. However, for drainage-basin-wide inversions the changes in ice softness further upstream become important and improve the residuals greatly.

Inversion 4 matches observed surface velocities with velocities derived by the SSA only. The largest differences in modeled basal yield stress compared to the previous inversions occur in areas of slow-flow (low-resolution) and north of Jakobshavn Isbræ. The velocity residuals are lower than for the hybrid case and the residual patterns lack the wave-like features of the hybrid inversion.

Prognostic model runs need initial and boundary conditions for the entire model domain and spin-ups are used to produce a realistic and consistent temperature field within the ice. In the spin-up, the surface elevation of the ice is allowed to evolve and the surface at the end of the spin-up is also used as the initial state for prognostic runs. This surface elevation with the accompanying temperature field is used for Inversion 5. Despite the use of the hybrid model in the inversion, the residuals do not display the wave-like features as seen in Inversions 1, 2 and 3. Using the hybrid model in the spin-up causes the surface

to smooth out and the high driving stresses caused by the mismatch between surface elevation and bed topography are not present anymore. The hybrid inversion reduces the velocity residual when used with the ice geometry and temperature from a spin-up: only the fast flow areas close to the termini still show large residuals. Note that the smaller outlet glaciers north of Jakobshavn Isbræ show the largest improvement in residual and a more realistic basal yield stress field compared to inversions with the observed ice surface elevation. In these outlet glaciers the bed topography data is not as detailed as in Jakobshavn Isbræ and an evolved ice surface can compensate for these errors.

Inversion 6 uses the same ice geometry as Inversion 5. Additionally, τ_c^{prior} is set to the basal yield stress from the spin-up. In PISM, the basal yield stress is defined as the product between the tangent of a till friction angle and the effective pressure. The latter is calculated while the till friction angle has to be set heuristically. Here we follow the current implementation in PISM and define a linear relationship between the till friction angle and the bed elevation, assuming that lower till will be weak due to the existence of marine sediments. This definition results in a spatially varying τ_c that mirrors much of the small-scale structure found in the bed topography data, especially close to the terminus where radar efforts have led to a relatively detailed bed topography. The inferred τ_c^{mod} shown in Figure 4.10 contains these small scale structures because they do not affect the modeled velocities enough to be corrected. The difference between modeled and prior τ_c shows that a lowering of the basal yield stress is introduced in order to match the observed velocities. The residual field shows that a good match to observed velocities is easier when using a spatially constant value for τ_c^{prior} as done in Inversion 5.

Data gaps

The influence of data gaps is investigated by excluding an area with missing data points from the misfit area. The misfit functional does not take into account grid points where data is missing, but the basal yield stress can still be corrected in these areas. Inversion 7 in Figure 4.11 shows that large data gaps greatly influence the inferred basal yield stress and the data-model misfit is large. Smaller data gaps and those trending across the flow direction do not influence the inferred basal yield stress as strongly. Data gaps do not constrain the inverse method used here, but the basal yield stress solution for large areas with missing data will be strongly dependent on the prior estimate of basal yield stress.

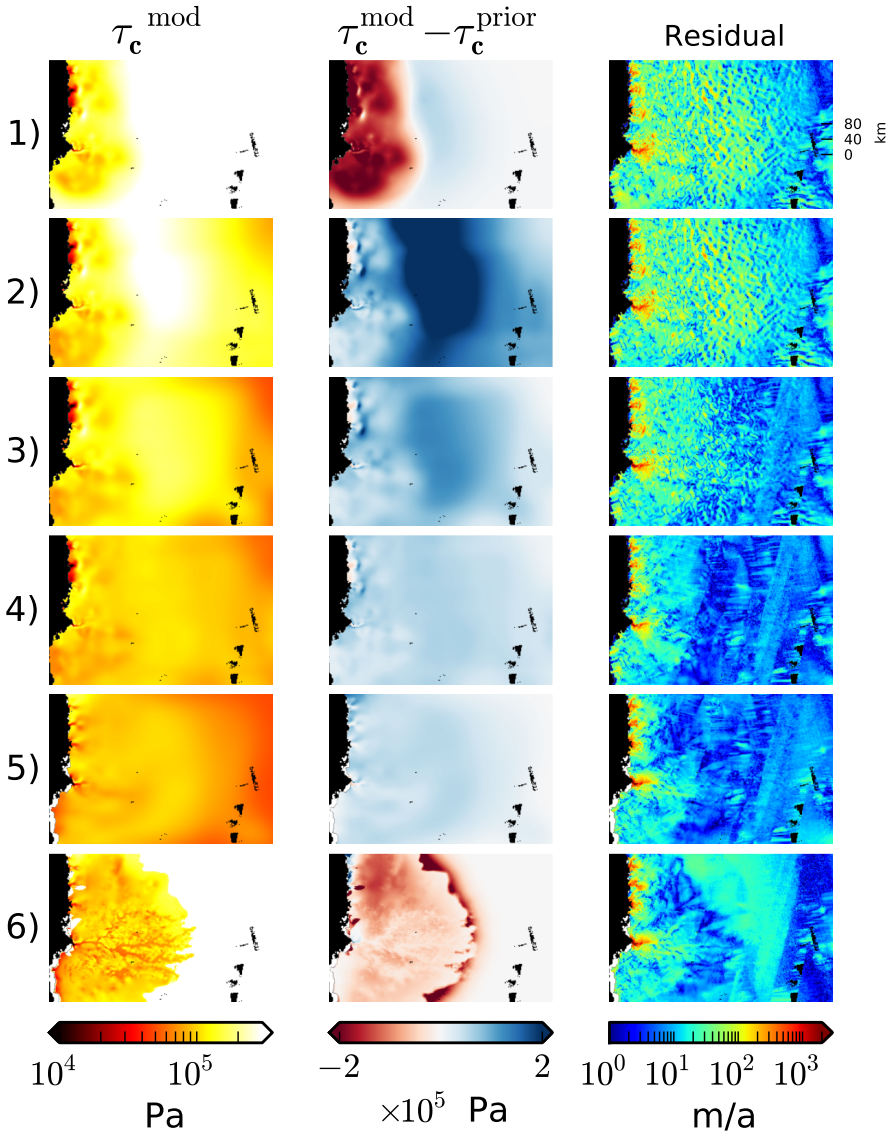

Figure 4.10. Sensitivity of real-data τ_c inversion to various choices. Real-data, drainage-basin wide τ_c inversions for 1) high τ_c^{prior}, 2) low τ_c^{prior}, 3) temperature field from spin-up, 4) SSA only forward model, 5) temperature field and ice geometry from spin-up, 6) τ_c^{prior} is set to the τ_c of the spin-up. The inversions are summarized in Table 4.2.

Table 4.2. Sensitivity of real-data τ_c inversion to various choices. Summary of real-data, drainage-basin wide τ_c inversions shown in Figure 4.10. For all inversions the averaged velocity described in Sec. 4.2.1, the H^1 model norm, and a regularization parameter found with the L-curve method is used. 'Ref.' refers to the reference inversion described in Section 4.2.

	Model	Ice Geometry	Ice Softness A $\times 10^{-24}$ $\mathrm{Pa}^{-3}\mathrm{s}^{-1}$	τ_c^{prior} $\times 10^5\,\mathrm{Pa}$	Comment
1)	Hybrid	Ref.	2.5	3	No adjustment of τ_c upstream
2)	Hybrid	Ref.	2.5	0.5	Better adjustment of τ_c upstream, but still high residuals upstream
3)	Hybrid	Ref.	Spun-up	0.5	Improved residual upstream, but wave-like features remain
4)	SSA	Ref.	2.5	0.5	Wave-like residual structure disappears, but SSA not realistic upstream
5)	Hybrid	Spun-up	Spun-up	0.5	Wave-like residual structure disappears
6)	Hybrid	Spun-up	Spun-up	τ_c used in spin-up	Small-scale structure is not corrected

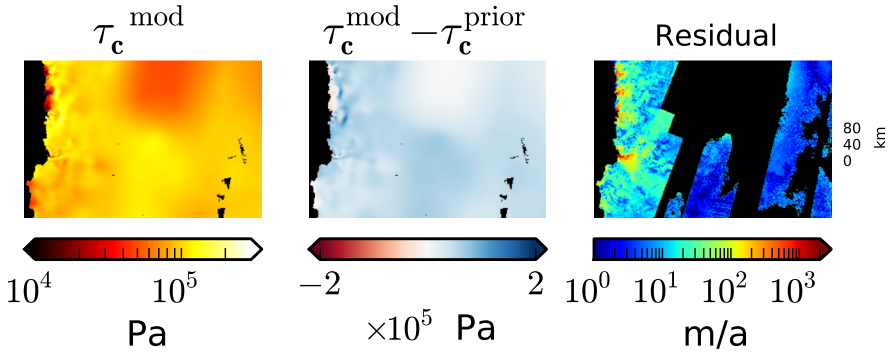

Figure 4.11. Real-data, drainage-basin wide τ_c inversions with data gaps (blacked out areas shown in right column) from the 2006 data set. Forward model, including ice geometry same as in experiment 4 (see Tab. 4.2)

4.5 Discussion and Conclusions

Synthetic experiments suggest that errors in surface velocity observations are not sufficient to explain the high residuals close to the terminus in real data inversions. Errors in ice geometry lead to residual patterns that match the real data inversion better, but only errors in the model are able to reproduce high residuals with similar patterns. This could indicate the need for higher order models in areas close to the terminus of Jakobshavn Isbræ. On the other hand, our residuals and relative residuals are comparable to the ones obtained by a full Greenland inversion with a Stokes model performed by *Gillet-Chaulet et al.* [2012]. In their study the regularization parameter was chosen for the entire ice-sheet, not just for the drainage basin of Jakobshavn Isbræ as done in our study. Only a direct comparison of residuals from identical inversions could show how important the model simplifications are compared to the uncertainties in ice geometry.

Checkerboard tests over the entire drainage basin show that for smaller amplitude and wavelength of perturbations the area where basal yield stress can be resolved is constrained to the fast flow areas close to the termini. This effect is also apparent in the real data inversions for the entire drainage area: the basal yield stress solution is highly dependent on the prior estimate in areas of low resolution strength. Where the ice is frozen to the bed or basal motion is negligible, the observed surface velocities only contain information about the ice deformation and not the basal motion. Only when ice flow in these areas increases such that there is basal motion would we be able to make inferences about the properties at the base. These limitations in resolution lead to a high sensitivity of the

inversion results to the initial estimate of basal yield stress. A low constant value for τ_c^{prior} is suggested because this will at least resolve a lower bound in areas where the ice is frozen to the bed. A high τ_c^{prior} on the other hand, will not be adjusted to give an upper bound in these areas because any high value of τ_c will already produce non-sliding conditions at the base.

The real-data inversions with the hybrid model display a small-scale wavy structure, especially visible in inversions 1 and 2. The higher residual points are caused by steep surface slopes which lead to higher driving stresses for the calculation of the SIA component of the velocity. In many places the calculated SIA velocities are indeed larger than the observed velocities leading to $\mathbf{u}^{\text{target}}$ velocities that point in the opposite direction of the observed velocities. Therefore, the inversion algorithm is trying to match unrealistic velocity fields and is unable to achieve this, as seen in the large residuals. When using inversions to improve the initial boundary conditions at the base of the ice it is reasonable to perform the inversion with an ice geometry and temperature field from a spin-up; in this way a self-consistent model setup is achieved. It is also possible to use the basal yield stress at the end of the spin-up as the initial estimate in the inversion (Inv 6); so that only areas where the velocity fields require a correction in τ_c will be adjusted. In this way inconsistencies with the temperature field can be minimized, on the other hand, a lot of small scale features are introduced with this type of initial estimate. As shown in *Habermann et al.* [2013] such small scale features in the prior estimate of basal yield stress will be preserved, especially when using a H^1 model norm.

When using inversion algorithms it is important to define the questions and goals clearly. For realistic prognostic models of surface velocities the main goal might be to achieve a setup that is self-consistent while matching observations as closely as possible. For other studies it might be more important to model the actual *in situ* basal yield stress as closely as possible. Different situations will make different modeling choices necessary. In all cases it is important to remember the limitations of inverse results and that the resulting basal yield stress will incorporate other model errors, such as an incorrect temperature field.

4.6 Acknowledgements

This work was supported by NASA NNX09AJ38G, NSF CMG 0732602, NSF CMG 0724860 and in part by the College of Natural Science and Mathematics at the University of Alaska,

Fairbanks. We acknowledge the use of data and data products from CReSIS generated with support from NSF grant ANT-0424589 and NASA grant NNX10AT68G, as well as Joughin, I., B. Smith, I. Howat, and T. Scambos. 2010. MEaSUREs Greenland Ice Velocity Map from InSAR Data. Boulder, Colorado, USA: National Snow and Ice Data Center. Digital media. Ed Bueler, Constantine Khroulev, and Andy Aschwanden have supported the modeling efforts and provided feedback.

References

Alley, R. B., and I. Joughin (2012), Modeling Ice-Sheet Flow, *Science*, pp. 551–552.

Amundson, J. M., M. Truffer, M. P. Lüthi, M. A. Fahnestock, M. West, and R. J. Motyka (2008), Glacier, fjord, and seismic response to recent large calving events, Jakobshavn Isbræ, Greenland, *Geophysical Research Letters*, *35*(22), L22,501, doi: 10.1029/2008GL035281.

Aschwanden, A., G. Adalgeirsd o ttir, and C. Khroulev (2013), Hindcasting to measure ice sheet model sensitivity to initial states, *The Cryopshere*, *in press*.

Aster, R. C., B. Borchers, and C. H. Thurber (2005), *Parameter Estimation and Inverse Problems*, Elsevier Academic Press, New York.

Bamber, J. L., R. Layberry, and S. P. Gogineni (2001), A new ice thickness and bed data set for the Greenland ice sheet. 1. Measurement, data reduction, and errors, *Journal of Geophysical Research*, *106*(D24), 33,773–33,780.

Bamber, J. L., et al. (2013), A new bed elevation dataset for Greenland, *The Cryosphere*, *7*(2), 499–510.

Bueler, E., and J. Brown (2009), Shallow shelf approximation as a "sliding law" in a thermomechanically coupled ice sheet model, *Journal of Geophysical Research*, *114*(03), F03,008, doi: 10.1029/2008JF001179.

Funk, M., K. A. Echelmeyer, and A. Iken (1994), Mechanisms of fast flow in Jakobshavns Isbræ, Greenland: Part II. Modeling of englacial temperatures, *Journal of Glaciology*, *40*(136), 569–585.

Gillet-Chaulet, F., O. Gagliardini, H. Seddik, M. Nodet, G. Durand, C. Ritz, T. Zwinger, R. Greve, and D. G. Vaughan (2012), Greenland ice sheet contribution to sea-level rise from a new-generation ice-sheet model, *The Cryosphere*, *6*(6), 1561–1576.

Gudmundsson, G. H. (2003), Transmission of basal variability to a glacier surface, *Journal of Geophysical Research*, *108*(B5), doi: 10.1029/2002JB002107.

Habermann, M., M. Truffer, and D. Maxwell (2013), Changing basal conditions during the speed-up of Jakobshavn Isbræ, Greenland, *The Cryosphere Discuss.*, *7*(3), 2153–2190.

Holland, D. M., R. H. Thomas, B. De Young, M. H. Ribergaard, and B. Lyberth (2008), Acceleration of Jakobshavn Isbræ triggered by warm subsurface ocean waters, *Nature Geoscience*, *1*, 659–664.

Joughin, I., W. Abdalati, and M. A. Fahnestock (2004), Large fluctuations in speed on Greenland's Jakobshavn Isbrae glacier, *Nature*, *432*(7017), 608–610.

Joughin, I., I. M. Howat, M. A. Fahnestock, B. E. Smith, W. B. Krabill, R. B. Alley, H. Stern, and M. Truffer (2008), Continued evolution of Jakobshavn Isbrae following its rapid speedup, *Journal of Geophysical Research*, *113*(04), F04,006, doi: 10.1029/2008JF001023.

Joughin, I., B. E. Smith, I. M. Howat, T. Scambos, and T. Moon (2010), Greenland flow variability from ice-sheet-wide velocity mapping, *Journal of Glaciology*, *56*(197), 415–430.

Joughin, I., B. E. Smith, I. M. Howat, D. Floricioiu, R. B. Alley, M. Truffer, and M. A. Fahnestock (2012), Seasonal to decadal scale variations in the surface velocity of Jakobshavn Isbrae, Greenland: Observation and model-based analysis, *Journal of Geophysical Research*, *117*, F02,030, doi: 10.1029/2011JF002110.

Morlighem, M., E. Rignot, H. Seroussi, E. Larour, H. B. Dhia, and D. Aubry (2010), Spatial patterns of basal drag inferred using control methods from a full Stokes and simpler models for Pine Island Glacier, West Antarctica, *Geophysical Research Letters*, *37*, L14,502, doi: 10.1029/2010GL043853.

Motyka, R. J., M. A. Fahnestock, and M. Truffer (2010), Volume change of Jakobshavn Isbrae, West Greenland: 1985-1997-2007, *Journal of Glaciology*, *56*(198), 635–646.

Plummer, J., S. P. Gogineni, C. J. van der Veen, C. Leuschen, and J. Li (2008), Ice thickness and bed map for Jakobshavn Isbræ, *Tech. Rep. 1*.

Podlech, S., and A. Weidick (2004), A catastrophic break-up of the front of Jakobshavn Isbrae, West Greenland, 2002/03, *Journal of Glaciology*, *50*(168), 153–154.

Schoof, C. G., and R. C. A. Hindmarsh (2010), Thin-film flows with wall slip: an asymptotic analysis of higher order glacier flow models, *The Quarterly Journal of Mechanics and Applied Mathematics*, *63*(1), 73–114.

Thomas, R. H., W. Abdalati, E. Frederick, W. B. Krabill, S. Manizade, and K. Steffen (2003), Investigation of surface melting and dynamic thinning on Jakobshavn Isbrae, Greenland, *Journal of Glaciology*, *49*(165), 231–239.

Chapter 5
Conclusions

Geophysical inverse methods are used to infer physical parameters from direct observations. It is crucial to avoid using these methods as a 'black box' with one 'correct answer'. The regularization of the problem and the inherent uncertainties are important for a proper interpretation of the solution. We show that iterative inverse methods can be used successfully if an appropriate stopping criterion is used as a means of regularization. We illustrate the effect of observation errors on the solution and emphasize the danger of overfitting. We also introduce a new rapidly converging iterative inverse method called the Incomplete Gauss Newton method, which is intrinsically tied to an appropriate stopping criterion. We show that the commonly used steepest descent method has a slow convergence rate, which fortuitously prevents overfitting. On the other hand it also inhibits us from reaching full resolution in the basal yield stress, and increases the dependence on initial estimates.

A careful application of inverse methods to the rapid changes of the terminus region of Jakobshavn Isbræ reveals a decrease in basal yield stress as the glacier increased its surface speed by a factor of two or more. This decreased basal yield stress in the deep trough close to the terminus is a robust signal even when taking into account the uncertainties in the inversion. The observed changes are in agreement with a Mohr-Coulomb parameterization of basal yield stress, where the change in effective pressure is the main driver for the changes in basal yield stress. This result supports previous findings of an ocean and terminus driven system. Additionally, this practical application of inverse methods shows that conclusions can be drawn from inversion results despite the large uncertainties associated with the method.

It also becomes apparent that model surface velocities cannot be fit to surface velocity observations within the error of observations. This indicates that other errors play a critical role. We find that, in the case of Jakobshavn Isbræ, the errors in observed and interpolated ice geometry and model simplifications influence the ability to reproduce observed velocity fields more than the error in observed velocity does. This indicates that further progress must come from model improvements and improved capabilities to measure bedrock geometry, or to include bedrock geometry refinement in the inverse method.

This research shows that, when applied properly, inverse methods are very powerful and can deliver information about difficult-to-measure parameters as well as the physical model used to describe the system. With today's wealth of large-scale satellite data we

can take full advantage of these methods. Data-assimilation methods, where the newest observations are used in inversions to constantly improve the initial and boundary conditions, are increasingly important when predicting future changes in ice-sheets. Hazard mitigation and policy making are depending on accurate predictions of the near future ($\sim$50 years), and inverse methods can supply the necessary initial and boundary conditions to make such short-term forecasts possible. Ideally, all available measurements (e.g. ice velocity, ice temperature from boreholes, ice surface elevation) would be included in an inverse problem where all unknown parameters are solved for simultaneously. This research also shows that, inverse methods can show where the largest uncertainties in the current understanding lie and can guide data collection and direct model development.